INTERFACIAL PROPERTIES OF EPITAXIAL GOLD NANOCRYSTALS SUPPORTED ON RUTILE TITANIUM DIOXIDE

BY

SHANKAR SIVARAMAKRISHNAN

DISSERTATION

Submitted in partial fulfillment of the requirements
for the degree of Doctor of Philosophy in Materials Science and Engineering
in the Graduate College of the
University of Illinois at Urbana-Champaign, 2010

Urbana, Illinois

Doctoral Committee:

Associate Professor Jian-Min Zuo, Chair
Professor Ivan Petrov
Assistant Professor Dallas Trinkle
Professor John Weaver

ABSTRACT

Interfacial science is a fascinating field in materials science. From grain boundaries in bulk materials to interfaces in thin films, the properties of interfaces can lead to novel functionality in materials. The effect of interfaces on a material's properties becomes amplified as the proportion of interfaces increases in relation to the volume of the material, for example in supported nanocrystals (NCs). While interfaces in bulk materials and thin films have been well characterized, atomic level characterization of NC interfaces is limited. The aim of this thesis is to develop a general set of methods to comprehensively study NC interfaces including interfacial atomic structure, interfacial energy and interfacial line tension. We have selected Au-TiO_2 interface that has significant attention for its role in the remarkably low temperature catalytic oxidation of carbon monoxide to carbon dioxide.

One of the best methods to study interfaces in bulk materials and thin films is cross sectional Transmission Electron Microscopy (TEM). Particularly with the advent of aberration corrected electron microscopy the experimental power to probe interfaces has increased manifold. However it is difficult to prepare NCs in the cross sectional viewing geometry for TEM without damaging the NCs using conventional specimen preparation methods. To enable this work, firstly a specimen preparation method was developed to support epitaxial Au NCs in the cross sectional geometry for TEM investigations without damaging the NCs.

The interfacial atomic structure was investigated using aberration corrected Scanning Transmission Electron Microscopy (STEM) with a spatial resolution of ~1Å. Interfacial energy of the NCs has been measured from cross sectional STEM images of NCs. It is found that Au NCs with the epitaxial relationship $Au(111)_{[-110]} \parallel TiO_2\ (110)_{[001]}$ have the largest adhesion to

TiO_2 (110) with an interfacial energy of 0.61±0.05 J/m^2 (assuming $\gamma_{TiO2(110)}$ = 0.33 J/m^2 and $\gamma_{Au(111)}$ = 1.283 J/m^2). The stability of this epitaxy is attributed to the nucleation of Au atoms in the missing titanium row of a (1x2) TiO_2 (110) reconstruction – resulting in an interfacial reconstruction of Au, Ti and O atoms which lowers the interfacial energy and enhances the adhesion of Au NCs to TiO_2 (110).

It has been found that smaller Au NCs dewet more than bigger Au NCs on TiO_2 (110). The dewetting is attributed to the effect of interfacial line tension. In order to measure interfacial line tension, the Wulff-Kaishew was modified to incorporate the effect of interfacial line tension on NC shapes. The lower limit of interfacial line tension was measured to be 0.85±0.24 eV/Å (1.36±0.38 x 10^{-9} N) (assuming $\gamma_{TiO2(110)}$ = 0.33 J/m^2 and $\gamma_{Au(111)}$ = 1.283 J/m^2) for NCs with the epitaxial relationship of $Au(111)_{[-110]}$ || TiO_2 $(110)_{[001]}$.

Since TEM/STEM studies are limited to individual NCs, the formation of epitaxial Au NCs was also probed using Reflection High Energy Electron Diffraction (RHEED) of Au NCs on flat TiO_2 (110) supports in order to obtain structural information averaged from a larger number of NCs. The RHEED study confirms the epitaxial relationship of Au NCs as $Au(111)_{[-110]}$ || TiO_2 $(110)_{[001]}$, irrespective of the details of the starting TiO_2 (110) surface structure and the annealing atmosphere. On reconstructed (1x2) TiO_2 (110) surfaces, the onset and completion of epitaxy formation occurred at much lower temperatures than unreconstructed TiO_2 (110) surfaces. This shows that Au prefers to nucleate and grow as epitaxial NCs over (1x2) reconstructed TiO_2 (110) in agreement with TEM/STEM images of NCs.

To the people I owe most,

My Parents

Teachers at Sri Sankara Senior Secondary School

Prof. P. Sankaran

Swami Mitrananda

ACKNOWLEDGEMENTS

I owe my first thanks to my advisor Prof. Jim Zuo for his guidance and technical inputs. Jim maintains a healthy balance between development of characterization techniques and fundamental studies of structure-property relationship in materials. This balance has immensely helped me develop a better appreciation of many fields of materials science. I am grateful to Jim for fostering a culture of diverse research in the group.

I have had many co-workers in the Zuo research group who have contributed to this thesis, directly and indirectly. I wish to thank Fakhruddin Bohra, Dr. Weijie Huang, Dr. Kazuhisa Sato, Amish Shah, Benjamin Pierce, Michael Scarpelli, Matthew Seebeck, Arya Tedjasaputra, Dr. Bin Jiang and Dr. Hyuk Park who have all helped in this work.

I would like to thank all the staff scientists at FSMRL who have been kind with their assistance on many occasions. Particularly I would like to thank Dr. Jianguo Wen and Dr. Changhui Lei for assistance with TEM, Doug Jeffers, Steve Burdin and Ernie Sammann for innumerable things, Dr. Scott Maclaren for assistance with AFM, Dr. Vania Petrova for assistance with SEM and STM, Dr. Wacek Sweich for his extended troubleshooting of our RHEED filament, Bharat Sankaran help with sputtering and e-beam, Kevin Colravey for advice on specimen preparation and Jim Brownfield for machining our holders. Finally, I would like to thank the ever friendly head of CMM, Dr. Ivan Petrov, for not only serving on my committee but also for recommending me for the Racheff award.

I owe my thanks to Prof. John Weaver, whose ‘quals’ training I have passed on to many junior students. I would also like to thank my group mates from Prof. John Weaver’s group for their assistance in my first two years in grad school.

I would like to thank Min Yu and Prof. Dallas Trinkle for their DFT simulations of Au-TiO_2 interfaces and Dr. Uli Dahmen for introducing the problem of line tension. I would also like to thank Sergio Sanchez, Matthew Small and Prof. Ralph Nuzzo for their collaboration in writing a paper together.

Finally, my greatest gratitude goes to my family and friends for their support over these years. My parents, brother and wife have been very positive influences during my doctoral study and their support cannot be described by words. Their constant encouragement and motivation always made me feel I was special. Numerous friends in Urbana-Champaign have also helped me in this endeavor. I will cherish their companionship and thank them for helping me in times of need.

TABLE OF CONTENTS

CHAPTER 1

INTRODUCTION

This chapter introduces the study of gold nanocrystals on titania (Au/TiO_2) and the need for advanced transmission electron microscopy techniques to study interfaces of Au/TiO_2. The chapter is organized into three sections. The first section describes the need for studying metal nanocrystals (NCs) supported on oxides as catalysts and the general issues related to the study of supported NCs. The second section analyzes different experimental methods for studying supported NC interfaces. Specifically this section outlines the advantages of aberration corrected electron microscopy for studies on interfaces. The third section introduces the Au/TiO_2 system, including details of unresolved problems in understanding oxidation catalysis by Au/TiO_2. The third section provides a background of studies using Au NCs grown on TiO_2 (110) surfaces.

1.1 Motivation

It was estimated in 2005 by US Climate Science and Technology program that catalyzed chemical processes contributed to nearly $700 billion worth products in a year. The massive figure immediately brings to our mind a picture of how much the world economy depends on catalysis. Starting from hydrocarbon cracking of petroleum products to the detoxification of noxious exhaust gases in millions of automobiles, catalysis assumes dominant if not visible roles in day to day life. The word ‘catalysis’ (which in Greek means ‘breaking down’) was coined by the Swedish scientist Berzelius who in the early part of the 19^{th} century carefully studied the phenomenon of platinum being unaffected during chemical reactions even though it was vital to the chemical reaction. Today, catalysis has come a long way with the synthesis of many different forms of catalysts for various functions. In the broadest sense, these catalysts can be classified

into two categories – homogeneous and heterogeneous catalysts. As the names suggest, homogeneous catalysts are ones which have the same phase as the reactants while heterogeneous catalysts have phases different from the reactants. Bulk of the industrial catalysts in use today is heterogeneous in nature. They form the backbone of oil refining, production of syngas, olefins, aromatics as well vital inorganic compounds such as nitric acid, sulfuric acid etc.[1]

Heterogeneous catalysts come in many different forms – metals, oxides, sulfides, solid acids etc. Of these types, metals form a common component of heterogeneous catalysts for their ability to chemisorb gaseous reactants and break them down to reactive intermediates. For example molecular hydrogen (H_2) spontaneously and exothermally splits into atomic hydrogen on platinum whereas it takes 410 kJ/mol of energy to break the hydrogen molecule into hydrogen atoms in the absence of a catalyst. While the above example illustrates the ability to use metals as catalysts, in order to maximize the potential of metals as catalysts, they need to be finely divided into small particles to increase the available surface area available for catalytic action. Metals in their finely divided form, however, are not stable at high temperatures unless they are affixed to a support that can provide a barrier for metal atom diffusion as well as particle coalescence. For this purpose, oxides find use as stable supports for catalytic metal NCs, which do not degrade at high temperatures. Over the course of time, it was found that oxide supports also performed a significant role in the catalytic mechanism by interacting with the interfacial metal atoms and imparting novel chemical properties to the interfacial metal atoms. Today, oxide supported metal NCs are used as heterogeneous catalysts in production of aromatics, hydrocracking, ethylene oxidation, automobile catalytic convertors etc.[2] A typical three-way automobile catalytic convertor uses for example metallic/alloy NCs (Pt,Pd,Rh etc.) supported on

gamma alumina to simultaneously perform NO_x reduction, carbon monoxide oxidation and oxidation of unburnt hydrocarbons.

The market for oxide supported metal NC catalysts continues to grow and new catalysts are sought for more energy efficient and 'green' processes that reduce environmental pollution. In 2007, the market for just automobile catalytic convertors was in excess of $1.7 billion.[3] In order to keep up with the market demands, scientists have been working to find more efficient, functional, selective and longer-lasting catalysts. One of the thrusts in this direction has been to find alternative oxidation catalysts used in automobile exhaust lines to meet the ever-tightening federal emission regulations. In present day automobiles, Pt/Pd NCs supported on silica, alumina, zinc oxide etc. perform the function of rapidly converting carbon monoxide to carbon dioxide before being released into the atmosphere. However, commercial Pt-group catalysts are not active for CO oxidation below 200^{o}C which leads to the "cold start-up" problem of excessive CO production during incomplete fuel combustion.[4] An alternative to Pt/Pd catalysts are Au NCs supported on reducible oxide substrates such as TiO_2, Fe_2O_3 etc. which promote oxidation catalysis at much lower temperatures than Pt/Pd. Apart from CO oxidation it has been also found that Au catalysts hold promise in catalyzing other reactions such as selective epoxidation of propene[5], ethyne hydrochlorination[6] etc. Further, the oxidation of CO is considered critical to using methanol or hydrocarbons as fuels for fuel cells, where traces of CO can poison the electrodes. Keeping in mind the number of applications, there has been a push to understand the mechanism behind Au catalysis.

In a paper in 1987, Haruta's group demonstrated exceptional catalytic activity for Au NCs supported on semiconducting oxides such as Co_3O_4, NiO and α-Fe_2O_3.[7] Prior to Haruta'a work, other groups also attempted to test the efficacy of Au based catalysts for CO oxidation

without as much success using impregnation of porous oxide substrates with $HAuCl_4$. However, Haruta et. al. showed that by coprecipitating Au NCs and the oxide support from a solution of chloroauric acid and the nitrate of transition metals, it was possible to disperse Au NCs of size less than 5 nm uniformly on oxide supports. This proved vital in producing Au/TiO_2 catalysts with remarkable catalytic activity for CO oxidation to CO_2 even at -70^oC.

Catalysis by Au varies markedly from Pt-group elements. Specifically, the O_2 molecule (O=O) does not spontaneously dissociate on Au to form oxygen atoms whereas O_2 spontaneously dissociates on Pt/Pd to form atomic oxygen species which is a critical step to the reaction mechanism on Pt/Pd. There has been much effort devoted to unraveling the mechanism of Au/TiO_2 promoted oxidation catalysis for more than 20 years now. Many proposals have been put forward to explain the unexpected low temperature activity of Au catalysts; the details are presented in Section 1.3. Despite extensive studies, there is still no agreement on the reaction mechanism.

Some of the fundamental issues in understanding Au NC catalysis stem from a broader problem that experimental methods to probe interfaces of NCs are still inadequate. Much is unknown about NC interfaces. For instance, fundamental questions such as a) "What is the interfacial atomic structure?" or b) "How does the interfacial energy of NCs change with size?" or c) "How much charge transfer happens at NC interfaces?" – have not been answered quantitatively for many systems. The predominant issue with studying NC interfaces relates to the fact that they are buried. Hence, while a large number of experimental methods can be used to study the interior and surfaces of NCs, many of these methods cannot be deployed for studying NC interfaces. The various experimental methods have been compared in Section 1.2.1.

1.2 Experimental Studies of Nanocluster Interfaces

Interfaces play a significant role especially in nanoscale systems. For example, inorganic-organic interfaces form the backbone of colloidal nanoparticle synthesis.[8] However, interfaces in materials are often difficult to study since they tend to be inaccessible to many experimental methods. Determining the structure and chemistry in nanoscale systems is still an unresolved problem [9] and more so in the case of nanoscale interfaces. Section 1.2.1 presents a brief survey of experimental methods used to study structure and chemistry of supported NCs. Particular emphasis is placed on the capability of the experimental probes to study interfaces of supported NCs. Section 1.2.2 provides a brief introduction to aberration corrected electron microscopy as a tool for probing NC interfaces.

1.2.1 Summary of Experimental Methods for Probing Interfaces of Supported Nanoclusters

Multiple microscopic and spectroscopic techniques have been applied to study the structure and chemistry of supported NCs (see Table 1.1). These include Transmission Electron Microscopy (TEM), Scanning Transmission Electron Microscopy (STEM), Scanning Tunneling Microscopy (STM), X-Ray Photoelectron Spectroscopy (XPS), Medium Energy Ion Scattering (MEIS) etc. The strengths and limitations of some of the major experimental techniques for studying interfaces of supported NCs are summarized below.

Table 1.1: Summary of experimental techniques to study supported NCs

Technique	Strengths	Limitations
Structure Determination		
TEM	Atomic resolution real and reciprocal space characterization	Samples must be thin and compatible with TEM
STEM	Atomic resolution real space information, Z-contrast	Same as TEM
STM	Near atomic resolution of top surfaces	Conductive samples only; some electronic structure information can be obtained from interfaces; Limited to top surfaces
AFM	High resolution z-axis imaging of many materials including insulators such as oxides ; Samples can be probed in air	Lower resolution; tip-particle convolution for smaller NCs can lead to artifacts
RHEED	Diffraction information about the structure of an ensemble of NCs or surfaces or both	Cannot analyze individual NCs, no direct real space information
LEED	Diffraction information from 2D surfaces	More of a 2D surface characterization tool; not used in general for NCs
LEEM	In-situ characterization of 2D surfaces; useful for imaging surface steps etc.	Limited resolution; Cannot image interfaces
XRD	In-situ characterization, bulk, surface and interfacial information	Large spot size; limited real space resolution
GIXRD	Diffraction information from surfaces and interfaces	Large spot size

Table 1.1 (Cont.)

Chemical Characterization		
XPS	Surface Sensitive	Cannot probe individual clusters
AES	Surface Sensitive Spatial resolution : ~10 nm	Sampling Depth : 0.5 – 7.5 nm Detection Limits: 0.1 – 5 atom%
MEIS	Surface Sensitive	Cannot probe individual NCs
STS	Surface and interface sensitive Spatial resolution : ~ 2Å	Limited to conductive specimens
EXAFS	Atomic bond distances; Applicable to bulk, surfaces and interfaces	Cannot probe individual NCs
EELS	Surfaces and interfaces sensitive	Limited range of energies for study; Samples must be thin and compatible with TEM

1.2.2 Aberration Corrected Electron Microscopy and Spectroscopy

Electron microscopes are one of the best tools available today to study supported NCs. The electron wavelengths used in transmission electron microscopes (TEM) range from ~0.4 to 4 pm. The highest magnification of a modern TEM is about a few million.[10] It has been consistently observed, however, that the resolution for conventional TEMs is about twenty times worse than their theoretical limits. This discrepancy in resolution is caused by aberrations inherent in cylindrical electromagnetic lenses that arise because of differences in field strength that increase with the distance away from the lens axis. As a result, the electrons traveling most

distant from the axis of cylindrical symmetry are focused more strongly than those traveling closer to the axis. This effect is termed spherical aberration and it ultimately limits the resolution of electron microscopes.[11] The point spread (the formation of a disc in the image from a single point on the object plane) is proportional to the spherical aberration coefficient (C_s) and the square of the off-axis distance divided by the focal length of the lens.

The cylindrical magnetic lenses used in electron microscopes have positive C_s values.[11] Thus, in order to correct the aberration in magnetic lenses, non-cylindrical magnetic lenses with negative C_s values must be employed. A lens capable of meeting this requirement is the thick magnetic hexapole lens, which is composed of three magnetic dipoles.[12] Unfortunately, the hexapole lens, like any other multipole lens system, exerts large low-order aberrations (C_s is a 3^{rd} order aberration) which, if not removed, impose greater limitations on the resolution than the C_s alone.[12, 13] A successful C_s-corrector design for TEM uses two symmetric magnetic hexapoles arranged with the help of two additional round lenses to eliminate each other's lower order aberrations.[13-15] Krivanek and colleagues have developed an alternative C_s-corrector design for STEM dedicated instruments that utilizes a combination of quadrupoles and octupoles.[16, 17]

The C_s-corrector can be positioned either before or after the sample. If placed after the sample, high resolution electron microscopy (HREM) imaging with a resolution of 1 Å or better can be achieved by correcting for the objective lens' aberrations. In HREM, atomic resolution is typically achieved with very thin samples (~few nm). The contrast within an image comes mostly from modifications to the phase of the electron wave by the electrostatic potential of atoms.[18] This contrast is sensitive to both light and heavy atom contributions. Hence lighter elements such as oxygen, carbon etc. can be visualized directly. Positioning the C_s-corrector

prior to the specimen plane, results in the formation of a scanning sub-nanometer electron probe for STEM imaging by correcting for the condenser lens' aberrations. In STEM, the electron probe is used to scan across the sample. As it scans, the electron probe is scattered by atoms in the specimen. Electrons scattered into an annular detector placed after the specimen plane are collected and used to form a rastered image. This mode of imaging is called annular dark-field ADF-STEM.[19] In ADF-STEM, the electron image contrast is approximately proportional to the square of the atomic number (Z) and thickness, when a large inner cutoff angle is used for the ADF detector.[20] This mode of imaging is known as incoherent imaging or Z-contrast. Additionally, the electrons passing through the hole in the ADF detector can be analyzed by electron energy loss spectroscopy (EELS)[21, 22] for high resolution chemical and electronic structure analysis.[23] The combination of C_s-correction and improvements in electron energy loss spectrometers have led to the recent demonstration of atomic resolution chemical mapping[24, 25] and local electronic structure analysis.[26] A more detailed description of TEM, STEM and EELS is provided in the next chapter.

With the advent of sub-Å resolution from Cs-correction it is now possible to not only image atomic structure of interfaces in thin films, grain boundaries, defects etc. with greater precision, but also make quantitative measurements of elemental composition, concentration, electronic structure etc. For example Jia *et. al.* used negative Cs-corrected imaging to measure the oxygen concentration at grain boundaries of perovskite ceramics. Shibata *et. al.* imaged individual yttrium dopants at an alumina grain boundary using Cs-STEM.[27] Klie *et. al.* showed the segregation of impurity atoms to specific locations in the grain boundaries of polycrystalline yttrium barium copper oxide using Cs-Corrected STEM and EELS.[28] Considering the advances made in studies of bulk and thin film interfaces, it is conceivable that Cs-corrected

electron microscopy will also offer new insights to our understanding of NC interfaces. Chapters 3,4 and 5 illustrate this amply for Au NCs supported on TiO_2 (110), where Cs-corrected microscopy and spectroscopy is to understand and interpret the atomic structure, electronic structure, interfacial energy and interfacial line tension of this very important interface.

1.3 Au on TiO_2

Haruta *et. al.* showed that the size of the Au NCs and the choice of support play a crucial role in the catalysis by Au NCs.[7] They showed that Au NCs with sizes smaller than 5 nm were active while larger Au NCs (above 20nm) did not catalyze CO oxidation. Also, unsupported Au NCs (in the powder form) were reported to have very little catalytic activity [7] while the catalysis was much found to be more efficient when Au was supported on reducible transition metal oxides (NiO,Fe_2O_3 etc.). Later on, many research groups have broadly confirmed these findings. The large body of work in this area has been reviewed multiple times in the last two decades.[6, 29-36]

However, despite extensive work in this field, there is no consensus about the reaction mechanism and the catalytically active sites for even a simple reaction such as Au catalyzed oxidation of CO. [6, 31, 37] Two major schools of thought have arisen out of experimental observations that catalytic activity is strongly (a) size dependent and (b) support dependent. Increased catalytic activity from size dependency has been supported by experiments[38, 39] and calculations[40] which suggest that undercoordinated surface gold atoms in smaller NCs are the active sites. Another proposal for the size dependent catalytic activity argues that the appearance of non metallic character in smaller Au NCs (measured by Scanning Tunnelling Spectroscopy (STS)) is responsible for the increased catalytic activity.[41] The support dependency is buffered

by arguments that charge transfer at the interface of the Au NCs[42-44] and favorable reactant adsorption sites on support[37, 45] are responsible for increased catalytic activity.

As noted by Bond[46], it is very difficult to satisfactorily compare the reports from various groups since the details of the experimental variables are often different. After an extensive summary of various works, Bond summarizes that size dependency and support dependency are not separable and consequently should not be treated exclusive of each other. Bond goes on to propose a model[37] for Au promoted catalysis of CO where CO molecules bind to under-coordinated surface sites at the Au NC surface. The defects in the oxide support provide binding sites for oxygen and the reaction is mediated by $Au^{\delta+}$ species that is hypothesized to exist at the interface. Experimentally, it has been shown using Mössbauer spectroscopy that both Au^0 and $Au^{\delta+}$ are present in active catalysts.[47] However, the precise location of the $Au^{\delta+}$ species could not been identified. As a result, the presence of $Au^{\delta+}$ species at the interface of Au NCs remains to be experimentally verified.[6]

One of the difficulties with studying the precise nature of the interfacial Au sites is that real catalysts tend to be difficult to characterize using microscopy and spectroscopy techniques. Hence, many researchers have resorted to studying NCs supported on flat, well-defined supports for solving fundamental problems in catalysis.[48] In case of Au NC catalysis, TiO_2 has garnered a lot of attention as a model support because the surfaces of TiO_2 have been extensively researched and well understood, especially for the TiO_2 (110) surface.[49] The subsequent sections describe TiO_2 surfaces and studies of Au NCs supported on well defined 2-D TiO_2 surfaces.

1.3.1 Surface Studies of TiO_2 (110)

TiO_2 crystallizes in three major forms – rutile (tetragonal, D_{4h}^{14}-$P4_2/mnm$, a = b = 4.584 Å, c = 2.953 Å)[50], anatase (tetragonal, D_{4h}^{19}-$I4_1/amd$, a = b = 3.782 Å, c = 9.502 Å) and brookite (rhombohedrical, D_{2h}^{15}-Pbca, a = 5.436 Å, b = 9.166 Å, c = 5.135 Å).[51] Most of the model studies on catalysts use rutile TiO_2. For this reason, all further discussions will pertain only to rutile TiO_2. In the tetragonal lattice of rutile TiO_2 (Figure 1.1), the unit cell consists of two titanium atoms at (0,0,0) and (½, ½, ½) and four oxygen atoms at ±(x,x,0) and ±(½+x, ½–x, ½) where x = 0.306.[50]

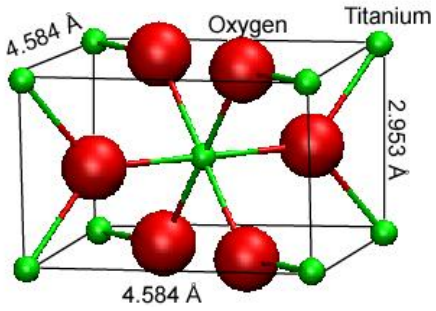

Figure 1.1: Unit cell of rutile TiO_2

Surfaces created in oxides can be predicted following autocompensation criteria such that the surface truncation creates no unbalanced charges.[52] In rutile TiO_2, the (110) surface is thermodynamically most stable.[53] By autocompensation rules, the (110) surface is terminated by oxygen atoms that are two-fold coordinated to titanium atoms (Figure 1.2).[49] These oxygen atoms are termed as bridging oxygen (O_{br}). The atomic layer immediately below O_{br} is termed as the basal plane. There are two kinds of Ti atoms in the basal plane – five-fold coordinated Ti (5-c TiO_2 in Figure 1.2) bonded to four in-plane O atoms and one out of plane O atom and the six-

fold coordinated Ti (6-c TiO_2 in Figure 1.2) bonded to two in-plane O atoms , two O_{br} and two O atoms below the basal plane. The coordination of 6-c Ti is similar to Ti atoms in bulk rutile TiO_2.

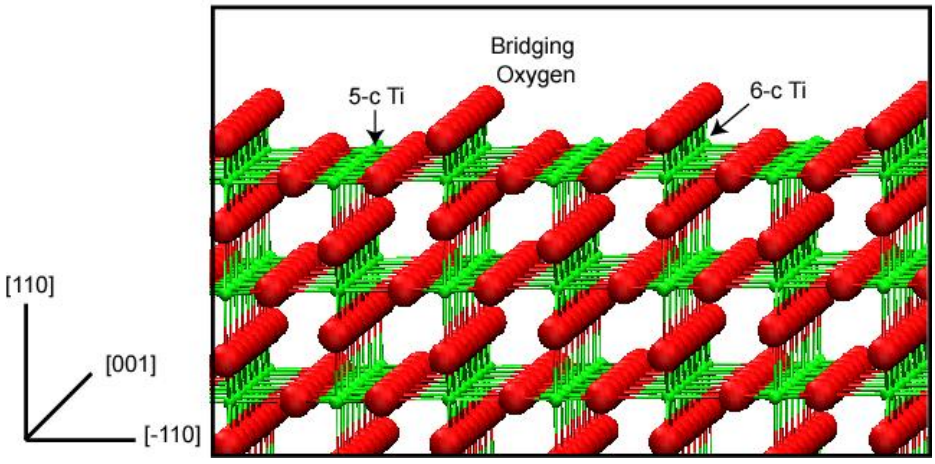

Figure 1.2: (110) surface of rutile TiO_2 viewed along TiO_2[001]

The (1x1) surface of TiO_2 (110) shown in Figure 1.2 is thermodynamically stable at room temperature in ultra high vacuum (UHV). Under mildly reducing conditions the bridging oxygen atoms can be removed resulting in surface oxygen vacancies. Under harsher reducing conditions, TiO_2 (110) can restructure into a number of possible reconstructions such as (1x2), (1x3), rosettes etc.[49] The atomic positions in these reconstructions have been experimentally using Scanning Tunneling Microscopy (STM) and confirmed using Density Function Theory (DFT) calculations. One of the (1x2) reconstructions observed under reducing conditions is shown in Figure 1.3. In this model, which was proposed by Pang *et. al.*, there are no bridging oxygen atoms and every alternate column of 4-c Ti atoms and subsurface O atoms immediately below the 4-c Ti atoms are absent resulting in a (1x2) reconstruction. (Figure 1.3).[54] A salient feature of this reconstruction is that the positions of Ti and O atoms at the surface do not differ from unreconstructed TiO_2 (110). Depending on the surface preparation technique, other kinds of

atomic rearrangements leading to (1x2) reconstructions have also been shown to be stable on reduced TiO_2 (110).[55, 56]

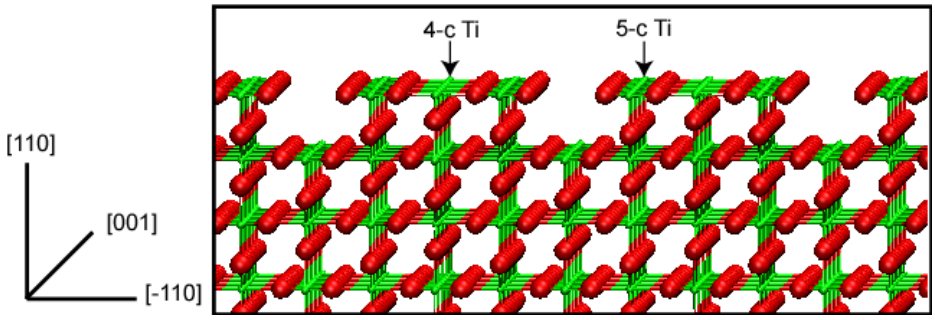

Figure 1.3: (1x2) reconstruction of TiO_2 (110) proposed by Pang *et. al.*

Upon metal deposition onto TiO_2, metals generally reduce the substrate and themselves become oxidized according to the reaction –

$$M + TiO_2 \rightarrow MO_x + TiO_{(2-x)}$$

if the reaction is thermodynamically favorable.[57] For metal overlayers deposited on TiO_2, only those metals whose oxides' heat of formation is below 250 kJ/mol do not undergo oxidation. However some of the metals (Pt, Pd etc.) that resist oxidation undergo another phenomenon at elevated temperatures known as encapsulation – where a layer of TiOx grows over the metal NCs.[49] This effect is commonly termed as Strong Metal Substrate Interaction (SMSI) in the catalyst community.[58] Among the metals grown on TiO_2, only Au, Cu and Ag do not suffer from oxidation, interdiffusion or encapsulation (SMSI) on most TiO_2 supports.[49] The nucleation and growth of Au on TiO_2 (110) is discussed further in the next section.

1.3.2 Growth of Au NCs on TiO_2 (110)

On a defect-free TiO_2 (110) surface, multiple reports suggest that a Au atom binds preferentially to either a 5-c Ti atom on the basal plane, or atop O_{br}.[42, 59] The two sites were found to have nearly the same binding energy for Au adsorption.[42, 59] However, the binding of Au-O_{br} is weak compared to the binding of other transition metals in the same group namely Cu and Ag. For instance, the binding energy of Au-O_{br} is lower than Ag-O_{br} or Cu-O_{br} by more than 1 eV.[60] As a result, the adhesion energy of larger Au coverage on oxidized defect-free TiO_2 (110) is very weak.[61]

However, in the presence of O_{br} vacancies, Au atoms preferentially bind to O_{br} vacancies ($O_{br\text{-}v}$).[62] The binding energy of a Au-$O_{br\text{-}v}$ is reduced by ~0.45 eV compared to Au-O_{br}.[62] As a result Au readily nucleates on $O_{br\text{-}v}$ at lower coverages.[62] UHV studies show that Au nucleation on defect sites (including $O_{br\text{-}v}$) on TiO_2 (110) leads to 2D growth for lower Au coverage (<0.1 ML) at room temperature.[63] Low Energy Ion Scattering (LEIS) and STM studies have confirmed that Au grows as 2D clusters for Au coverage less than 0.1 ML.[63-65] The 2D clusters are rectangular and elongated along the TiO_2 [001] direction which has a close lattice match to the Au [110] direction.[65] These rectangular 2D Au clusters are only 1-2 atomic layers tall and less than 2 nm wide.[65] With increasing Au coverage at room temperature, Au clusters become quasi-2D shaped (diameter = 1.5 - 2.5 nm), hemispherical 3D shaped (diameter = 2.5 - 4 nm) and eventually spherical 3D shaped (diameter > 4nm).[63] Upon annealing to high temperatures, the clusters transform irreversibly to the 3D morphology.[63]

The 3D growth of Au NCs on TiO_2 (110) can be understood from the following equation, which provides a rough estimate for predicting the growth mode of supported NCs. When,

$$\gamma_{Interface} > \gamma_{Substrate} - \gamma_{Metal}$$

metal NCs adopt 3D shapes (Volmer-Weber growth). The surface energy of Au (111) – which is lowest amongst the surfaces of Au – was calculated to be 1.283 J/m^2.[66] The surface energy of TiO_2 was measured to be 0.28-0.38 J/m^2 from a liquid drop measurement.[67] A DFT calculation from a (1x1) terminated TiO_2 (110) surface gave 0.35 J/m^2 for the surface energy of TiO_2 (110).[68] Since $\gamma_{TiO2(110)}$ is much lesser than γ_{Au} and since $\gamma_{Interface} > 0$, Au always forms 3D NCs for larger NC sizes.

Au growth on TiO_2 (110) at room temperature in UHV results in relatively poor epitaxy.[63] Annealing to 775K was results in faceted epitaxial Au clusters (> 100 nm) with Au $(111)_{[-110]} \parallel TiO_2\ (110)_{[001]}$. Similar epitaxial relationship was reported for Au NCs grown by deposition precipitation and gas phase grafting methods followed by heating to 300^{o}C in air.[69] Au growth at high temperatures results in faceted epitaxial Au clusters (> 100 nm) with Au $(112)_{[-110]} \parallel TiO_2\ (110)_{[001]}$.[70] In most cases, Au [110] orients along TiO_2 [001] since there exists a reasonable lattice match ($d_{Au(110)}$ = 2.885Å and $d_{TiO2(001)}$ = 2.953 Å).

1.4 Summary

In this work we have attempted to address some of the fundamental questions that are still controversial in the growth of Au NCs TiO_2. Chapter 2 details the experimental techniques used in our studies. In chapter 3 we have investigated the driving force behind the epitaxy of Au NCs on TiO_2 (110) by studying the formation of epitaxial Au NCs on unreconstructed and reconstructed TiO_2 (110) using RHEED. For comparison, we have also studied Ag NCs on TiO_2 (110) and show the broad differences between Ag and Au which are structurally identical but chemically dissimilar. In chapter 4, we have studied the interfacial atomic structure of a specific

epitaxy of Au on TiO_2 (110) that has a large adhesion energy on TiO_2 (110). Using aberration corrected STEM we have shown that there exists a special interfacial structure which is responsible for the enhanced adhesion. In chapter 5, we have probed the non-self similarity of NC shapes for a specific class of epitaxial Au NCs that dewet from the support at smaller sizes. We have modeled this phenomenon by invoking the effect of interfacial line tension at the three phase interface of Au, TiO_2 and air. By suitably fitting the data to the model, we have also measured a lower limit to the value of interfacial line tension, thereby laying out a framework for measuring interfacial line tension in supported NCs. In Chapter 6, the conclusions from this work have been laid out and some future directions have been proposed.

CHAPTER 2

EXPERIMENTAL METHODS

This chapter introduces the experimental techniques used in this thesis to probe Au NCs on TiO_2. The chapter is organized into four sections. The first section describes the basics of image formation in a Scanning Transmission Electron Microscope (STEM). This section also describes electron probe formation in an aberration corrected STEM and the details of the typical experimental settings used for imaging in the JEOL 2200FS STEM installed in CMM-MRL. The second section describes electron energy loss spectroscopy (EELS) in the STEM mode and the conditions used for obtaining high quality EELS data from the JEOL 2200FS STEM. The third section describes high resolution transmission electron microscopy (HRTEM) and the issue of specimen thickness complicating the phase contrast in HRTEM. The fourth section describes the specimen preparation methods used in creating equilibrium shaped NCs supported on atomically flat terraces of TiO_2 (110) for TEM/STEM imaging and EELS.

2.1 Image Formation in a Scanning Transmission Electron Microscope

A brief introduction to Scanning Transmission Electron Microscopy (STEM) was provided in the previous chapter. This section aims to elaborate the physical principles behind image formation in a STEM. The origin of the modern STEM traces back to Albert Crewe and colleagues working in Argonne National Laboratory towards construction of a STEM fitted with a high brightness field emission electron source. Using the reciprocity theorem, Crewe et al. showed that the ultimate resolution of a STEM operating under equivalent conditions (of high voltage, lens aberrations etc.) will be similar to conventional TEM (CTEM).[71] In the first demonstration of atomic resolution STEM, uranium and thorium atoms were imaged on a carbon

film.[72] In this demonstration, an annular detector (termed as ADF detector for annular dark field detector) subtending a half angle of 20 to 200 mrads below the specimen was used to collect 90% of the scattering. That is, the image was formed by collecting both elastically and inelastically scattered electrons between 20 and 200 mrads but excluding all beams that scatter less than 20 mrads. The scattered intensity was found to be proportional to $Z^{3/2}$, which was attributed to the $Z^{3/2}$ dependence of the total elastic scattering cross section.[73] The images obtained by this technique were seen to exhibit a key feature of 'incoherent imaging', i.e. the lack of contrast reversals.[74] (Under coherent imaging conditions, the image-contrast of a thin specimen can be reversed by a change in focus due to the strong interference effect. Incoherent imaging refers to the imaging condition in the absence of the strong interference effect.) However, for crystalline specimens whose thicknesses were several tens of nanometers it became apparent that contrast reversals were present for images formed from low-angle scattered electrons as expected from coherent scattering theory.

Howie proposed the idea for incoherent imaging which involved the complete exclusion of all Bragg diffracted beams by increasing the inner collection angle.[20] The original proposal by Howie was aimed at conclusively identifying metal catalysts supported on partially crystalline supports where elastic scattering from the crystalline support showed up strongly in the images formed with low-angle scattered beams. It was realized that the contribution to higher angle electron scattering was mostly from thermal diffuse scattering (TDS), i.e. electron-phonon scattering. TDS can result in large momentum transfer and is usually accompanied by very little energy loss. Therefore TDS can be observed at much higher angles than Bragg diffraction. While elastic scattering falls off as the square of the atomic scattering factor ($f^2(u)$), first-order TDS is proportional to the product of the angular distance from the center and the atomic scattering

factor squared ($u^2f^2(u)$).[75] The elastic mean free path of TDS is 100-200nm which is of the same order as plasmon scattering.[76] Therefore TDS is very much prevalent in crystalline specimens. Also, electrons scattered at high angles have intrinsically small impact parameters with the atomic nuclei in the specimen. For example, the impact parameters at 50 mrad is 0.12 Å which is less than the typical atomic vibration amplitude.[77] As a result, electrons scattered to high angles see crystal atoms behaving as a random assembly of scattering centers whose scattering cross section approaches the Z^2 dependence of Rutherford scattering in comparison to the $Z^{3/2}$ dependence of the total elastic scattering cross-section .[77] The incoherent scattering phenomenon does not prevent STEM imaging of crystallographic specimens. In thicker crystalline specimens where dynamic diffraction is often strong, the electron waves channel preferentially along atomic columns. Thus the number of high angle scattered electrons along atomic columns increases proportionately thus producing Z-contrast images of even thicker crystalline specimens. The detector which is used to collect the high-angle electron scattering is known as the high-angle annular dark field (HAADF) detector (Figure 2.1). HAADF is routinely used nowadays in atomic resolution imaging of crystalline specimens.

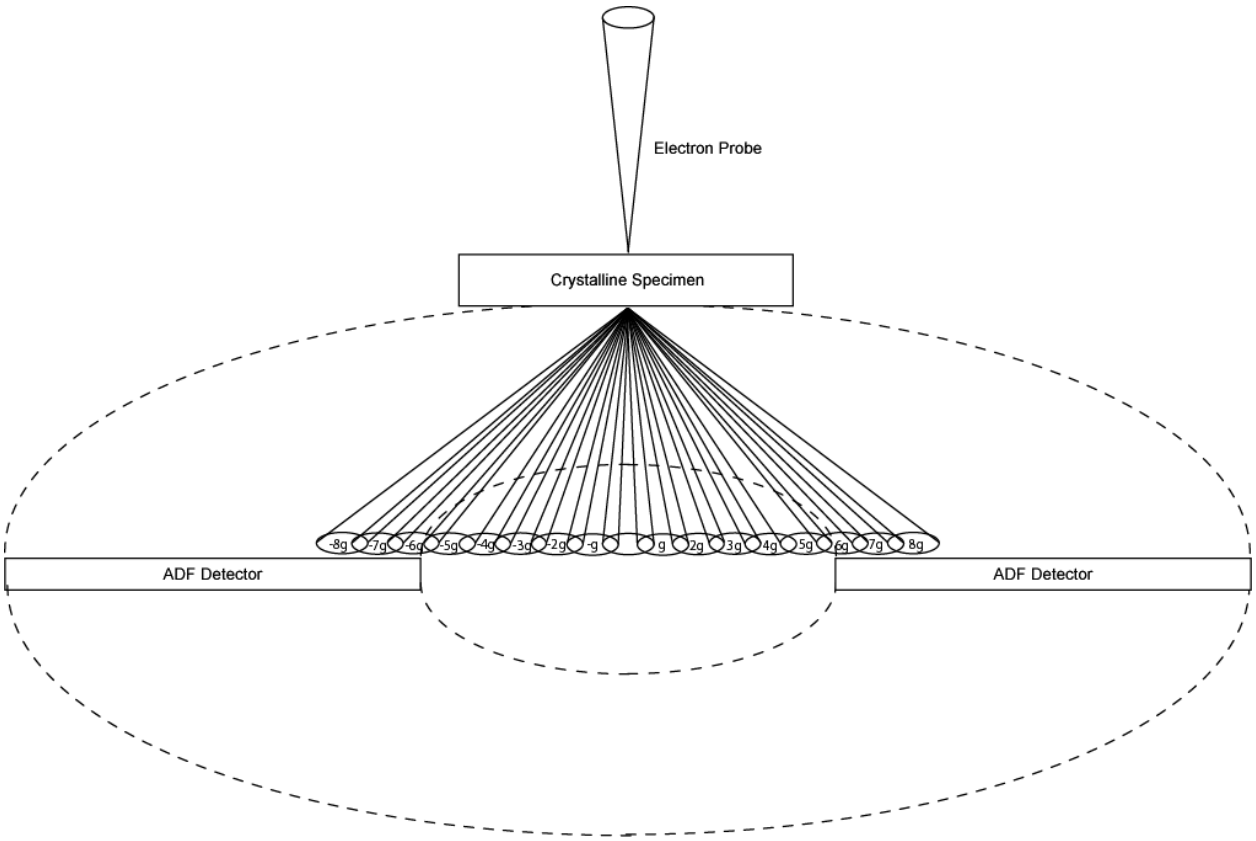

Figure 2.1: Schematic of the STEM geometry. The HA-ADF detector typically collects electrons scattering between 60 and 300 mrad. The first bragg diffraction for Au(111) scatters to 10.6 mrad for comparison.

One of the key factors that determine the resolution in a modern STEM is the size of the electron probe. Hence it is worthwhile to discuss probe formation in a STEM. The wavefunction of the probe (Ψ_{Probe}) is computed as the convolution of the wavefunction of the electrons at the "effective" source (Ψ_{Source}) and product of the lens transfer function and aperture function. In a simple 2 lens system, the effective source is the image of the electron filament after demagnification by the condenser 1 lens.

$$\Psi_{Probe} = \Psi_{Source} \otimes (\text{Transfer Function} * \text{Aperture Function}) \quad (2.1)$$

where,

$$\text{Transfer function} = (e^{-i\chi}) \tag{2. 2}$$

$$\text{Aperture Function} = A(\mathbf{k}) \tag{2. 3}$$

where,

$$\begin{aligned}\chi(\omega)) = \frac{2\pi}{\lambda}\{\ \mathrm{Re}\ (\ & \frac{1}{2}\bar{\omega}^2 A_1 + \frac{1}{2}\omega\bar{\omega}C_1 + \frac{1}{3}\bar{\omega}^3 A_2 + \omega^2\bar{\omega}B_2 \\ & + \frac{1}{4}\bar{\omega}^4 A_3 + \frac{1}{4}(\omega\bar{\omega})^2 C_3 + \omega^3\bar{\omega}S_3 \\ & + \frac{1}{5}\bar{\omega}^5 A_4 + \omega^3\bar{\omega}^2 B_4 + \omega^4\bar{\omega}D_4 \\ & + \frac{1}{6}\bar{\omega}^6 A_5 + \frac{1}{6}(\omega\bar{\omega})^3 C_5 + \omega^4\bar{\omega}^2 S_5 \\ & + \omega^5\bar{\omega}D_5 + \ ...)\}\end{aligned} \tag{2. 4}$$

and $\omega = 1/f(x + iy)$, where x, y are real space coordinates. The above terminology is derived from Haider et al.[78] where A_1 = Two-fold astigmatism, C_1 = Defocus, A_2 = Three-fold astigmatism, B_2 = Coma, A_3 = Four-fold astigmatism, C_3 = Cs = Spherical Abberation, S_3 = Two-fold star aberration, A_4 = Five-fold astigmatism, B_4 = Coma, D_4 = Three-lobe aberration, and A_5 = Six-fold astigmatism. In the above equation, C_3 and A_1 are the most dominating aberrations. A_1 which is the two-fold stigmatism can be easily corrected using the objective stigmators even in a TEM. Correction of C_3 is not possible in an uncorrected TEM and needs an aberration corrector to accomplish this task. Therefore in uncorrected TEMs, the aberration function can be approximated to be solely a function of C_3 and A_1. In aberration corrected TEMs, the effect of higher order aberrations on the aberration function is seen since C_3 is nearly zero and the contrast becomes a function of higher order aberrations in this case.

The effect of the various aberrations leads to a broadening of the probe. The JEOL 2200FS in CMM-FSMRL is equipped with an aberration corrector that is capable of correcting aberrations up to third order. The aperture function also determines the probe size and probe

current. For a given aperture size and C_5 the optimum defocus and spherical aberration was found to be (in the absence of two-fold astigmatism and coma) [78] –

$$C_1 = 0.144\omega_A^4 C_5 \quad (2.5)$$

$$C_3 = -0.92\omega_A^2 C_5 \quad (2.6)$$

where ω_A is the half angle subtended due the condenser aperture at the specimen. For the JEOL 2200FS microscope at CMM-MRL, the aperture cutoff angles ω_A were measured to be[79]

Condenser Aperture	**Diameter (μm)**	**Convergence half angle - ω_A (milliradians)**	**Probe Current (pA)**
#2	40	36.88	
#3	30	26.61	30
#4	20	16.8	13

Table 2.1: List of aperture sizes and convergence half angles for condenser apertures in JEOL 2200FS at CMM-MRL

Figure 4 in Haider et. al.[78] shows the simulated beam profile for aperture sizes similar to #2, #3 and #4 with C_1 and C_3 set to the optimum values as described by the equations above. The probe size is often reported as the full width at 59% maximum (FWHM) of the probe beam intensity ($\Psi_{Probe}\,\Psi^*_{Probe}$).[78] It can be seen that the probe size becomes smaller with decreasing aperture size when the product of Cc and ΔE is 1.5. This resembles the condition in our microscope where Cc ~ 1.4 mm and ΔE = 1.0 eV.[79] It is also seen that both CL#3 and CL#4 can achieve sub-angstrom resolution when residual aberrations are set to zero. For high resolution STEM in our microscope, CL#3 or CL#4 can be used depending upon the resolution

and signal to noise ratio constraints (CL#3 provide a higher probe intensity and CL#4 provides a slightly better resolution). Other settings to be kept in mind during HR-STEM imaging are the spot size and camera length. Spot size is controlled by the strength of the condenser 1 lens which forms a demagnified image of the source. During the demagnification, some of the intensity is lost thus resulting in weaker intensity for smaller probe sizes. A smaller spot size results in higher resolution but lower signal to noise ratios. During typical HRSTEM imaging, spot "3C" in "MAG" mode and a camera length of 60cm are found adequate to achieve sub-1Å resolution.

The formation of an image by summing inelastically scattered electrons at the HAADF detector can be quite complicated to describe for many specimens. A reasonable approximation image formation at the HAADF detector is that the measured intensity is proportional to the probe intensity times the atomic scattering cross section. A simple model for scattering cross section using the Einstein model for crystalline specimens is given by[80, 81]

$$\sigma_{HAADF} = \left(\frac{4\pi m}{m_0}\right)\left(\frac{2\pi}{\lambda}\right) \int_{HAADF} \left| f(s)\left(1 - e^{-2M_x(s)}\right) \right|^2 d^2 s \tag{2.5}$$

where $s = \theta/2\lambda$, λ = wavelength, θ = scattering half-angle, f(s) is the atomic scattering factor and $M_x(s)$ is the Debye factor. The upper ADF detector in JEOL 2200FS has an inner cut-off angle of ~100 mrad for a 60cm camera length[79] which is sufficient for avoiding diffraction contrast effects in the HAADF image as discussed above. All images reported in this work were recorded with spot "3C", CL#4 and camera length = 60cm. The HAADF detector also has "brightness" and "contrast" settings that can be adjusted for optimum image clarity. These functions control the post-acquisition electronics of the HAADF detector and do not fundamentally alter the sensitivity of the hardware to scattered electrons.

2.2 Electron Energy Loss Spectroscopy in a Scanning Transmission Electron Microscope

The transmission of probe electrons in a TEM through a specimen leads to inelastic interactions where the probe electrons lose energy to certain processes in the specimen. The dominant inelastic losses arise from the excitation of plasmons and phonons. Plasmon losses typically range from 0-50 eV. Phonon losses form a continuous exponentially decreasing background over the entire range. The exponential background arises from energy loss due to multiple phonon scattering events in the specimen. Intraband losses from core levels (core-loss edges) typically occur above ~50 eV. Useful core loss information extends out to 1000eV beyond which there is little signal to make meaningful observations.

EEL spectra are obtained by dispersing the inelastically scattered electrons according to their energy loss using a energy-loss spectrometer. The spectrometer consists of a magnetic prism which bends the electrons differently according to their energies. The energy dispersed electron beams are then refocused and simultaneously spatially separated on a scintillator where the electrons are converted to photons. The photons are read out using a photodiode array coupled to the scintillator using fiber-optics. The two most common energy filters are the GIF (Gatan Imaging Filter) and the in-column Omega (Ω) filter (so named because of the Ω shaped arrangement of magnetic prisms). The GIF is a post-column energy filter that is located below the TEM viewing screen. The back focal plane of the last projector lens is the image plane for the GIF. The Ω filter is an in-column energy filter. It is located between the intermediate and projector lenses. The back focal plane of the intermediate lens (sometimes termed as the first projector lens) is the object plane for the Ω filter in the “image mode”.

The JEOL 2200FS at CMM-MRL is fitted with an in-column Ω filter. An entrance aperture is located above the Ω filter to limit the angular spread of electron beams entering the Ω

filter. We used an acceptance half-angle of ~42 mrad for collecting the EEL spectra. An energy selection slit is placed in the spectrum plane below the Ω filter for forming energy filtered diffraction patterns and energy filtered TEM (EFTEM) images. While the energy slit is not used during EELS acquisition, it is used prior to EELS collection for aligning the Ω filter. During EELS acquisition, a diffraction pattern is formed at the back focal plane of the intermediate lens (object plane for the Ω filter). The magnification of this diffraction pattern (camera length) determines the collection angle for collecting energy loss data.

While conventional STEM imaging is performed at a camera length of 60cm in our microscope, this setting does not permit enough electrons to be available for high quality core-loss EELS. Hence, for obtaining core-loss EELS, we use a camera length of 20cm. Also, in order to increase the signal to noise ratio of the EEL spectra we use spot "3C" in the "AMAG" mode which results in a probe current of 160 pA. At these settings the best energy and spatial resolution are about 0.9 eV and 0.11nm respectively.[79] It must be noted that large probe currents can cause specimen damage and must be therefore used with caution for beam sensitive specimens. We observed that repetitive scans on the same atomic columns did cause specimen damage in TiO_2. We minimized specimen damage by choosing the smallest possible integration times for high quality EELS.

The energy resolution of an EEL spectrum is a function of the energy spread of the electron gun (due to ripples in high tension and current supply), chromatic aberration of the condenser lenses as well as the energy resolution of the energy filter. The best energy resolution obtained in our microscope is ~0.6 eV under specific conditions (that are not normally used in day-to-day core-loss EELS operation).[79] The energy resolution in EELS can be further improved using monochromators[82, 83], cold-field emission guns[84] etc.

2.3 High Resolution Transmission Electron Microscopy

High resolution transmission electron microscopy (HRTEM) is a vast subject in itself. One cannot do justice to the details of the subject in a short space. Therefore, only a brief introduction will be given in this section. More information can be found in well-established TEM textbooks.[10, 18, 73, 85, 86] After introducing HRTEM, a detailed discussion will ensue to describe the strengths and weaknesses associated with HRTEM for studying supported NCs and their interfaces.

In a TEM, an image is formed by first illuminating the specimen with a nearly parallel beam of electrons and then by bringing together the scattered electrons using the objective lens to form an image. This process is schematically illustrated below in Figure 2.2 for a crystalline specimen and an objective lens with no aberrations.

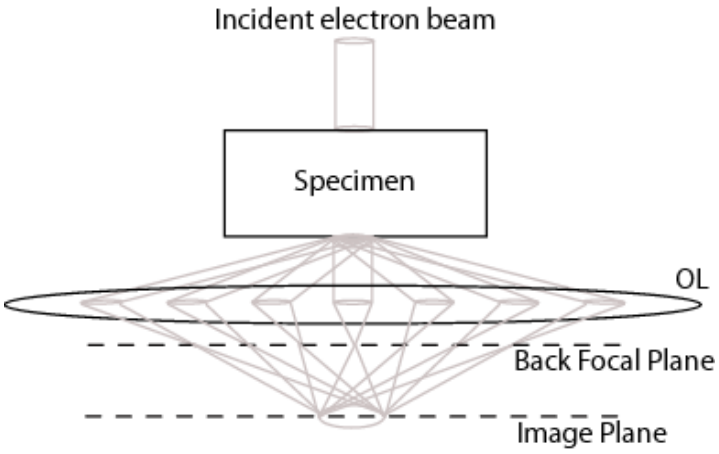

Figure 2.2: Schematic of image formation at the objective lens of a TEM

Figure 2.2 shows that electrons exiting from the crystalline specimen interfere constructively in a periodic manner to produce scattered electrons only along certain defined paths. The objective lens brings together the diffracted beams by bending the electron beams

towards the optical axis. Since Figure 2.2 assumes an objective lens with no aberrations, all the electron paths are shown to overlap perfectly at the image plane. Objective lenses used in TEMs however always have aberrations and bend farther deflected electrons further towards the optic axis – an effect called spherical aberration. Because of spherical aberration, all the electrons never overlap perfectly at any plane resulting in a smearing of information at the image plane. This smearing can be mathematically written as –

$$g(r) = \int f(r')h(r - r')dr' \tag{2. 7}$$

$$= f(r) \otimes h(r - r') \tag{2. 8}$$

where f(**r**) represents the specimen, g(**r**) represents the image and h(**r**) represents the nonlocal contributions to image formation due to lens aberrations. Using Fourier transforms, the above equation can be equivalently and more conveniently written as –

$$G(\boldsymbol{u}) = F(\boldsymbol{u})H(\boldsymbol{u}) \tag{2. 9}$$

where G(**u**), F(**u**) and H(**u**) are the Fourier coefficients of g(**r**),f(**r**) and h(**r**) respectively.

H(**u**) is the (complex) contrast transfer function and describes how information from the specimen (F(**u**)) is altered and represented as information in the image (G(**u**)) in HREM. H(**u**) is made of three factors – objective lens aberration function (B(**u**)), objective aperture function (A(**u**)) and the envelope function (E(**u**)). A(**u**) and E(**u**) function by cutting off spatial frequencies beyond a certain upper limit of **u**. The lens aberration function B(**u**) has already been described in equations 2.2 and 2.4. The complex dependence of B(**u**) results in a non-intuitive lens aberration function at different lens defoci. Assuming astigmatism can be nearly eliminated, B(**u**) is largely dependent only the defocus (C_1) and spherical aberration (Cs) in uncorrected lenses. A typical Cs for uncorrected lenses is 1mm. With the addition of an aberration corrector

below the objective lens, the effective Cs of the objective lens can be brought down to the order of microns (μm). In aberration-corrected lenses, since Cs is of the order of microns, the effect of higher order aberrations on B(**u**) become comparable and results in more non-intuitive transfer functions. In aberration-corrected lenses, estimation of B(**u**) demands complete knowledge of higher order aberration coefficients.

Assuming everything about the contrast transfer function (H(**u**)) is known, we turn our attention to the description of the specimen function (f(**r**)). For a thin specimen, it is often approximated that the specimen plays the role of a phase object and only weakly alters the phase of the incident electron beam without causing any change to the amplitude. This approximation is known as the Weak Phase-Object Approximation (WPOA). Image analysis under the WPOA approximation allows for nearly intuitive image interpretation under optimum lens conditions. However, for larger specimen thicknesses WPOA does not hold and multiple-scattering events (dynamical diffraction) have to be taken into account in understanding the exit-wave and consequently the image formation. Multiple scattering can be simulated using multi-slice methods [86] which is however non-intuitive and requires reasonable computing power.

Most of the specimens used in our study were 30nm or more in thickness. At these thicknesses, WPOA cannot be used to estimate the exit wave and the image contrast becomes complicated as shown in Figure 2.3 below. In the HRTEM image of a Au NC supported on TiO_2 (Figure 2.3), the contrast at the surface changes quickly upon moving towards the interior of the substrate. The hatched box shows that for a unit cell of the rutile lattice, the contrast is dissimilar even between successive layers close to the surface. This presents a huge challenge when it comes to structure determination of the interface of Au-TiO_2 where the exact substrate thickness

is not known. A further challenge is the inability to intuitively identify the interfacial atomic positions due to the complicated contrast.

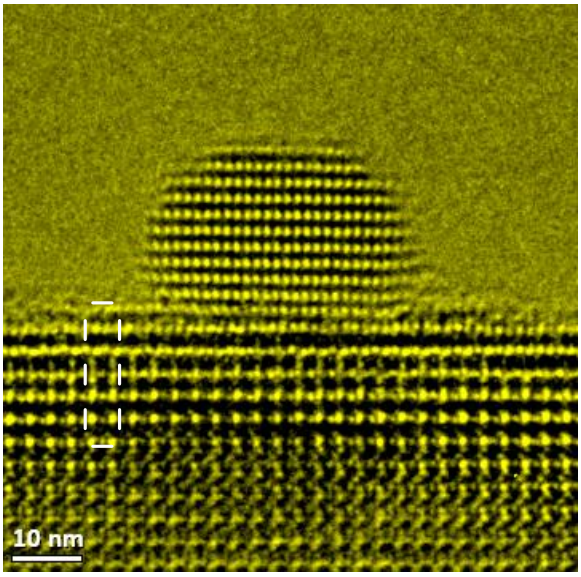

Figure 2.3: HRTEM image of a Au NC supported on TiO_2. The contrast at the TiO_2 surface changes quickly upon progressing towards the interior of the substrate. The hatched box is a guide to the eye and shows that contrast is dissimilar even between successive layers close to the surface.

The complicated HRTEM contrast can be better interpreted by reconstructing the exit wave function. Exit wave reconstruction can be accomplished by taking multiple (alteast three) images at various defoci and iteratively obtaining the exit electron wave by post processing. However, for thick specimens such as the ones we use for our experiments (Figure 2.3), exit wave reconstruction is often very challenging since reconstruction algorithms cannot function correctly when there are phase jumps (arising from thickness) between focal series images.

Because of the complications associated with interfacial contrast of supported NCs imaged using HRTEM, we preferred HRSTEM imaging. For supported NCs, HRSTEM allows direct measurement of shape of NCs as well as identification of individual atomic positions with

ease. Nevertheless with better specimen preparation methods and simulations HRTEM can provide information about interfacial binding and interfacial oxygen atoms which are outside the realm of HRSTEM. Also, for strain measurements, HRTEM is better than HRSTEM since specimen drift is an issue with scanning images.

2.4 Sample Preparation of Supported Au NCs on TiO_2 (110)

For successful TEM/STEM characterization of nanocrystal (NC) interfaces and NC shapes, model NCs must be prepared such that –

a) NCs are in cross-sectional geometry.
b) The support is thin enough for TEM/STEM observation (< 100nm).
c) The facet supporting the NC must be well defined and flat.
d) The interface of NC and support facet must be produced reproducibly.
e) NC surface and interface should not be altered by sample preparation methods.

Prior to this work, many groups have used cross-sectional TEM sample preparation to image supported nanoclusters. However NCs prepared using cross sectional TEM images are questionable when it comes to structure determination of small NCs because specimen preparation typically involves burying the clusters in polymeric materials and ion milling of the specimen. These procedures alter the surface chemistry and may cause atomic rearrangement, thereby altering the shape, surfaces and the interfaces of the nanoclusters.

We prepared pristine Au NCs on atomically flat TiO_2 terraces in the cross-sectional geometry using the following methods. We first prepared electron transparent (<100nm) TiO_2 regions in a rutile TiO_2 (110) single crystal (MTI Corporation) by dimpling a 3mm disc of the single crystal followed by ion-milling (GATAN PIPS) at 5keV. After ion-milling the crystal

turned olive green and resulted in the production of leaf-like features that were TEM transparent (Figure 2.4).

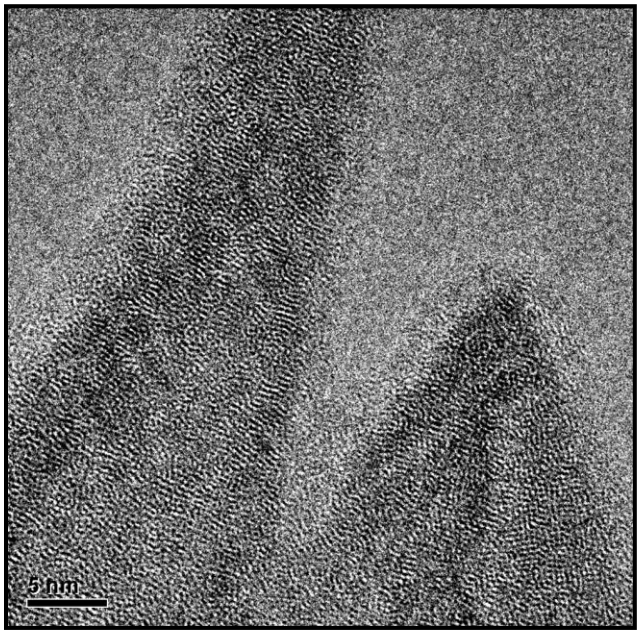

Figure 2.4: TEM image of amorphous TiO_2 after ion milling

The ion-beam damage was removed by heating the olive green TiO_2 disc in an air furnace at 1000^{o}C for 30 minutes and cooling at ~1^{o}C/minute. The crystal turned light yellow after annealing. The annealing also produced extensive electron transparent regions in the crystal with (110) faceted edges. Figure 2.5 shows a single crystalline TiO_2 that has been thinned to become TEM transparent after annealing in air to 1000^{o}C for 30 minutes. The grey region on the top and bottom of the image is empty space.

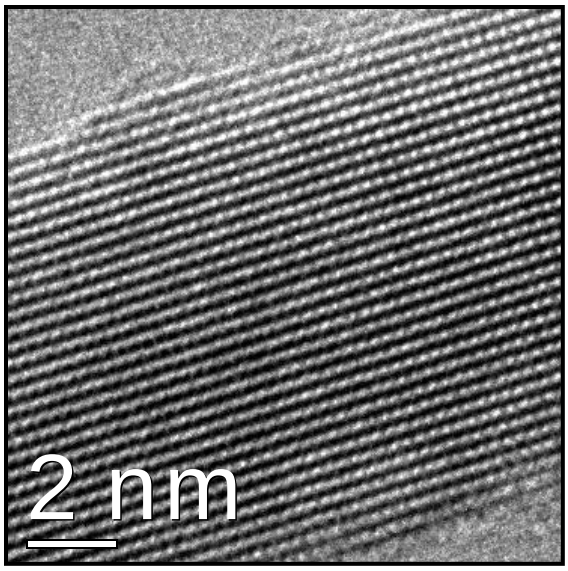

Figure 2.5: TEM image of crystalline TiO_2 after annealing

Prior to gold deposition, the substrate was cleaned in oxygen plasma (20torr, 100W) for a minute. Gold was then sputtered onto the TiO_2 substrate in a vacuum chamber (~$5x10^{-7}$ torr) at room temperature. The sample was then removed from the vacuum chamber and heated to desired temperatures (up to 700^{o}C) in an air furnace to promote NC growth and formation of the equilibrium shape in an ambient environment. This procedure produced single crystal Au NCs supported on facets of TiO_2(110) as shown in Figure 2.6.

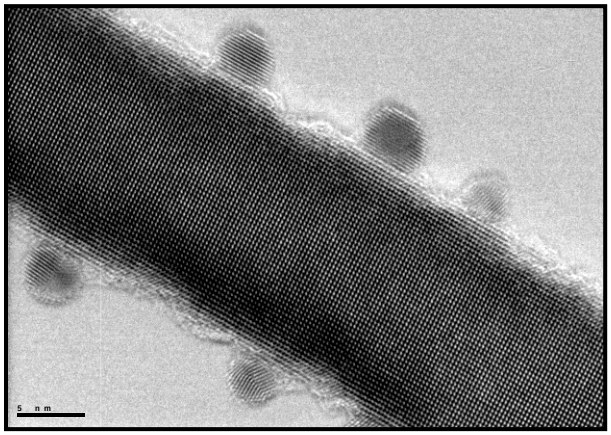

Figure 2.6: TEM image of Au nanoclusters supported on TiO_2 (110) planes

The above sample preparation method enables the analysis of surfaces and interfaces of nanoclusters for a wide range of nanocluster sizes. Figure 2.7 shows an example of an aberration corrected HRTEM and an aberration corrected STEM image of gold nanoclusters supported on TiO_2 (Au/TiO_2). The white lines on the STEM image are a guide to the eye showing how the particle dimensions, namely the center-to-edge (h) and center-to-interface (h-Δh) distances, can be typically extracted.

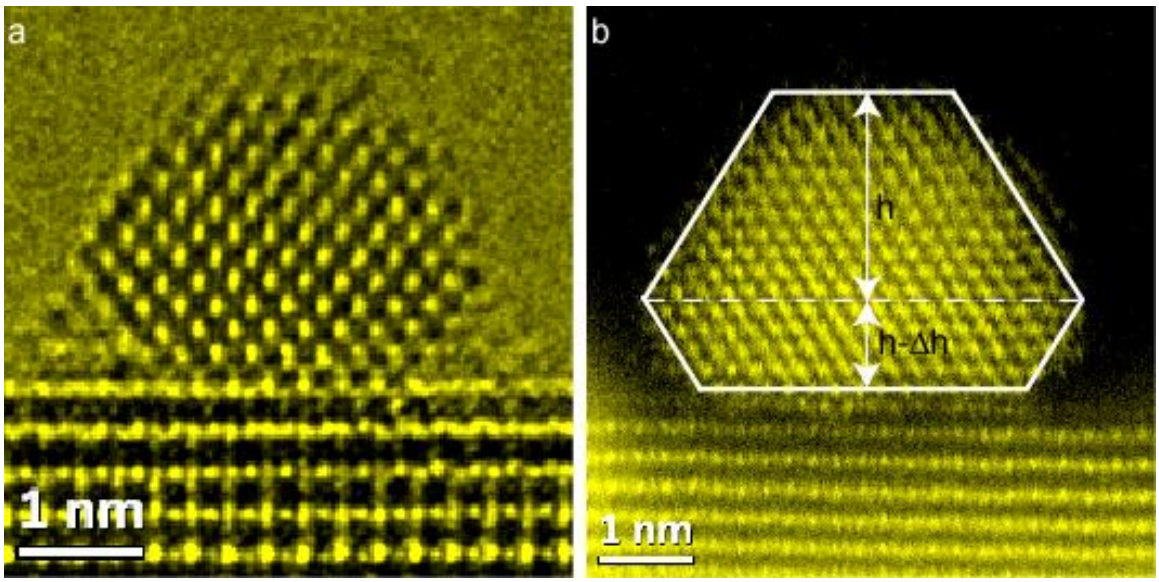

Figure 2.7: Aberration corrected (a) HRTEM and (b) HRSTEM images of Au/TiO_2. The white lines are a guide to the eye.

CHAPTER 3

EFFECT OF TITANIUM DIOXIDE SURFACE STOICHIOMETRY ON EPITAXY OF GOLD AND SILVER NANOCRYSTALS

The structural evolution and epitaxy of gold and silver nanoclusters (NCs) on TiO_2 (110) surfaces are reported here for oxidized (oxygen rich) and reduced TiO_2 surfaces. Additionally for silver, the sublimation temperature is also explored as a function of the surface stoichiometry. The reduced TiO_2 (110) surface was found to be (1x2) reconstructed after annealing the oxidized surface in vacuum to ~750^{o}C. It is shown that gold NCs evolve to the same epitaxial orientation – (111) Au || (110) TiO_2, [-110] Au || [001] TiO_2 irrespective of the details of the surface preparation and annealing conditions. In all the experiments, a (1x2) reconstruction is always observed along with the presence of Au epitaxy. For vacuum annealed samples, the onset and completion of epitaxy happens at much lower temperatures on the reduced (reconstructed) surface compared to a oxidized (unreconstructed) surface.

For silver, it is shown that silver NCs deposited at room temperature on oxidized TiO_2 (110) surfaces are unable to form a single epitaxy prior to sublimation. When heated close to sublimation - two particle orientations dominate - (111) Ag || (110) TiO_2, [-110] Ag || [001] TiO_2 ; (112)Ag || (110) TiO_2, [-110] Ag || [001] TiO_2. Single twinned silver NCs are found to be stable even at temperatures close to sublimation. On the other hand, silver NCs prepared similarly on reduced TiO_2 (110) surfaces behave very differently when heated to higher temperatures. On the reduced surface, the NCs are able to evolve into a single epitaxy - (111) Ag || (110) TiO_2, [-110] Ag || [001] TiO_2. The sublimation temperature for silver NCs on the reduced surface is found to be less than those on the oxidized surface by about 35 degrees. The

epitaxy formed by annealing is the same as the one formed by depositing silver onto reduced TiO_2 (110) at 350^oC (> 0.5 Tm of Ag).

3.1 Introduction

Single crystal titanium dioxide (TiO_2) is a model substrate for the study of oxide surfaces and growth of metal nanoparticles, which has been investigated extensively in the literature[49]. A major motivation of this study comes from the catalytic activities of metal nanoclusters (NCs) supported on TiO_2[49, 65], the importance of NC structure and the effect of TiO_2 surfaces on the NC structure. For example, gold NCs on TiO_2 have been shown to convert carbon monoxide to carbon dioxide at relatively low temperatures[29, 32, 87]. The properties of the TiO_2 surfaces also present unique opportunities for the study of surface and interfacial physics. For example, the chemistry and structure of TiO_2 surfaces can be very well controlled by different processing conditions[49]. The (110) surface of TiO_2 has the lowest surface energy [53] and has been a popular choice for experimental studies. Amongst various transition metals that have been studied on TiO_2 (110) surfaces[49, 57], gold, silver and copper are free of encapsulation at high temperatures on TiO_2 (110) surfaces [49], which makes them amenable to in-situ surface studies.

NCs on 2D oxide surfaces provide a model system to understand the effect of the support's surface on the size, shape and structure of metal NCs.[48] A number of experimental [41, 49, 63-65, 69, 70, 88-102] and theoretical investigations[42, 60-62, 68, 103, 104] have been conducted on Au NCs supported on TiO_2 (110) surfaces. As summarized in chapter one, it is known that at room temperature Au prefers to nucleate on oxygen vacancies. At coverages less than 0.1ML Au NCs grow as elongated islands along the TiO_2 [001] direction. [63-65] Au NCs align parallel to TiO_2 [001] since the spacing between Au atoms along the <110> close packing

direction ($d_{Au(110)}$ = 2.885 Å) lattice matches with TiO_2 (001) ($d_{TiO2(110)}$ = 2.954 Å). Increasing coverage leads to the formation of quasi-2D, hemispherical and eventually spherical 3D shaped islands when NC diameter is greater than 4nm. Annealing these NCs in vacuum leads to the formation of epitaxial Au islands with the epitaxial relationship[70] – $Au(111)_{[-110]} \parallel TiO_2(110)_{[001]}$. The same epitaxy was reported for Au NCs prepared on TiO_2 powders by precipitation and calcinations.[69] However, using DFT calculations, Lopez et. al. found that the work of adhesion for a defect-free $Au(111)/TiO_2(110)$ interface was nearly zero.[61, 68] Lopez et. al. further calculated the binding energy of a Au NC to be 1.6 eV/defect and argued that interfacial defects stabilize the $Au(111)/TiO_2(110)$ interface. Lopez et. al. did not offer an explanation for why the defects stabilize the epitaxial relationship found by Cosandey et. al. and others. It is conceivable that the changes to surface atomic structure of TiO_2 (110) during vacuum annealing could have resulted in surface atomic structures/ surface reconstructions that result in a preferred epitaxial relationship. We wanted to probe the formation of a preferred epitaxy in $Au/TiO_2(110)$ and identify the effect of surface stoichiometry and surface reconstruction on Au/TiO_2 (110) epitaxy to help us understand why Au (111) adheres to TiO_2 (110) even though DFT calculations suggest that the work of adhesion of such an interface is nearly zero.

Further, it would also be instructive to compare the similarities and differences in the formation of epitaxial islands between Au and Ag on TiO_2 (110). Au and Ag are both FCC solids with similar lattice parameters ($a_{0\text{-}Au}$ = 4.08 Å, $a_{0\text{-}Ag}$ = 4.09 Å) but prefer different nucleation sites on TiO_2 (110) because of their markedly different chemical properties.[59] While small Au NCs preferentially nucleate on surface defects such as oxygen vacancies,[62] small Ag NCs nucleate on step edge of TiO_2 (110).[105, 106] Also, while the binding energy of $Au\text{-}O_{br\text{-}v}$ is

lower than Au-O_{br} the binding energy of Ag-$O_{br\text{-}v}$ is more than Ag-O_{br}.[59] Hence it is expected that the effect of surface stoichiometry of TiO_2 (110) on Au and Ag will be quite different. Moreover, compared to Au that prefers nanocrystal formation,[63] Ag can form a number of intermediate structures, including multiply twinned particles (MTPs).[107-109] While the growth characteristics of Ag on TiO_2 (110) surfaces have been studied by several groups [94, 105, 110], there is no systematic study of the structure evolution and epitaxy formation of Ag NCs on TiO_2 (110). Temperature dependent studies are important, in general, for understanding the effect of sintering on the structure of NCs.[99, 111] Hence we investigated the effect of surface structure and stoichiometry on the epitaxy of Au and Ag on TiO_2 (110). In the case of Ag, we also investigated the effect of surface stoichiometry on the sublimation temperature of Ag NCs.

We used RHEED to investigate the structure and epitaxy of Au and Ag NCs on TiO_2 (110). We show that RHEED offers a reliable way to obtain real time, in-situ, structural data from an ensemble of NCs during heating.[112, 113] We studied the structural evolution of Au and Ag NCs on TiO_2 (110) as a function of temperature up to the formation of epitaxy for Au and up to sublimation for Ag. The results from these experiments show the surface stoichiometry of TiO_2 (110) is critical for the evolution and sublimation of Au and Ag NCs. Information about Au and Ag NCs' structural evolution at high temperatures can be useful, for example in catalytically relevant systems.[5, 6, 114-116]

3.2 Experimental Methods

For Au and Ag, slightly different specimen preparation methods were used since Au NCs were imaged using AFM while Ag NCs were imaged using TEM. For both Au and Ag we started

with epi-polished TiO_2 (110) substrates obtained from MTI Corporation. The as-received TiO2 (110) substrates were heated in air for 2 hours at 1100^oC. Such substrates will henceforth be referred to as "furnace oxidized" TiO_2 (110). The furnace oxidized TiO_2 showed predominantly a (1x1) surface (Figure 3.1). There is some weak intensity observable in the RHEED patterns taken along the TiO_2 [001] zone axis (Figure 3.1 (b)) between the strong (1x1) spots which suggest that other atomic arrangements exist on the surface in agreement with earlier studies.[117] We also observe little streaking of the RHEED spots, which implies that the terrace width on our surfaces are quite large. All the specimens in this work exhibited charging and beam deflection when the specimen was transferred from air. The contamination was removed by heating to ~200^oC in vacuum for ~ 10 minutes.

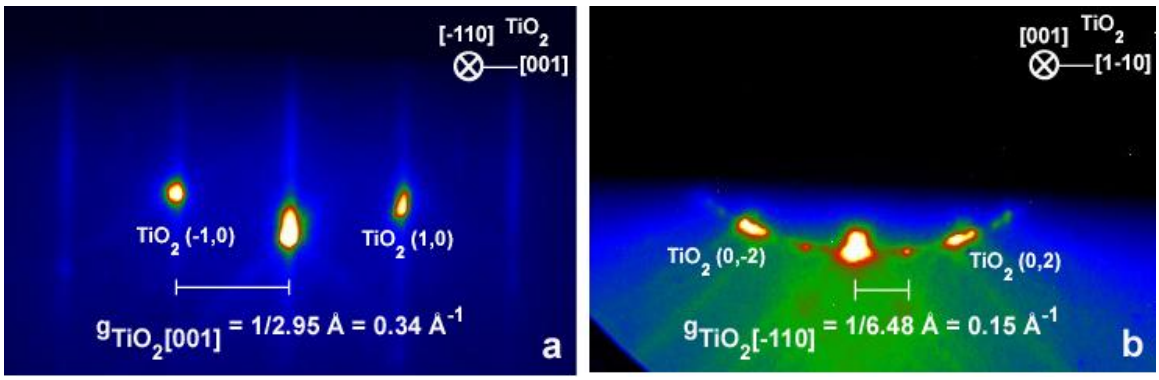

Figure 3.1: RHEED patterns of furnace oxidized TiO_2 (110) taken close to (a) TiO_2 [-110] and (b) TiO_2 [001] zone axes respectively. The diffraction patterns were obtained at the same magnification.

Au NCs were deposited by sputtering at a rate of ~0.2Å/s in a AJA International Co-Sputtering Unit (Microfab, CMM). The deposition rate was read from a quartz crystal monitor. The rate was measured by setting the density of Au to 1/10th of the actually density of Au (19.3 g/cc). It was found using AFM that the actual deposition rate was higher than the value read out on the thickness monitor. A 1Å deposition on the quartz crystal thickness monitor was found to

correspond to roughly 4.8Å of Au deposition using AFM as a calibration tool (without taking into account particle size broadening due to AFM tip). Post deposition, the samples were transferred to a high vacuum chamber (base pressure < $3x10^{-8}$ torr) or an air furnace for annealing. RHEED was performed using a 15 keV electron beam using a STAIB RHEED gun (http://www.staibinstruments.com). The substrate was placed on a rotation stage, permitting diffraction measurements from different azimuthal angles. RHEED patterns were recorded using a combination of a phosphor screen and an optically coupled CCD camera. For annealing in vacuum, the substrate was heated by radiation from a resistive heater that is located ~ 15 mm from the stage. For annealing in air, the substrate was heated in a three zone lindberg tube furnace (http://www.lindbergmph.com) in an alumina boat obtained from Coorstek.

For Ag, the as-received wafer was coated with 300nm of SiO_2 via PECVD to prevent any damage to the surface during the sample preparation processes. SiO_2 was chosen since it could be removed fully using HF, without affecting the TiO_2 surface below. The wafer was heated to 300^oC during PECVD. The wafer was then cut into pieces of ~8mm x 2mm in dimension using a diamond saw. The cut specimens were back thinned by dimpling to obtain a thin region of 10-20μm thickness, which was later ion-milled on the back side using 5keV Argon ions in a Gatan Precision Ion Miller to create electron transparent regions. The SiO_2 protective layer was later removed by etching using 49% HF – thereby maintaining a clean TiO_2 (110) surface, that was verified using RHEED. In a separate control experiment it was seen that 49% HF did not etch TiO_2 (110) even after 48 hours.

In the case of ion milled samples, the oxygen vacancies created during ion-milling (which is evident from the color change of the sample) were removed by annealing the sample at 1450^oK [118] for 2 hours in air. Regrowth features are expected to be seen on such surfaces,

similar to the regrowth features seen during high temperature oxygen exposure in vacuum [119]. The regrowth features on the surface were removed by etching the sample in boiling sulfuric acid for 2 minutes. Such specimens showed a (1x1) RHEED pattern after heating to 150^{o}C inside a vacuum chamber.

Specimens that were reduced in vacuum can be reused by the above method of air furnace oxidation, etching in H_2SO_4 and heating to 150^{o}C inside a vacuum chamber. It was seen that the RHEED pattern had no streaks for the as-received specimens indicating a flat surface. The surface flatness was also checked in an AFM. However, the RHEED pattern shows streaks after the samples were reduced in vacuum and were reoxidized; this is expected from a more disordered terrace structure after the reduction-oxidation process. However, no significant difference was observed between using the reoxidized specimen as against the as-received specimen. We will henceforth refer to the reoxidized surface also as 'furnace-oxidized' along the lines of furnace oxidized TiO_2 specimens prepared for Au.

Ag was deposited onto the substrate from a MDC "e-Vap® Mighty Source™"– a 4 pocket (2cc capacity) rotary e-beam evaporator in a vacuum chamber with a base pressure of $2x10^{-7}$ torr during evaporation and a base pressure of $5x10^{-8}$ torr during specimen heating. The amount of Ag deposited was monitored using a quartz crystal monitor. Reflection High Energy Electron Diffraction (RHEED) was performed using a 13 keV electron beam using a FOCUS RHEED gun from Focus-gmbh. The geometry of the substrate, heater and screen are the same as described earlier for Au.

For Transmission Electron Microscopy (TEM) measurements, the sample was transferred in air before being loaded onto the TEM stage using a custom-made holder that could hold a

8mm x 2mm TiO_2 specimen and simultaneously fit into any JEOL single tilt TEM holder. TEM micrographs were obtained from JEOL 2010 LaB_6 and JEOL 2010F, both operating at 200 keV.

3.3 Results

3.3.1 Studies of Gold NCs onTiO_2 (110)

3.3.1.1 Gold NCs deposited on furnace oxidized TiO_2 (110) and vacuum annealed

Figure 3.2(a) shows a RHEED pattern of 1 Å Au deposited on furnace oxidized TiO_2(110) at 215^{o}C. The azimuth of TiO_2 could not be determined since the diffraction from TiO_2 was weak due to shadowing by Au NCs. The samples were heated at the rate of 5^{o}C/s. The series of RHEED patterns in Figure 3.2 (a), (b) and (c) show the evolution of the Au NCs with temperature. At 215^{o}C, the random arrangement of Au NCs gave rise to broad diffraction rings in the RHEED pattern of the as-deposited Au (Figure 3.2 (a)). On heating, epitaxial NCs began to form and showed up in the RHEED pattern as strong diffraction spots. Figure 3.2 (b) shows the diffraction pattern recorded at ~500^{o}C. It is seen that the epitaxy is still very weak and not discernable to the eye at 500^{o}C. Figure 3.2 (c) shows the diffraction pattern at ~785^{o}C. At 785^{o}C, the epitaxy is clearly identifiable. Upon the formation of epitaxial Au NCs, the diffraction spots from TiO_2 also became strong and allowed us to obtain diffraction patterns from the surface along low index TiO_2 zone axes. Figure 3.2 (d) and (e) show RHEED patterns from TiO_2 [1-10] and TiO_2 [001] azimuths respectively. On indexing the RHEED patterns in Figure 3.2 (d) and (e), it was seen that epitaxy could be described as –

$$(111)\ Au \parallel (110)\ TiO_2,\ [-110]\ Au \parallel [001]\ TiO_2$$

In such NCs, both ABCABC and ACBACB (energetically equivalent) stacking are observed in the RHEED pattern. For both kinds of NCs, the electron beam is parallel to Au [-110]. This epitaxial orientation relationship is consistent with Cosandey et. al.'s experiments for room temperature deposition of Au on TiO_2 (110) followed by vacuum annealing.[70] The AFM image in Figure 3.3 shows that the Au NCs are mostly smaller than 20 nm and dense (coverage ~0.2) following vacuum annealing to 750^{o}C.

The black arrows in Figure 3.2 (e) point to the appearance of TiO_2 diffraction peaks corresponding to a spacing of 12.96 Å, i.e. two times the periodicity of TiO_2 (1-10) ($d_{TiO2(1\text{-}10)}$ = 6.48 Å). At the same time, no new TiO_2 diffraction peaks was observed in Figure 3.2 (d), which is a RHEED pattern along an orthogonal azimuth (TiO_2[-110]). Thus the reconstruction can be described as TiO_2 (110) (1x2). The (1x2) reconstruction was not observed in the furnace oxidized TiO_2 (110) prior to vacuum annealing (Figure 3.1). Hence, vacuum annealing was responsible for the appearance of the (1x2) reconstruction. Multiple stable (1x2) reconstructions have been observed on the TiO_2 (110) surface subject to different surface treatments in vacuum.[54-56, 120] We cannot identify the type of (1x2) reconstruction present in our samples post vacuum annealing from just RHEED patterns; identification of atomic co-ordinates from diffraction patterns require a more quantitative understanding of diffraction patterns. One of the possible reconstructions is the 'added-row' model proposed by Pang et. al. where the surface has no bridging oxygen atoms and every second Ti-row along TiO_2[001] is missing.[54] The periodic arrangement of the surface atoms in this reconstruction has been shown in Figure 3.4.

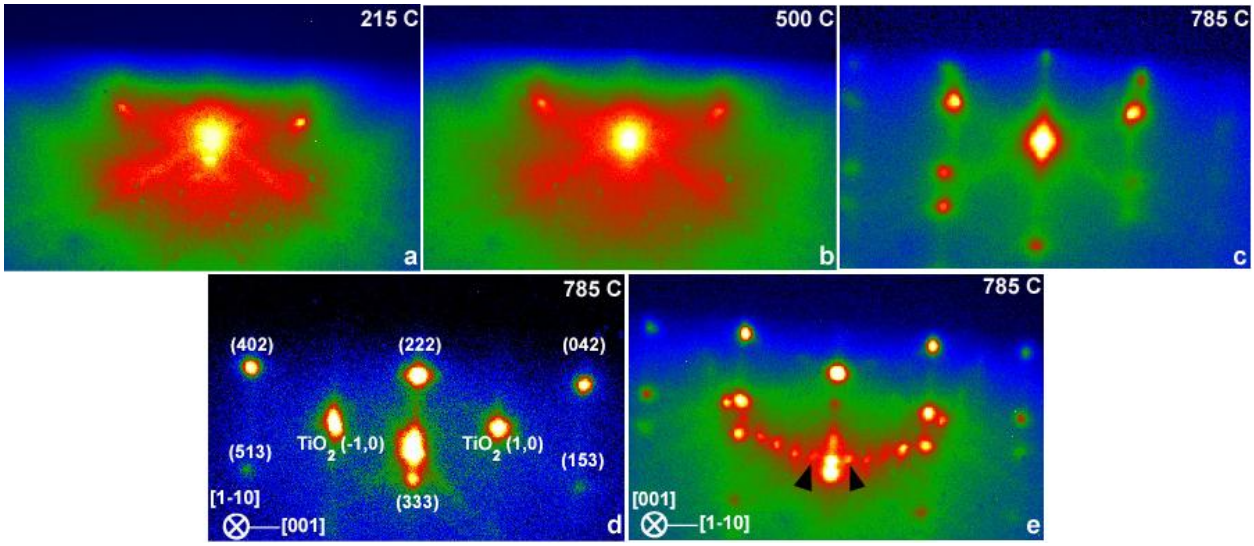

Figure 3.2: RHEED patterns of 1Å Au deposited on furnace oxidized TiO_2 (110) at 25°C annealed to (a) 215°C, (b) 500°C, (c) 785°C, (d) and (e) 785°C in vacuum taken close to TiO_2 [1-10] and TiO_2 [001] zone axes respectively. The arrows in (e) point to spots arising from (1x2) TiO_2 reconstruction. All directions on the figures are specified with respect to bulk rutile TiO_2 lattice. The directions in the bottom left corners of the figures are specified with respect to bulk rutile TiO_2 lattice. All diffraction patterns were obtained at the same magnification.

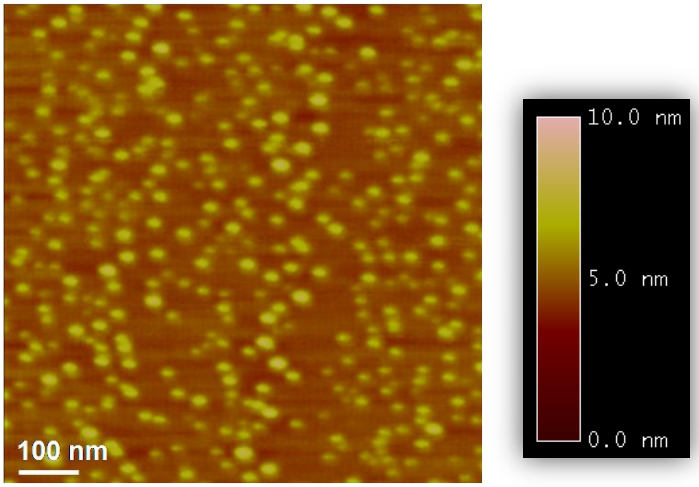

Figure 3.3: AFM image of 1Å Au deposited on a furnace oxidized TiO_2(110), and heated to 750°C in vacuum.

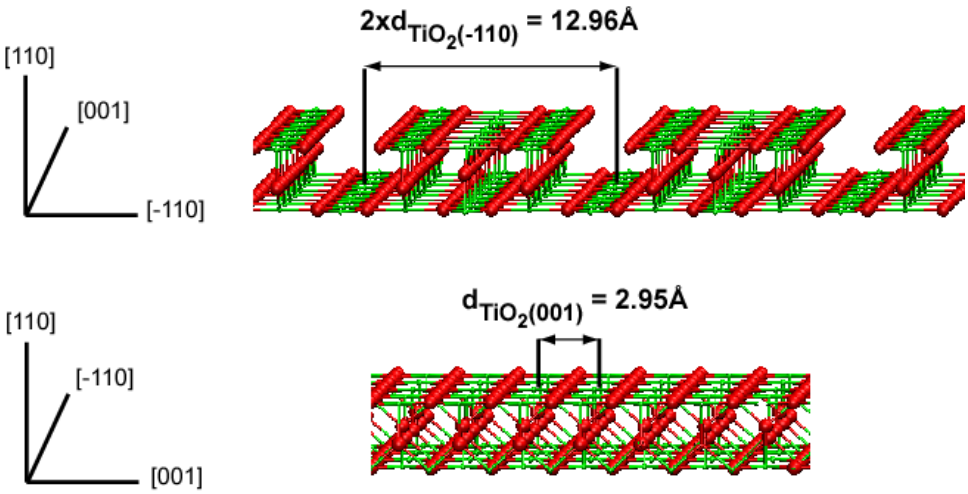

Figure 3.4: Schematic of the top row of Pang et al.'s TiO_2 (110) (1x2) reconstruction showing the unit cell on the reconstructed surface.

3.3.1.2 Gold NCs deposited on reduced TiO_2 (110) and vacuum annealed

A reduced surface of TiO_2 (110) was prepared by heating a furnace oxidized TiO_2 (110) to 750^{o}C in vacuum. Figure 3.5 (a) shows a RHEED pattern of the reduced TiO_2 (110) surface along the TiO_2 [001] azimuthal direction. The black arrows in Figure 3.5 (a) point to the appearance of TiO_2 diffraction peaks corresponding to a spacing of 12.96 Å. The RHEED pattern along the orthogonal azimuth – TiO_2[-110] – was similar to the RHEED pattern from furnace oxidized TiO_2 (110) (Figure 3.1) and hence is not shown. Hence, the surface of reduced TiO_2 is (1x2) reconstructed similar to the vacuum annealed TiO_2 (110) in the previous section. Thus, subsequent reference to reduced TiO_2 (110) implicitly means that the surface is also (1x2) reconstructed.

The samples were heated at the rate of 5^{o}C/s. The series of RHEED patterns in Figure 3.5 (b), (c) and (d) show the evolution of the Au NCs with temperature. The RHEED patterns in Figure 3.5 (b), (c) and (d) were obtained along the TiO_2 [1-10] azimuth. In contrast to Au NCs

on furnace oxidized TiO_2 (110) where there was little sign of epitaxy at 215^oC (Figure 3.2(a)), Au NCs deposited on reduced TiO_2 (110) show a stronger sign of epitaxy at 215^oC, which is clear from the appearance of a discernable Au diffraction peak (indicated by white arrow Figure 3.5 (b)). In the diffraction pattern at 500^oC (Figure 3.5 (c)), it is seen that the epitaxy becomes more prevalent and the peak identified by the white arrow becomes stronger (Figure 3.5 (c)). The visible appearance of a strong Au peak is again in contrast with Au deposited on furnace oxidized TiO_2 (110) where the epitaxy was weak and not discernable to the eye at 500^oC (Figure 3.2 (b)). Figure 3.5 (d) shows the diffraction pattern at 760^oC. At 760^oC, the epitaxy is clearly identifiable. On indexing the RHEED patterns in Figure 3.5 (d), it was seen that the epitaxy could be described as –

$$(111)\ Au \parallel (110)\ TiO_2,\ [-110]\ Au \parallel [001]\ TiO_2$$

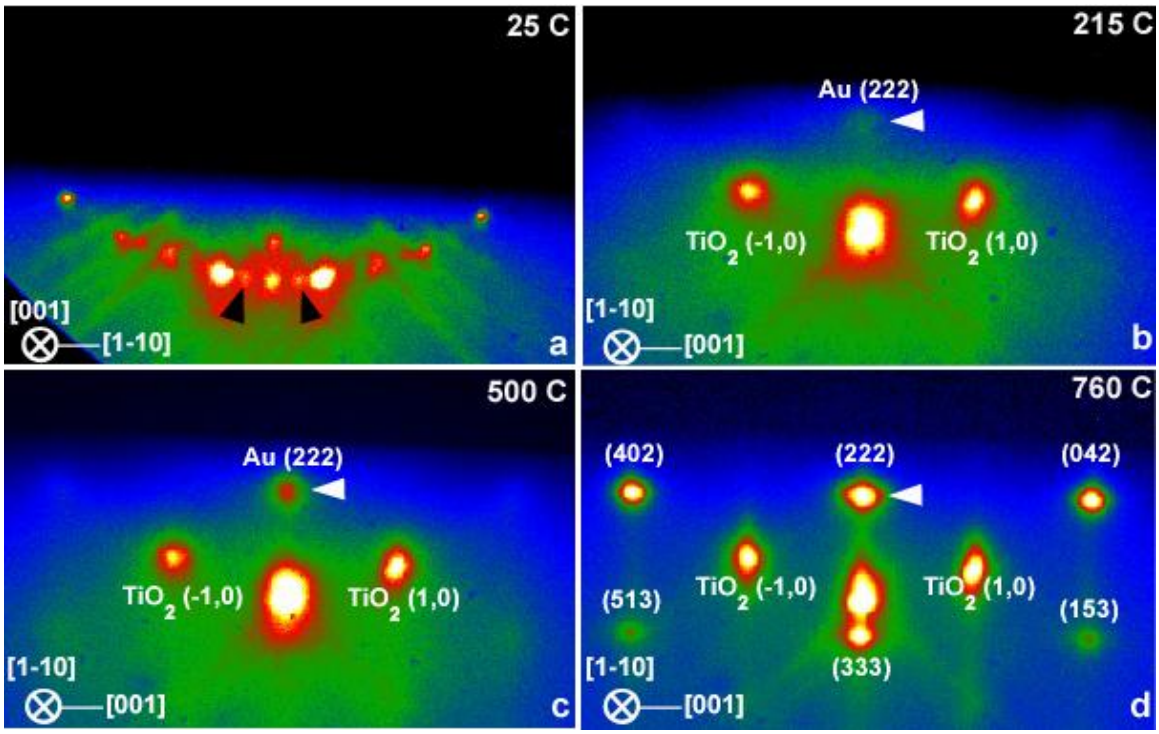

Figure 3.5: (a) RHEED pattern of reduced TiO_2 (110) taken close to TiO_2 [001] zone axis. The black arrows point to diffraction peaks from TiO_2 (110) (1x2) reconstruction. (b), (c), (d) RHEED patterns (close to TiO_2 [1-10] zone axis) of 1Å Au deposited on reduced TiO_2(110) at 25^{o}C annealed to 215^{o}C, 500^{o}C and 760^{o}C respectively in vacuum. The white arrows in (b), (c) point to Au(222) diffraction peak. The directions in the bottom left corners of the figures are specified with respect to bulk rutile TiO_2 lattice. All diffraction patterns were obtained at the same magnification.

While the epitaxial relationship of 1 Å Au on reduced TiO_2 (110) is similar to the epitaxy of 1 Å Au on furnace oxidized TiO_2 (110) at high temperatures, the onset and completion of epitaxy appear to happen at much lower temperatures on a reduced (and reconstructed) TiO_2 (110) substrate. In order to probe the temperature dependence of Au NC epitaxy more quantitatively, we plotted the integrated intensity of a Au diffraction peak as a function of temperature in Figure 3.6. Figure 3.6 (a) and Figure 3.6 (b) show the evolution of a selected Au diffraction (Bragg) peak for Au NCs deposited on furnace oxidized TiO_2 (110) and reduced TiO_2 (110) respectively. The dashed lines point to temperatures where the intensity was seen to change abruptly signifying the onset and completion of epitaxy. The onset of epitaxy is inferred

from the abrupt rise in intensity of the Au Bragg peak since epitaxial rearrangement leads to an increased number of Au atoms scattering into the same direction. It is seen that the onset of epitaxy happens at ~750^{o}C for Au NCs on furnace oxidized TiO_2 (110) while the onset happens at ~600^{o}C for Au NCs on reduced TiO_2 (110). The completion of epitaxy is inferred from the abrupt drop in intensity of the Au Bragg peak since at the completion of epitaxy, the fall in diffraction intensity due to increased atomic vibration at higher temperatures (described by the Debye-Waller factor) takes over. (The abruptness in the drop suggests that the epitaxial transformation is highly temperature sensitive and completes in a small temperature range where the TiO_2 surface is probably reconstructing and aiding the epitaxial transformation of Au.) It is seen that the completion of epitaxy happens at ~780^{o}C for Au NCs on furnace oxidized TiO_2 (110) while the completion happens at ~700^{o}C for Au NCs on reduced TiO_2 (110).

Thus the onset and completion of epitaxy of Au NCs on (1x2) reconstructed TiO_2 (110) happen at 150 degrees and 80 degrees lower than the onset and completion on unreconstructed furnace oxidized TiO_2 (110) respectively. The significantly lower epitaxial onset and completion temperatures can be attributed to the nucleation of epitaxial NCs even at lower temperatures (215^{o}C) on reduced TiO_2 (110) surfaces as against randomly nucleated Au NCs on furnace oxidized TiO_2 (110) surfaces at lower temperature. This is also supported by the AFM image in Figure 3.7 which shows that the coverage (~0.3) for Au NCs deposited on reduced and reconstructed TiO_2(110) is greater than the coverage of Au NCs deposited on furnace oxidized TiO_2 (110) (~0.2 in Figure 3.3). However, since the effect of tip-shape can influence the details of coverage for smaller NCs, we don't rely too much on the AFM data at these NC sizes.

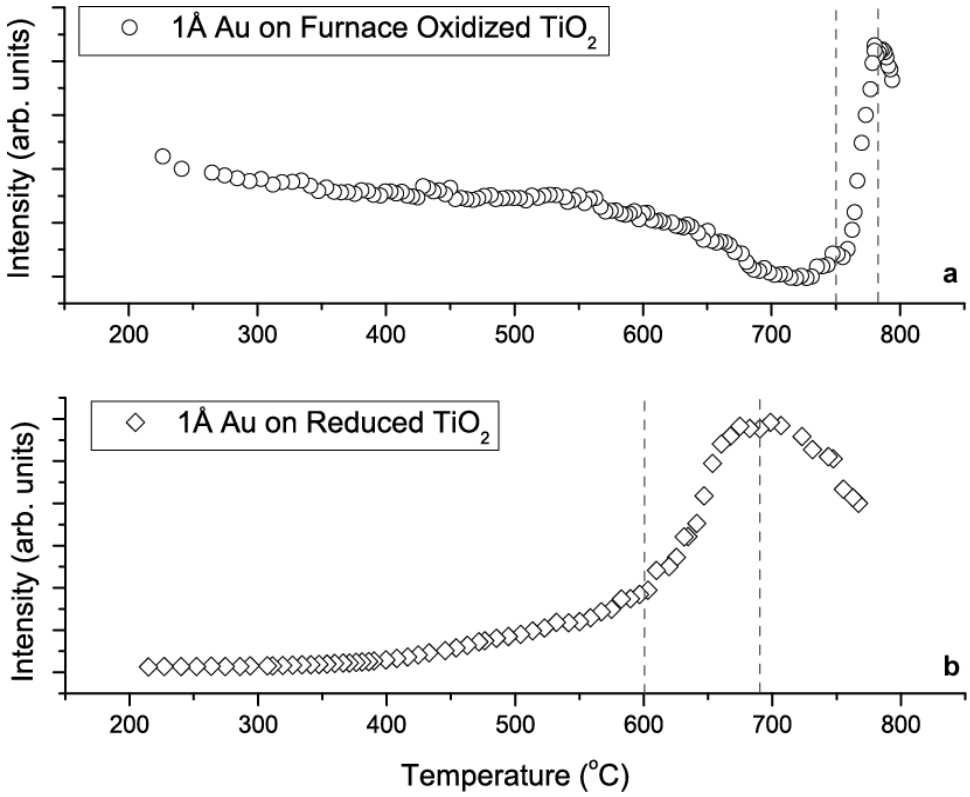

Figure 3.6: RHEED intensity versus temperature for gold nanoclusters deposited at 25°C on (a) furnace oxidized TiO_2(110) and (b) reduced TiO_2(110) with (1x2) reconstruction. The RHEED intensities were obtained from Au (224) and Au (222) diffraction spots respectively. The dashed lines show the onset of dramatic increase in the intensity.

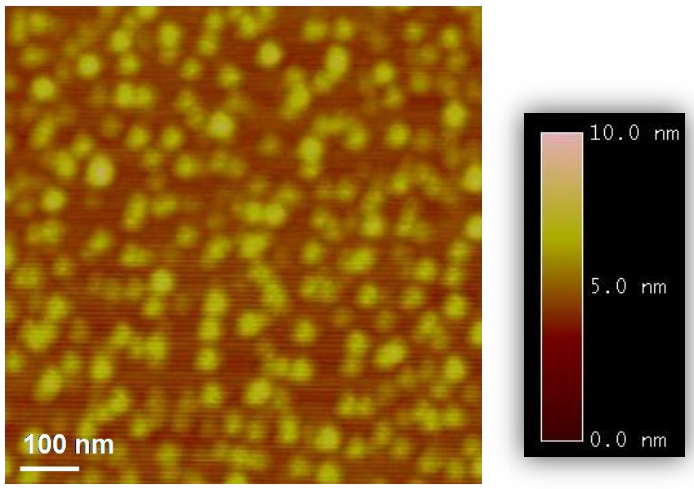

Figure 3.7: An AFM image of 1Å Au deposited on a reduced TiO_2(110) with (1x2) reconstruction, and heated to 750^{o}C in vacuum.

3.3.1.3 Gold NCs deposited on furnace oxidized TiO_2 (110) and air annealed

Au NCs deposited at room temperature on a furnace oxidized surface of TiO_2 (110) were heated to 750^{o}C in an air furnace for 1 hour. Figure 3.8 (a) and (b) shows the diffraction patterns after the Au NCs were heated to 750^{o}C along the TiO_2 [-110] and TiO_2 [001] azimuths respectively. On indexing the RHEED patterns in Figure 3.8 (a), it was seen that the epitaxy could be described as –

$$(111)\ Au \parallel (110)\ TiO_2,\ \ [-110]\ Au \parallel [001]\ TiO_2$$

which is identical to the epitaxy reported in the previous sections. Figure 3.8 (c) is a magnified view of the red box in Figure 3.8 (b). The black arrows in Figure 3.8 (c) point to the TiO_2 (1x2) diffraction peaks. The other peaks close to the (1x1) peaks probably stem from different types of oxygen induced surface restructuring phenomena that appear during air annealing of TiO_2 (110).[117] It is interesting to see that in all the above cases, some form of (1x2) TiO_2 (110) reconstruction is seen along with the occurrence of the $Au(111)_{[-110]}\|TiO_2(110)_{[001]}$ epitaxy. Even

though the epitaxial relationship is similar to Au NCs annealed in vacuum, we found that the density (coverage = ~0.15) of Au NCs on air annealed specimens was much lower than the previous cases (Figure 3.9).

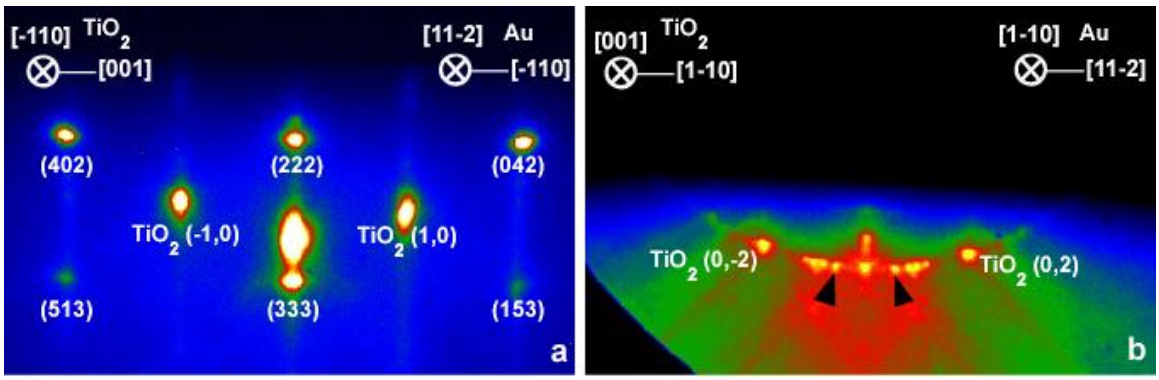

Figure 3.8: (a) RHEED pattern (close to TiO_2 [001] zone axis) of 1Å Au deposited on furnace oxidized TiO_2 (110) at 25^{o}C annealed to 750^{o}C in air. (b) RHEED pattern (close to TiO_2 [1-10] zone axis) of 1Å Au on furnace oxidized TiO_2 (110) annealed to 750^{o}C in air. (c) Magnified view of box in (b). The arrows in (c) point to spots arising from (1x2) TiO_2 reconstruction. The diffraction patterns were obtained at the same magnification.

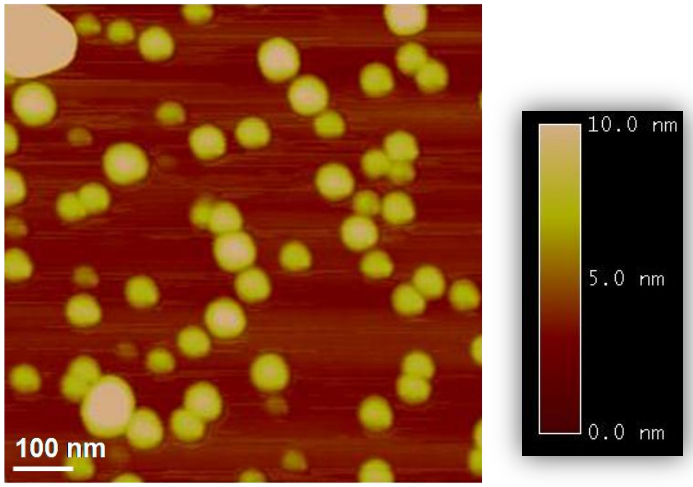

Figure 3.9: AFM image of 1Å Au deposited on a furnace oxidized TiO_2(110), and heated to 750^{o}C in air.

3.3.2 Studies of Silver NCs on TiO_2 (110)

3.3.2.1 Silver NCs deposited at room temperature on furnace oxidized TiO_2 (110)

A. Structure Evolution and Epitaxy

Figure 3.10 (a) shows a RHEED pattern of furnace oxidized TiO_2(110) along the [001] azimuth of TiO_2. There are no obvious diffraction spots from surface reconstructions and the surface structure appears (1x1) terminated. A coverage of 6.5 Å of Ag was deposited onto furnace oxidized TiO_2 (110) at room temperature (~25^oC). The samples were heated at the rate of 5^oC/s. The series of RHEED patterns in Figure 3.10 (b), 1(d) and 1(e) show the evolution of the Ag NCs with temperature. All RHEED patterns in Figure 3.10 were obtained along the [001] azimuth of TiO_2 (110). Figure 3.10 (c) shows a TEM micrograph of 6.5 Å of Ag deposited on fully oxidized TiO_2 (110) at room temperature. It can be seen from Figure 3.10 (c) that, as deposited there are multiple orientations of NCs, as well as single twinned and multiply twinned NCs. This random arrangement of Ag NCs gave rise to broad diffraction rings in the RHEED pattern of the as deposited Ag (Figure 3.10 (b)). On heating, different textures – each with its own epitaxial relationship – began to appear on the RHEED pattern. Figure 3.10 (d) shows the diffraction pattern at ~460^oC. Figure 3.10 (e) shows the diffraction pattern at ~585^oC. Figure 3.10 (g) shows a schematic of the diffraction pattern in Figure 3.10 (e) along with indices of the Ag diffraction rings. TiO_2 spots are not shown in the schematic for the sake of clarity. On indexing the RHEED diffraction pattern, it is seen that two epitaxial relationships dominate. They can be described by –

$$(111)\ Ag \parallel (110)\ TiO_2,\ [-110]\ Ag \parallel [001]\ TiO_2$$

(112) Ag || (110) TiO_2, [-110] Ag || [001] TiO_2

In such NCs, both ABCABC and ACBACB (energetically equivalent) stacking are observed in the RHEED pattern. This has been previously observed for FCC metals on other ceramic substrates as well [70]. This is shown schematically in Figure 3.10 (g) by diametrically opposite shading on diffraction spots belonging to different stacking sequences but similar epitaxial orientations. The spots corresponding to Ag (111) have been shaded horizontally while the spots corresponding to Ag (112) have been shaded vertically. When spots from two different stacking sequences overlap, it is shown as a filled dark circle. For both kinds of NCs, the electron beam is parallel to Ag [-110]. The lack of single epitaxy is most likely from the nucleation and growth of NCs around different kinds of surface defects. As shown in previous work [119] TiO_2(110) heated in the presence of oxygen results in a multitude of surface regrowth/reconstructions. These surface reconstructions, which are small enough to be not detected by RHEED (Figure 3.10 (a)), most likely act as pinning sites for the growth of epitaxial NCs.

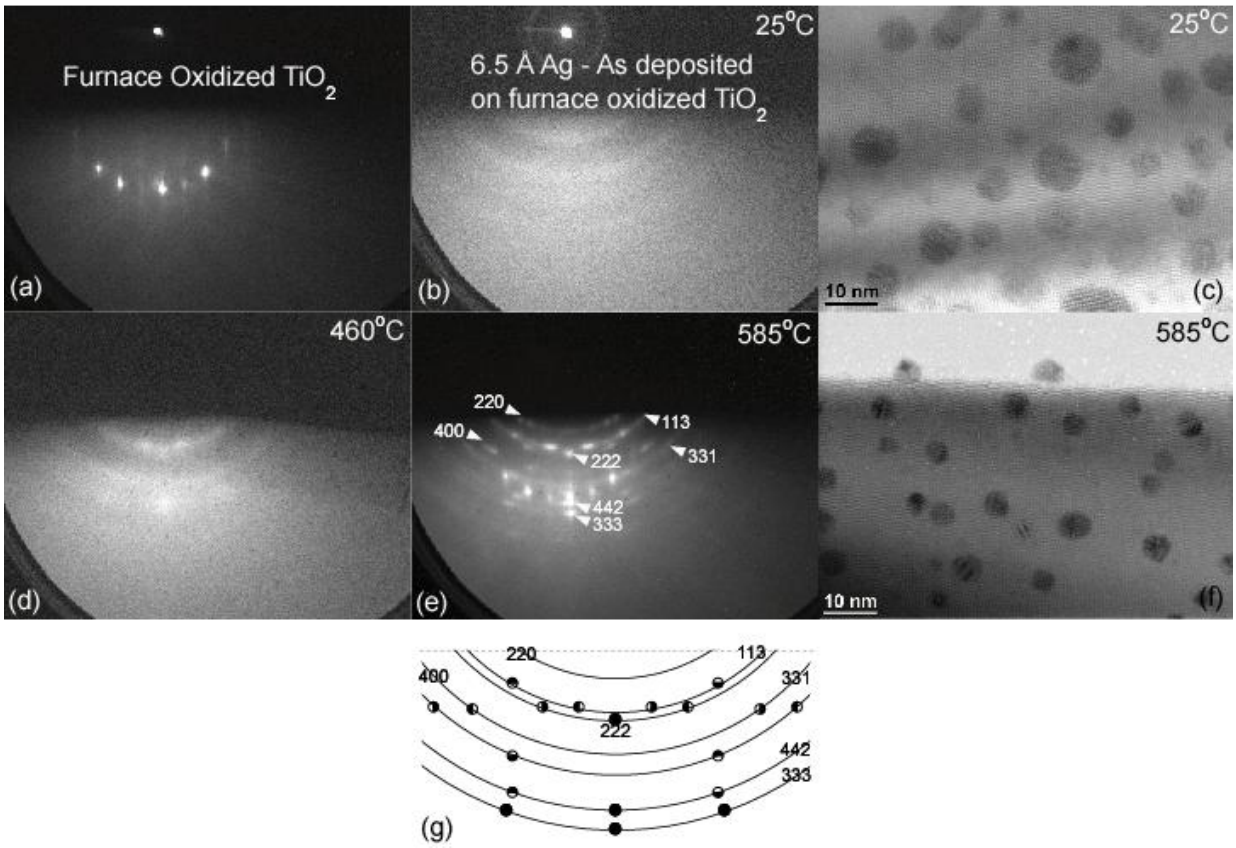

Figure 3.10: All RHEED patterns were obtained close to TiO_2[001]. (a) RHEED pattern of furnace oxidized TiO_2(110), (b) RHEED pattern and (c) TEM micrograph of Ag NCs on furnace oxidized TiO_2(110) at 25°C showing multiple NC orientations, (d) RHEED pattern of Ag NCs on furnace oxidized TiO_2(110) at 460°C showing the appearance of weak Ag diffraction spots, (e) RHEED pattern of Ag NCs on furnace oxidized TiO_2(110) at 585°C showing multiple epitaxies just prior to sublimation, (f) TEM micrograph at 585°C showing the presence of many singly twinned NCs prior to sublimation, (g) Schematic of RHEED pattern at 585°C – spots corresponding to Ag (111) have been shaded horizontally while the spots corresponding to Ag (112) have been shaded vertically. When spots from two different stacking sequences overlap, it is shown as a filled dark circle. The electron beam is parallel to Ag [-110] for both kinds of nanoclusters.

B. Sublimation

The RHEED intensities of the Ag (222) spot, TiO_2 (2,0) and the specular spot are shown in Figure 3.11 as a function of temperature. The increase of the Ag (222) intensity starts at ~ 450°C and continues until ~580°C. At the same time, the intensities of the TiO_2 (2,0) and

specular change only marginally. At 580^{o}C (shown by dashed line in plot), the Ag (222) intensity begins to decrease while the TiO_2 (2,0) and specular intensities increase dramatically. The intensities of the specular and the TiO_2 (2,0) mimic each other which suggests that the Ag desorbs significantly starting at 580^{o}C. The decrease in Ag coverage results in a larger surface region being exposed, which resulted in both the TiO_2 (2,0) and the specular intensity increasing. The decrease in Ag coverage is also seen by comparing Figure 3.10 (c) and Figure 3.10 (f). The Ag (222) intensity decreases till 620^{o}C (shown in dashed line in the plot), after which it stabilizes to more or less the background value. At this point no evidence of Ag is observed in the RHEED pattern. The dramatic decrease of the Ag diffraction spots beyond 620^{o}C is taken as the completion Ag NC sublimation. It must be noted that smaller NCs are expected to sublime at a lower temperature which cannot be detected here since the diffraction intensity is dominated by the signal from larger NCs. Melting of the Ag NCs is not completely ruled out, but since no amorphous rings were seen in the RHEED pattern, the silver disappearance event will be termed as sublimation henceforth.

At 585^{o}C, just prior to sublimation (Figure 3.10 (f)) singly twinned NCs dominate with a few epitaxial NCs also being present. Twinning is expected because the two predominant types of Ag NCs – (112) and (111) – have two orientations that are rotated 180^{o} about the TiO_2 (110) axis. Epitaxy is inferred from the presence of moiré fringes. Twinning is inferred from the presence of two sets of moiré fringes on the same island. It is clearly seen that twinned Ag NPs are stable all the way until sublimation and do not convert to single domain epitaxial islands in the timescales of our experiment.

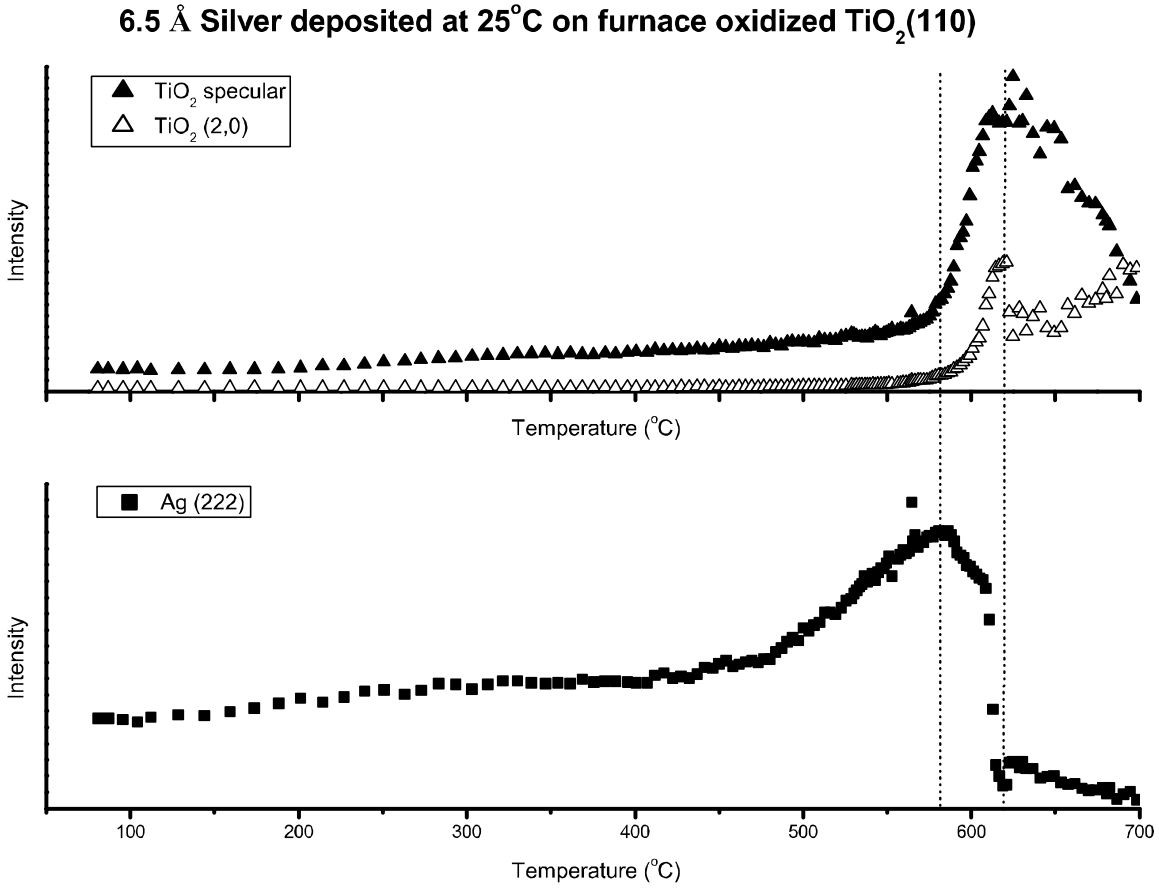

Figure 3.11: RHEED intensity versus temperature for silver nanoclusters deposited at 25°C on furnace oxidized TiO_2(110). The dashed line to the left shows the onset of sublimation and the dashed line to the right shows the completion of sublimation.

3.3.3 Silver NCs Deposited at Room Temperature on Reduced TiO_2 (110)

A. Structure evolution and epitaxy

A reduced TiO_2 (110) was prepared by starting with a furnace oxidized substrate (see the experimental section) and heating it to 750°C in vacuum. The substrate was then cooled to room temperature and 6.5 Å of Ag was deposited on it. The samples were then heated at the rate of 5°C/s. The series of RHEED patterns in Figure 3.12 (a)-(c) show the evolution of the Ag NCs with temperature. All RHEED patterns in Figure 3.12 were obtained along the [-110] azimuth of TiO_2 (110). The random arrangement of Ag NCs in the as deposited state gave rise to broad

diffraction rings in the RHEED pattern at low temperatures. Figure 3.12 (a) shows a diffraction pattern at ~100^{o}C that is dominated by the rings with a couple of weak spots. On further heating, a single epitaxial orientation began to appear on the RHEED pattern. Figure 3.12 (b) shows the diffraction pattern at ~350^{o}C where the Ag diffraction spots have been indexed. Figure 3.12 (c) shows the diffraction pattern at ~560^{o}C (that is after the start of sublimation) where the Ag spots have become weaker. It is seen from the RHEED pattern in Figure 3.12 (b) that the electron beam is parallel to Ag [11-2] and that there is only one epitaxy namely –

$$(111)\ Ag \parallel (110)\ TiO_2,\ \ [-110]\ Ag \parallel [001]\ TiO_2$$

In such NCs, both ABCABC and ACBACB (energetically equivalent) stacking were observed by recording RHEED patterns along the [001] azimuth of TiO_2 (not shown here).

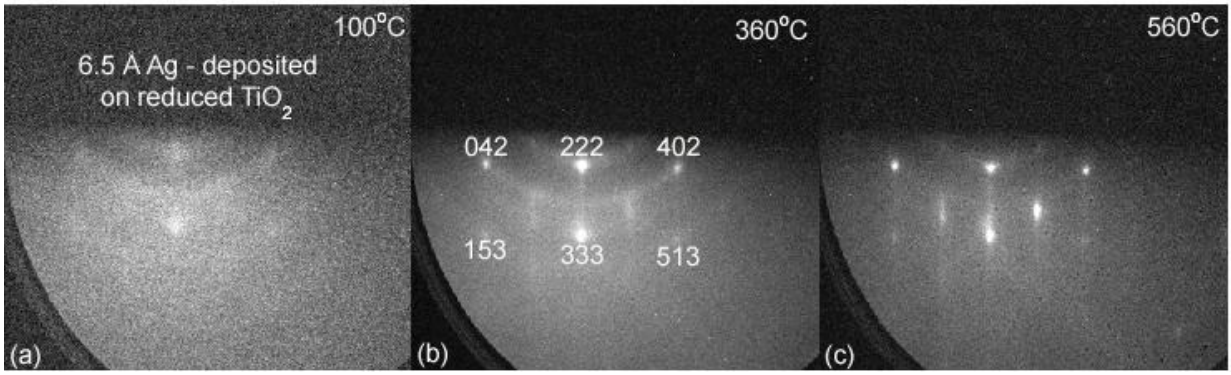

Figure 3.12: Silver nanoclusters on reduced TiO_2(110) : RHEED pattern taken along [-110] TiO_2 at (a) 100^{o}C showing the onset of epitaxy and weak Ag diffraction spots, (b) 350^{o}C showing the completion of epitaxial rearrangement of NCs and a single epitaxial orientation (Ag diffraction spots have been indexed with electron beam being parallel to Ag [11-2]), (c) 560^{o}C showing TiO_2 spots becoming stronger and Ag spots becoming weaker signifying sublimation of some Ag NCs.

B. Sublimation

The intensities of the Ag (222) diffraction spot, TiO_2 (2,0) and the specular spot are shown in Figure 3.13 as a function of temperature. The increase in the Ag (222) diffraction intensity starts right from room temperature and continues until ~315^oC (shown in dashed line in the plot). At the same time, the intensity of the TiO_2 (2,0) remains constant. This suggests that the ordering in the Ag NCs is not accompanied by significant dewetting of the substrate and is due to intra-island ordering. At 315^oC, the Ag (222) intensity begins to decrease. The decrease in the Ag (222) could come from both the conventional decrease in intensity with temperature that can be described by the Debye-Waller factor and the disappearance of the smaller Ag NCs. However, since the smaller Ag NCs do not contribute significantly to the RHEED intensity, it is expected that the decrease in the Ag (222) intensity starting at 315^oC is mainly due to the increased thermal vibrations of the Ag atoms. It also means that most of the Ag NCs become epitaxially oriented by 315^oC. The intensity of the Ag (222) spot decreases dramatically at ~525^oC, signifying the start of Ag sublimation. The intensities of the TiO_2 (2,0) and the specular spot increase dramatically at the same time signifying that the coverage of Ag is decreasing. The decrease in Ag coverage results in a larger region of the surface being exposed which causes both the TiO_2 (2,0) and the specular intensity to increase. The decrease in the Ag coverage beyond 525^oC can also be seen visually by observing that TiO_2 diffraction spot intensities in Figure 3.12 (c) are higher than Figure 3.12 (b). The Ag (222) intensity decreases till 585^oC (shown in dashed line in the plot), after which it is seen to more or less stabilize to the background value. At this point all Ag has been removed from the surface. The TiO_2 (2,0) and the specular intensities rise dramatically until 585^oC and thereafter fall down due the

conventional decrease in intensity expected from increasing temperature as described by the Debye-Waller factor.

It is seen that Ag deposited on a reduced TiO_2 (110) at room temperature completes its epitaxial formation at 315^oC even for the largest Ag island, which for a 8 nm Ag cluster is more than 80 K below the 2/3 Tm [121, 122] even if one assumes a large value of 1.4 J/m^2 for the surface energy of Ag [66, 123]. The epitaxy is dominated by one kind of orientation only. Furthermore, the sublimation temperature for complete silver disappearance is about 35 degrees lower than the sublimation temperature of Ag NCs supported on furnace oxidized TiO_2(110). These observations clearly show that the stoichiometry of the substrate plays a significant role in driving the structural change of Ag NCs on TiO_2 (110).

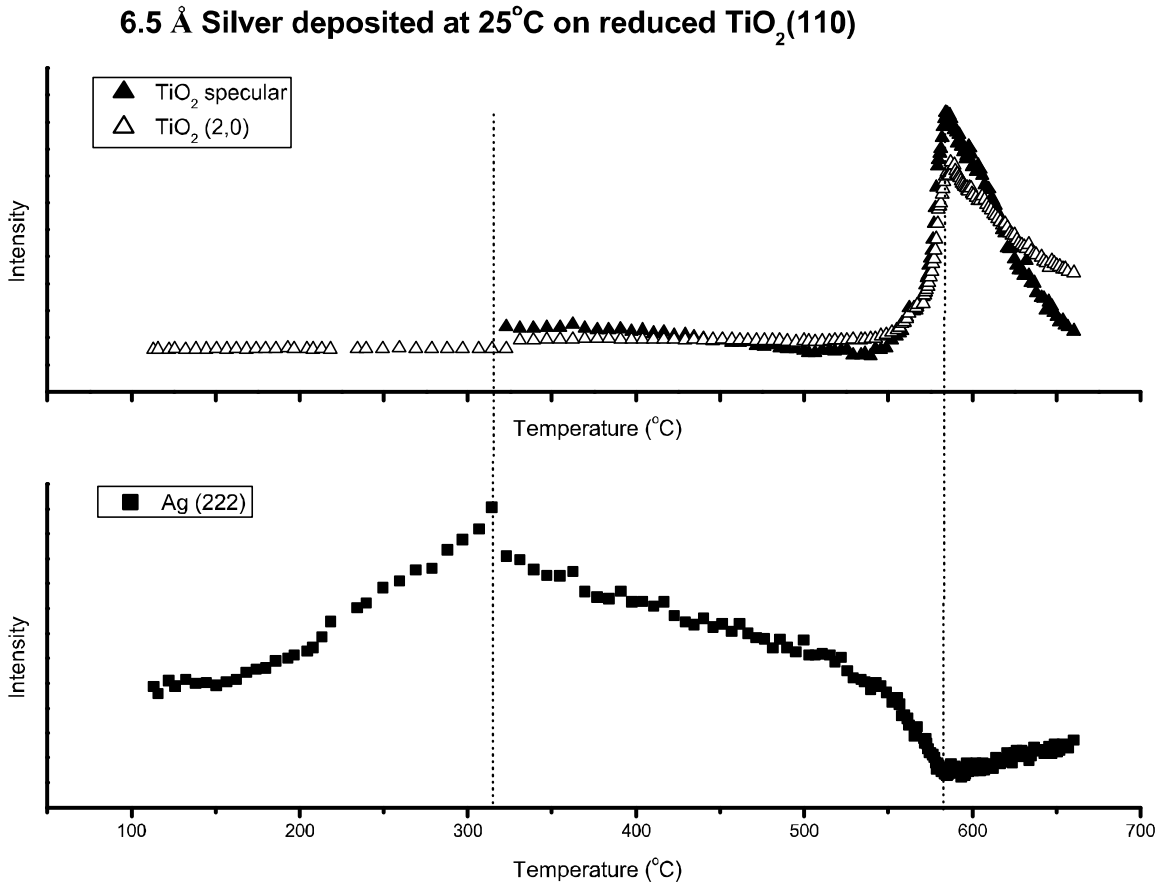

Figure 3.13: RHEED intensity versus temperature for silver nanoclusters deposited at 25°C on reduced TiO_2(110). The dashed line to the left shows the completion of epitaxial rearrangement and dashed line to the right shows the completion of sublimation.

3.3.4 Silver NCs Deposited at 350°C on Reduced TiO_2 (110)

A. Structure evolution and epitaxy

A reduced TiO_2 (110) was prepared by taking a furnace oxidized substrate (refer experimental section) and heating it to 750°C in vacuum. 6.5 Å of Ag was deposited at 350°C onto the reduced TiO_2 (110) surface. The samples were then heated at the rate of 5°C/s. The RHEED patterns in Figure 3.14 (a), (b) were taken close to the [-110] azimuth of TiO_2 (110). It is seen that there is complete epitaxy even as deposited at 350°C (Figure 3.14 (a)), which does not change in Figure 3.14 (b) which was taken close to the sublimation temperature. Figure 3.14

(c) shows a TEM micrograph of the as deposited Ag NCs at 350°C. The Ag NCs were found to be mostly epitaxial as expected with a few multiply twinned NCs also seen. For most of the epitaxial Ag NCs, the (111) plane of Ag was parallel to the surface of the TiO_2 (110). The electron beam is parallel to Ag [11-2]. Both ABCABC and ACBACB stacking were seen in the Ag NCs similar to previous observations. The predominant epitaxial orientation as seen from RHEED was –

$$(111)\ Ag \parallel (110)\ TiO_2,\ \ [-110]\ Ag \parallel [001]\ TiO_2$$

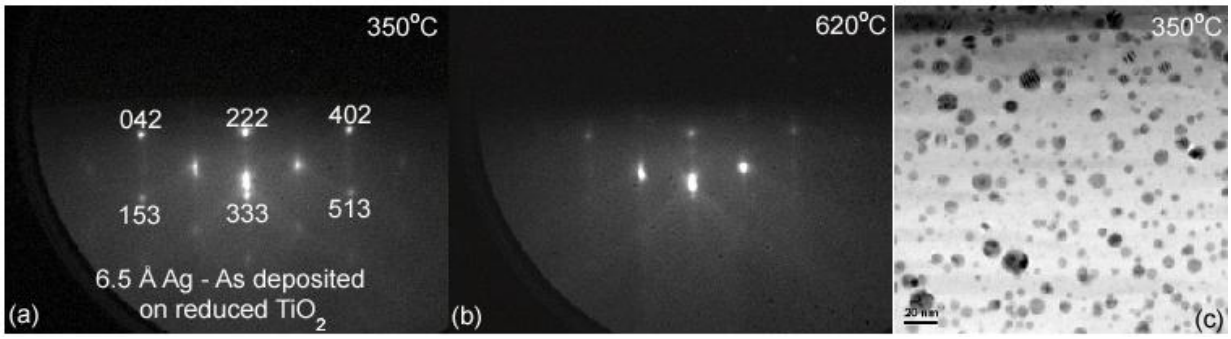

Figure 3.14: Silver nanoclusters on reduced TiO_2(110) at 350°C: (a) RHEED pattern taken along [-110] TiO_2 at 350°C showing formation of single epitaxy (Ag diffraction spots have been indexed with electron beam parallel to Ag [11-2]), (b) RHEED pattern taken along [-110] TiO_2 at 620°C showing the presence of weaker Ag diffraction spots signifying sublimation of some Ag NCs. (c) TEM micrograph of nanoclusters deposited at 350°C showing large size range of NCs.

B. Sublimation

The intensities of the Ag (222) spot, TiO_2 (2,0) and the specular spot are shown in Figure 3.15 as a function of temperature. The decrease in the Ag (222) intensity starts right from the temperature of deposition and continues till all Ag has disappeared at ~ 660°C (as shown in dashed line on the plot). The decrease in the Ag (222) could come from both the conventional decrease intensity with temperature that can be described by the Debye-Waller factor and the disappearance of the smaller Ag NCs. Noticeably, there is no further ordering of Ag NCs

indicating that the NCs formed immediately after deposition are equilibrium structures. Unlike the previous cases, there is no dramatic decrease in the intensity of the Ag (222) spot to signify the start of Ag sublimation. This is due to the fact that higher temperature depositions lead to larger size distributions for the NCs (as also seen in Figure 3.14 (c)). Consequently, the temperature of desorption of the NCs occurs over a range of temperatures. However, the largest NCs of Ag cause the greatest shadowing of the TiO_2 substrate. Hence, once the disappearance of the larger NCs begin, the TiO_2 (2,0) and the specular increase dramatically at the same time. This happens around 630^{o}C. At 630^{o}C, the TiO_2 (2,0) and the specular intensities rise dramatically until 660^{o}C (when all Ag NCs sublime) and thereafter fall down due the conventional decrease in intensity expected from increasing temperature as described by the Debye-Waller factor.

It is seen that the epitaxial relationship obtained on depositing Ag on a reduced TiO_2 (110) surface at 350^{o}C is the same as the epitaxy seen when Ag was deposited at room temperature on a reduced surface and then heated up. These results prove that the structural evolution of Ag NCs deposited on reduced TiO_2 (110) (in section B) leads to equilibrium structures for the Ag NCs and not metastable structures. Furthermore, it shows that the high temperature deposition leads to the formation of larger cluster sizes and greater size distribution in the process of obtaining equilibrium structures, while deposition on a reduced TiO_2 (110) surface at room temperature followed by annealing leads to a tighter size distribution and smaller structures for obtaining similar equilibrium structures.

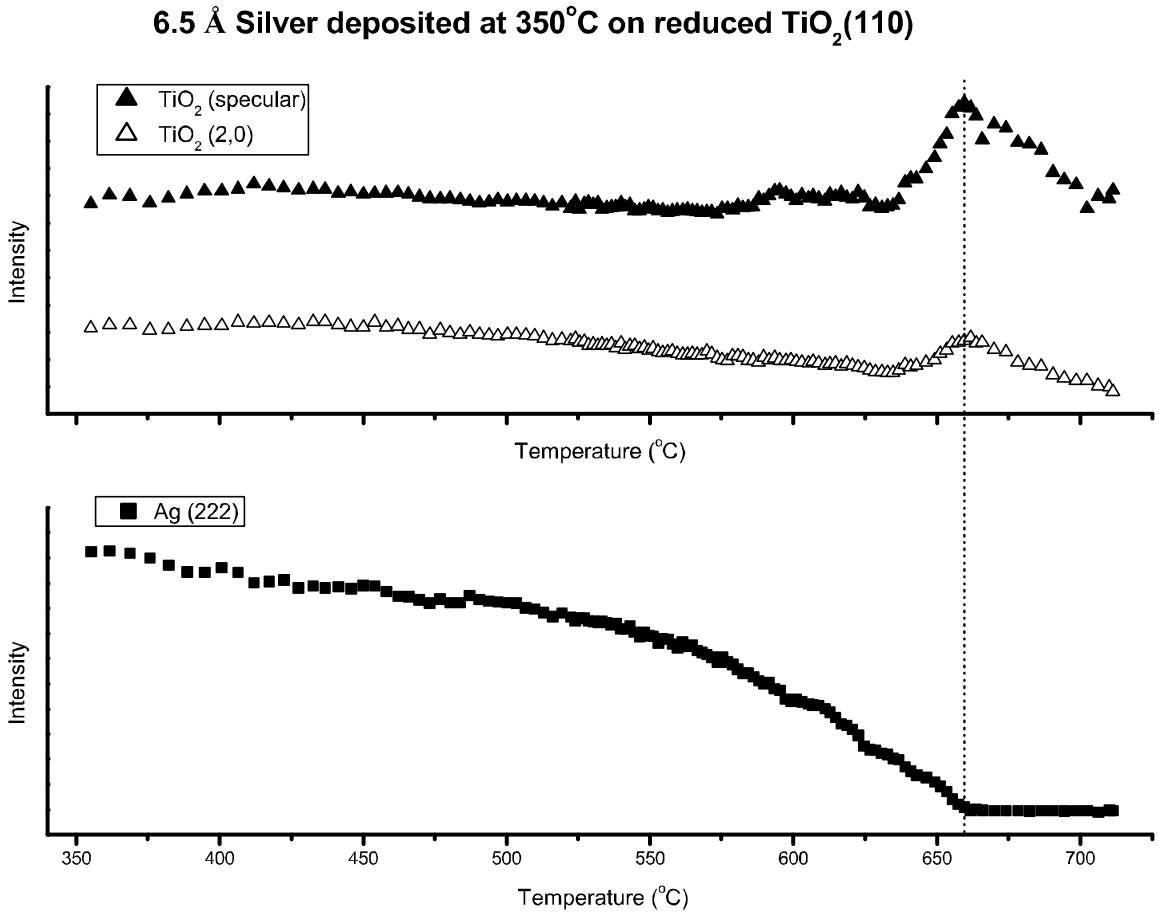

Figure 3.15: RHEED intensity versus temperature for silver nanoclusters deposited at 350°C on reduced TiO_2(110). The dashed line shows the completion of sublimation.

3.4 Discussion

3.4.1 Epitaxy of Au NCs

The stability of the commonly observed Au(111)/TiO_2(110) interface has been a subject of debate in the past. Lopez et. al. showed using DFT calculations that an ideal (1x1) oxygen terminated TiO_2 (110) surface has nearly zero adhesion for Au (111) and therefore the interface of Au (111) and defect-free TiO_2 (110) (1x1) could not be stable.[68] They suggested that the presence of oxygen vacancies and other defects as being probable causes for stabilizing the interface of Au(111) and TiO_2 (110). The observation that Au atoms and small Au clusters (<20

atoms) bind more strongly to oxygen vacancies ($O_{br\text{-}v}$) on TiO_2 (110) than O_{br} has also been broadly confirmed by various other groups.[42, 59, 62, 104, 124] However, the presence of random defects such as oxygen vacancies on TiO_2 (110), whose number and configuration have to necessarily change for the three different TiO_2 (110) surfaces in our studies, cannot account for the appearance of an identical epitaxy in all the three cases. The dominant epitaxy of Au NCs on TiO_2 (110) in our experiments does not change with different starting surfaces of TiO_2 (110) and different annealing atmospheres. While other minor epitaxial arrangements of Au NCs may be present in our experiments, the presence of only one epitaxy in all the RHEED patterns suggest that the $Au(111)_{[1\text{-}10]} \parallel TiO_2\ (110)_{[001]}$ epitaxy is highly dominant.

We argue that the stability of the $Au(111)_{[1\text{-}10]} \parallel TiO_2\ (110)_{[001]}$ epitaxy is due to the nucleation and growth of epitaxial Au NCs at areas of TiO_2 (110) that are (1x2) reconstructed. We infer this hypothesis from four key observations – (a) Au NCs on (1x2) reconstructed TiO_2 (110) surfaces nucleate as epitaxial NCs even at room temperatures, (b) Au NCs evolve to the equilibrium epitaxial configuration at lower temperatures when the bare surface is (1x2) reconstructed prior to Au deposition, (c) the coverage of Au NCs on TiO_2 (110) increases with increasing fraction of (1x2) surface reconstruction and (d) TiO_2 (110) (1x2) reconstruction is simultaneously observed along with the $Au(111)_{[1\text{-}10]} \parallel TiO_2\ (110)_{[001]}$ epitaxy in RHEED, irrespective of the stoichiometry of the starting surfaces and the details of their heat treatments.

Au NCs most likely prefer to nucleate over the (1x2) reconstruction since these reconstructions are oxygen deficient[54-56, 120] and lattice match to TiO_2 [001] along Au [1-10]. Others have also reported selective Au nucleation over (1x2) TiO_2 (110).[125, 126] In these studies, the authors use Low Energy Electron Diffraction (LEED), X-Ray Photoelectron Spectroscopy (XPS) and Density Functional Theory (DFT) to infer that Au preferentially

nucleates over missing row (1x2) reconstruction as atomic chains which lattice match along the TiO_2 [001] direction and .are separated by ~13Å along TiO_2 [-110], thus matching the periodicity of the (1x2) reconstruction along TiO_2 [-110]. The authors contend that the (1x2) reconstructions in their studies are of the missing-row type[120] and Au nucleates at these missing row (1x2) reconstructions as Au atomic chains. While we agree that Au likes to nucleate on TiO_2 (110) (1x2) reconstruction, we think the nucleation of Au on the (1x2) reconstruction is not limited to just the missing row type since we observe the same epitaxy on (1x2) reconstructions created by vacuum heating and air annealing – which most likely are not identical.

Once the first Au row is nucleated by lattice matching to the TiO_2 (1x2) reconstruction, the subsequent growth of Au NCs on top these nucleation sites is preferred since the adhesion of Au to the (1x2) reconstruction is strong.[125, 126] The growth of 3D Au NCs over the (1x2) reconstruction would result in an interfacial strain of 3% along the Au [11-2] and TiO_2 [-110] direction assuming five periods of Au with each period consisting of three Au (112) lattice planes are lattice matched to two periods of the TiO_2 (110) (1x2) reconstruction along TiO_2 [-110]. In the orthogonal direction (along TiO_2 [001]), as mentioned earlier, we expect one is to one lattice match. We note that we were not able to measure interfacial strain using RHEED since RHEED signal is dominated by larger NCs which relax to the equilibrium Au spacing away from the interface. In all of our measurements, the equilibrium spacing of Au NCs was found to be fully relaxed.

Even though we have made a strong case for Au nucleation over the (1x2) reconstruction of TiO_2 (110) using RHEED studies, we cannot prove it beyond doubt unless we are able to view the interface using microscopy. Electron microscopy analysis of this interface will be presented in Chapter 4 which agrees with all the conclusions we have arrived at with RHEED experiments.

3.4.2 Epitaxy and Sublimation of Ag NCs

Our observation of Ag NC disappearance at ~ 620^{o}C is similar to the temperature regime of disappearance of Ag islands on furnace annealed TiO_2 (110) in a previously reported study.[106] In this study, the authors noted that the density of Ag NCs decreases utmost by a factor of four even after a long period of annealing and the average size of the Ag NCs does not change significantly, which indicates that Ag NCs are quite stable after their initial formation at room temperature. Also, Scanning Tunneling Microscopy (STM) studies revealed that Ag NCs nucleate on step edges of TiO_2 (110)[105, 106] even at room temperature. Based on this observation, it was concluded that there is a high diffusion rate for Ag atoms at room temperature on oxidized TiO_2 (110) terraces. The lack of coarsening during annealing, despite a relative fast Ag diffusion on TiO_2 (110) terraces, indicates a strong bonding of Ag atoms to step edge defects. These defects are likely to provide sites for pinning of Ag atoms. We suspect that the strong bonding of the Ag atoms to the step edge defects is also responsible for the lack of the uniform epitaxy of Ag NCs on furnace oxidized TiO_2 (110) upon annealing. On a step edge, the orientation of a Ag NC is highly dependent on the details of the step edge atomic structure. The dominant epitaxial configurations possibly reflect the dominance of different step edges of the TiO_2 surface. However, further study is needed here to clarify the relationship between step edges and NC orientations.

For understanding the remarkable difference in the behavior of Ag on furnace oxidized versus reduced TiO_2, we note that DFT calculations have shown that the bonding of Ag atoms to O_{br} is much stronger than the bonding of Ag to Ti sites[60] or Ag to $O_{br\text{-}v}$. This is in contrast to Au where Au binds much stronger to $O_{br\text{-}v}$ than O_{br}. Therefore, on reduced TiO_2 (110) surfaces, where the bridging oxygen atoms are expected to be missing, it is anticipated that the adsorption

of Ag will be much weaker. This is consistent with our experimental observation that the sublimation temperature in the case of Ag NCs on furnace oxidized TiO_2 (110) is higher than reduced TiO_2 (110) by ~35 degrees. It should be noted that not all bridging oxygen atoms are missing on the reduced TiO_2 (110). The somewhat small temperature difference observed experimentally is likely an indication of a mixture of different adsorption sites at the interface of Ag NCs and TiO_2 (110).

Also, since we observe epitaxial Ag NCs form even at 100^oC on reduced TiO_2 (110) substrates, we believe that Ag nucleates on the (1x2) reconstruction by lattice matching with the (1x2) reconstruction similar to Au. Similar to Au NCs on reduced TiO_2 surfaces, the presence of small Ag NC nuclei with epitaxial arrangement should drive the reorganization of Ag NCs supported on reduced TiO_2 (110) surfaces to epitaxy at lower temperatures than furnace oxidized surfaces. Indeed this is supported by our observation that Ag NCs fully evolve to a single epitaxy - (111) Ag || (110) TiO_2, [-110] Ag || [001] TiO_2 - on reduced TiO_2 (110) at 350^oC as against 575^oC for Ag NCs on furnace oxidized TiO_2 (110). Thus, we see that the bridging oxygen atoms play a strong role in determining the bonding and epitaxy of Ag NCs to TiO_2 (110).

3.5 Summary and Conclusions

The structural evolution and epitaxy of Au NCs on TiO_2 (110) surfaces prepared in three different ways have been studied using RHEED characterization.

1. 1 Å of Au deposited on furnace oxidized TiO_2 (110) at room temperature evolves into a single epitaxial arrangement upon annealing in vacuum to 785^oC. The predominant epitaxial arrangement is –

   (111) Au || (110) TiO_2, [-110] Au || [001] TiO_2

It is seen from the RHEED intensity analysis that the onset of epitaxy happens around 750^{o}C and is completed by 750^{o}C. The TiO_2 (110) surface is seen to be (1x2) reconstructed after heating to 785^{o}C.

2. 1 Å of Au deposited on reduced and (1x2) reconstructed TiO_2 (110) at room temperature evolves into a single epitaxial arrangement upon annealing in vacuum to 750^{o}C. The predominant epitaxial arrangement is –

(111) Au || (110) TiO_2, [-110] Au || [001] TiO_2

RHEED patterns show evidence of epitaxy even at room temperatures. It is seen from the RHEED intensity analysis that the onset of epitaxy happens around 600^{o}C and is completed by 700^{o}C. The nucleation and growth of Au NCs on (1x2) reconstructed TiO_2 (110) therefore happens at much lower temperatures and is mostly likely favored by nucleation of Au atomic chains on the (1x2) reconstruction.

3. 1 Å of Au deposited on furnace oxidized TiO_2 (110) at room temperature evolves into a single epitaxial arrangement upon annealing in air to 750^{o}C. The predominant epitaxial arrangement is –

(111) Au || (110) TiO_2, [-110] Au || [001] TiO_2

The TiO_2 (110) surface is seen to be (1x2) reconstructed after heating to 750^{o}C in air. The omnipresence of the (1x2) reconstruction in all the three cases suggests that the lattice match of (1x2) TiO_2 (110) and Au/Ag is responsible for the formation of epitaxial Au NCs on TiO_2 (110).

The structural evolution, epitaxy and sublimation temperature of Ag NCs on TiO_2 (110) surfaces prepared in two different ways have been studied using a combination of in-situ RHEED characterization and ex-situ electron imaging. The results show:

1. 6.5 Å of Ag deposited on furnace oxidized TiO_2 (110) at room temperature does not get into complete or single epitaxial structure before sublimation. The predominant orientations just before sublimation are –

   (111) Ag || (110) TiO_2, [-110] Ag || [001] TiO_2

   (112) Ag || (110) TiO_2, [-110] Ag || [001] TiO_2

   It is seen from the RHEED intensity analysis that sublimation is complete at 620^{o}C. Single twinned NCs are seen to be stable even at temperatures close to sublimation. This suggests that either the local interfacial atomic arrangement causes twinned structures to be thermodynamically stable or that surface diffusion of Ag atoms on the NCs is too slow to cause significant structural change in the timescales of this experiment.

2. Ag deposited on reduced TiO_2 (110) at room temperature and 6.5 Å coverage gets into complete and single epitaxial relationship with the substrate, which can be described as-

   (111) Ag || (110) TiO_2, [-110] Ag || [001] TiO_2

   It is seen from the RHEED intensity profile that epitaxy is complete by 315^{o}C, which is 80K below 2/3 Tm of an 8nm Ag cluster, which is a typical size in this case. It is also seen that sublimation is complete by ~585^{o}C, which is significantly lower than the sublimation temperature of Ag NCs supported on furnace-oxidized TiO_2 (110). Both

these observations clearly show that surface stoichiometry plays a crucial role in the structural evolution, epitaxy and sublimation of Ag NCs on TiO_2 (110).

3. 6.5 Å of Ag was deposited on a reduced TiO_2 (110) surface at 350^oC, which is greater than 0.5 T_m of Ag. This is expected to yield equilibrium epitaxial structures. It was seen that complete epitaxy was achieved, which can be described as –

$$(111)Ag \parallel (110)\ TiO_2,\ [-110]\ Ag \parallel [001]\ TiO_2$$

This proves that the epitaxy seen in the previous case was indeed the equilibrium structure and that structural evolution on a reduced TiO_2 (110) surface can lead to the formation of equilibrium structures. Sublimation was complete at 660^oC, which is significantly higher than both the above cases. This is attributed to the presence of larger Ag NCs due to the higher deposition temperature. Unlike the previous cases, the start of desorption did not show up significantly in the RHEED. This is attributed to the larger distribution in the cluster size which results in sublimation over a larger temperature range.

Further, the similarities and differences between Au and Ag are highlighted by this study. The similar lattice parameters and atomic structures of Au and Ag cause both Au and Ag NCs to nucleate on the TiO_2 (110) (1x2) reconstruction with identical epitaxial relationships and evolve to the same epitaxy on reduced TiO_2 (110) surfaces. However, the dissimilarities in the bonding of Au and Ag to defects and oxygen vacancies results in the presence of two dominant epitaxies for Ag NCs deposited and vacuum annealed on furnace annealed TiO_2 (110) surfaces and only a single epitaxy for Au NCs processed under similar conditions.

CHAPTER 4

INTERFACIAL ATOMIC STRUCTURE AND INTERFACIAL ENERGY OF EPITAXIAL GOLD NANOCRYSTALS SUPPORTED ON TITANIUM DIOXIDE (110)

Substantial parts of materials technology, major components of chemical industry, and exciting new developments in medical diagnostics rely on the synergistic interactions at the interface of metal nanoparticles and oxide surfaces[1]. The interfacial property is largely determined by its atomic structure, however, we know little about this relationship for nanoparticles. Here we report an examination of the interface formed between gold nanocrystals (NCs) and the TiO_2 (110) surface, which is a model oxidation catalyst[30, 33, 37, 41]. Using aberration corrected scanning transmission electron microscopy (STEM), we observed direct evidence of interface reconstruction for epitaxial Au NCs with $Au(11\bar{1})||TiO_2(110)$. The reconstructed interface is formed by Au atoms sitting between added-rows of TiO_2 (110) (1x2) reconstruction,[54] resulting in a single atomic layer of Au, Ti and oxygen, as evidenced by atomic scale electron spectroscopy. It has a significantly lower interfacial energy by ~0.5 J/m^2 compared to interfaces without reconstruction. The interface is also stable under high temperature annealing. First-principles calculations suggest that the interfacial Au atoms are ionized with a valence of 1.5.

4.1 Introduction

In 1878, Gibbs had proposed that the equilibrium shape of a droplet or a crystal will be the one that minimizes the net surface energy of the droplet or crystal. In other words, the crystal will adopt that shape which minimizes the quantity $G_{Crystal} = \sum_i \gamma_i A_i$, where "i" represents each

facet. In 1901, Wulff stated that the length of the vector (h_i) drawn from the center of a crystal normal to a facet "i" will be proportional to the surface energy of the facet (γ_i),[127] i.e.

$$\frac{h_i}{\gamma_i} = \text{Constant} \qquad (4.1)$$

The Wulff theorem was later proved by many others and found to be exact in both two and three dimensions.[128-130] Kaishew is credited with modifying the Wulff theorem for predicting the equilibrium shape of supported crystals which have an interface.[131] The following derivation of the Wulff-Kaishew has been reproduced from Kern et al.[132]. The excess free energy of a supported nanocluster with n atoms with interfacial line tension can be expressed as

$$\Delta G(n) = -n\Delta\mu + \sum_{j \neq Int} \gamma_j A_j + (\gamma_{Int} - \gamma_{TiO_2}) A_{Int} \qquad (4.2)$$

where ΔG and $\Delta\mu$ are the excess free energy and chemical potential difference between a Au atom in the gas phase and a Au atom in the nanocluster respectively, n is the number of atoms in the nanocluster, γ_j and A_j are the surface energy and surface areas of the free surfaces, and γ_{Int} is the interfacial energy. Noting that

$$V = n\nu \qquad (4.3)$$

where V is t he volume of the nanocluster and ν is the atomic volume, and

$$V = \frac{1}{2}\left(\sum_{j \neq Int} h_j A_j + (h - \Delta h) A_{Int} \right) \qquad (4.4)$$

where, hj is the distance from the centre of the nanocrystal to the centroid of the facet (Figure 4.1), the derivative of ΔG can be written as –

$$d\Delta G(n) = -\frac{\Delta\mu}{2\nu}\left(\sum_{j=Int} h_j dA_j + (h-\Delta h)dA_{Int}\right) + \sum_{j\neq Int}\gamma_j dA_j + (\gamma_{Int} - \gamma_{TiO_2})dA_{Int} \quad (4.5)$$

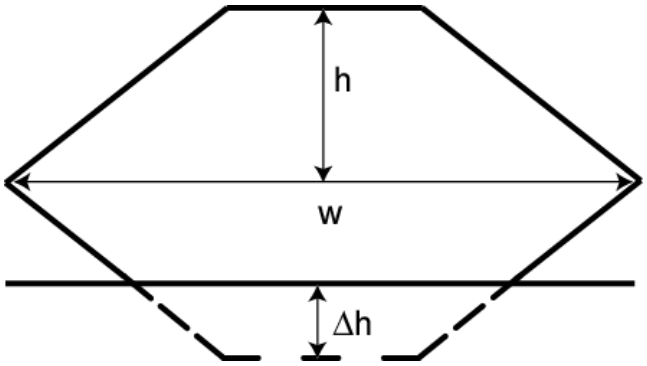

Figure 4.1: Schematic illustration of a supported nanocrystal. “h” is distance from the center of the crystal to the facets. “Δh” is the undercut. “w” is the width of the NC.

Using the partial equilibria conditions

$$\left(\frac{\partial\Delta G}{\partial A_{Int}}\right)_{A_j,\ldots,T,\Delta\mu} = 0 \quad (4.6)$$

$$\left(\frac{\partial\Delta G}{\partial A_j}\right)_{A_i,\ldots,A_{Int},T,\Delta\mu} = 0 \quad (4.7)$$

we get,

$$\frac{(\gamma_{Int} - \gamma_{TiO_2})}{h-\Delta h} = \frac{\Delta\mu}{2\nu} \quad (4.8)$$

$$\frac{\gamma_{Au}}{h} = \frac{\Delta\mu}{2\nu} \quad (4.9)$$

where γ_{Au} is the surface energy of the gold surface facet parallel to the interface.

Combining equations (7) and (8) we get,

$$\frac{(h - \Delta h)}{h} = \frac{(\gamma_{Int} - \gamma_{TiO_2})}{\gamma_{Au}} \qquad (4.\ 10)$$

The above equation is fundamentally similar to the effect of interfacial energy on the shape of liquid droplets. It can be seen from the above equation that as the interfacial energy of an interface is lowered, the undercut (Δh) increases, that is the crystal wets the support as the interfacial energy decreases. This is illustrated schematically in Figure 4.2.

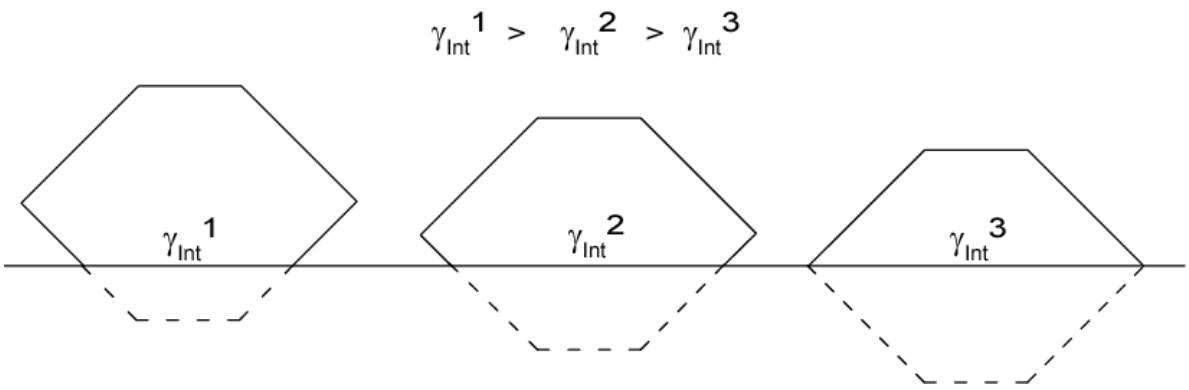

Figure 4.2: Schematic illustration of wetting with decreasing interfacial free energy. The dashed lines are a guide to the eye and depict increasing undercut with decreasing interfacial energy.

An alternative description of the interfacial formation energy is the work of adhesion (W_{adh}) defined originally by Dupré, where

$$W_{adh} = \gamma_{Au} + \gamma_{TiO_2} - \gamma_{Int} \qquad (4.\ 11)$$

which represents the net energy gained from forming an interface. A lower interfacial energy results in a larger work of adhesion (W_{adh}). Scaling the work of adhesion by the surface of energy of the nanocrystal facet forming the interface gives the relative work of adhesion as -

$$\frac{\Delta h}{h} = \frac{W_{adh}}{\gamma_{Au}} \qquad (4.\ 12)$$

The relative work of adhesion is a convenient measure for comparing the relative adhesive strengths of interfaces formed between disparate materials.

Using the Wulff-Kaishew principle, the work of adhesion and interfacial energies of many interfaces have been determined. It must be noted that all these measurements rely on the shape information of the crystals. Since the shape provides only relative values of W_{adh} and γ_{int} , (scaled by the surface energy), one has to know the surface energy apriori in order to find absolute values of W_{adh} and γ_{int}. However experimental determination of surface energies is often extremely difficult and many authors use theoretically calculated surface energies in order to obtain absolute values for W_{adh} and γ_{int}. Similar to other researchers, we have also used theoretical estimates for the surface energy to provide reasonable estimates for W_{adh} and γ_{int}, but we note that shape measurement experiments such as ours can quantitatively measure only relative W_{adh} and γ_{int}, i.e. W_{adh}/γ_{Au} and $\gamma_{int}/\gamma_{Au.}$ For the surface energy of gold, we use the first-principles calculations by Vitos et al.[66] For the surface energy of TiO_2, we use the measurement from a droplet based method[67] in order compare our measurements with other reports that use the droplet based value for TiO_2 (110) surface energy.[63]

Some of the experimental techniques that have been used to determine the shapes (and hence the interfacial energy) of metal nanocrystal-oxide support systems are – Transmission Electron Microscopy (TEM) [63, 133], Scanning Electron Microscopy (SEM)[134] and Scanning Probe Microscopy (SPM) [135]. The results of some previous studies are summarized in Table 4.1 below. Since absolute values of W_{adh} and γ_{int} do not make sense when comparing interfaces formed by different surfaces/materials, $\Delta h/h$ has been tabulated in Table 4.1. Higher ($\Delta h/h$) implies stronger adhesion.

Metal	Oxide	Crystal Size (nm)	Δh/h	Comments	Technique	Reference
Au (111)	TiO_2 (110)	150	0.39	3D	Cross sectional TEM	[63]
Au (111)	TiO_2 (110)	5	0.47	3D-Circular	Cross sectional TEM	[63]
Au (111)	Sapphire (0001)	550	0.35	3D	Cross sectional TEM	[133]
Au (001)	Sapphire (0001)	570	0.37	3D	Cross sectional TEM	[133]
Cu (111)	Sapphire (0001)	4-6	1.48	2D	STM	[136]
Pd (111)	Sapphire (0001)	4	1.70	2D	STM	[137]
Au (111)	Graphite	< 4000	0.38	3D	SEM	[134]
Cu (111)/	ZnO (0001)	4-6	1.54	2D	STM	[138]

Table 4.1: Experimentally measured undercut for various metal/oxide systems

For smaller nanocrystals (<10nm), interfacial energies have not been extensively measured [139]. The prime difficulty with measuring interfacial energies of smaller nanocrystals, is the lack of an experimental technique that can image the interface, facets and the equilibrium shape of nanoclusters supported on model atomically flat surfaces. As seen from the above table, SEM can be used only for bigger crystals. Cross sectional TEM is useful for bigger NCs (>10nm), but cross sectional sample preparation methods can lead to modifications of the surface atomic structure of smaller clusters. Scanning probe microscopy (SPM) was successful in

determining the interfacial energy of 2-D metal NCs in a few systems[136-138]. However, generally SPM has difficulties with many 3-D metallic NCs [97, 105, 140-144], in general due to lack of atomic resolution, and since interpretation of SPM data involves deconvoluting the particle-tip interactions. Therefore, a more direct method is sought to address the issue of measuring interfacial energies of small NCs. The sample preparation method we have developed (described in detail in Chapter 2) presents a novel way of measuring interfacial energies of smaller NCs.

Another issue with the study of nanocrystal interfaces is the general inability to directly probe the interface's atomic and electron structure. While 2D (thin film/ superlattice) interfaces can be interrogated by a combination of techniques including X-ray diffraction, atom probe and electron microscopy and first-principle calculation studies[145], only atom probe and electron microscopy are sensitive to nanoscale interfaces. However, both techniques require significant improvement in resolution for atomic structure determination of NC interfaces. In particular, conventional cross-sectional sample preparation methods, which are found to be rather adequate for obtaining high quality experimental data[146] from thin interfaces, can alter NCs smaller than 10nm. Also, coating the NCs with polymeric materials reduces the signal to noise ratio from the interface in a TEM/STEM. These are serious limitations that restrict our ultimate ability to obtain high quality data from NC interfaces. Other direct microscopy techniques such as SEM and STM cannot image the interface either (except in very special situations[147]).

The novel cross-sectional sample preparation method we have developed not only helps measure interfacial energies but also presents a neat system for studying the interfacial atomic structure, electronic structure and interfacial energy of small supported NCs using TEM/STEM. We have used the above method to characterize the interface of Au NCs supported on TiO_2 (110)

which has been the subject of a long debate in the catalyst community (as described in detail in Chapter 1). The following section describes our work on the interfacial energy, atomic structure and electronic structure of Au NCs supported on TiO_2.

4.2 Au-TiO_2 Interface

The atomic structure of Au/TiO_2 interfaces has been a subject of considerable speculation [37, 96]. Au nanoclusters (NCs), when supported on reducible oxides like TiO_2, show unusual size-dependent catalytic activity, including the oxidation of CO at low temperatures[30, 31, 37, 41, 63, 148]. Bulk Au however is chemically inert. In supported Au NCs, the simultaneous presence of Au cations next to metallic Au atoms has been suggested crucial for catalytic activity of Au [31, 33, 37]. Despite many proposals, so far there has been no 'direct' study of interfacial Au atoms.

Nanoparticle interfaces, in general, are difficult to characterize. While 2D (thin film/ superlattice) interfaces can be interrogated by a combination of techniques including X-ray diffraction, atom probe and electron microscopy and first-principle calculation studies[145], only atom probe and electron microscopy are sensitive to nanoscale interfaces. However, both techniques require significant improvement in resolution for atomic structure determination of NC interfaces. In particular, conventional cross-sectional sample preparation methods, which are found to be rather adequate for obtaining high quality experimental data[146] from thin interfaces, can alter NCs smaller than 10nm. Also, coating the NCs with polymeric materials reduces the signal to noise ratio from the interface in a TEM/STEM. These are serious limitations that restrict our ultimate ability to obtain high quality data from NC interfaces. Other direct microscopy techniques such as SEM and STM cannot image the interface either (except in special situations[147]).

We used aberration corrected scanning transmission electron microscopy (STEM) in the cross sectional geometry for the characterization of Au NC interfaces by developing a novel way to prepare NC interfaces. The high resolution (< 1 Å) allows for direct visualization of individual interfacial atomic columns in projection, which has proved to be extremely useful for understanding atomic and electronic structure of interfaces[149-152]. Furthermore, the quantitative dependence on Z in the STEM image contrast obtained using a high angular annual dark field (HAADF) detector[153] allows determination of the nanocrystal shape and its interfacial energy, as we will show here.

The interface between Au nanocrystals and rutile (110) surfaces was formed by deposition of few monolayers of Au atoms followed by annealing. The (110) is most stable among different rutile surfaces. The structure of rutile (110) ranges from the fully oxygenated (1x1) structure to reconstructed oxygen deficient (1x2), (1x3) structures, rosettes etc[49]. For our TEM study, the TiO_2 crystal was first thinned and then annealed in air to promote the formation of TiO_2 surface facets. Previous studies have shown that upon deposition Au forms 2-3 monolayer high, randomly oriented nanoparticles[154] and after annealing there is a tendency to form epitaxial nanocrystals[63]. The formation of Au NCs on the top, bottom and side surfaces of the TiO_2 crystal was achieved by sputtering and annealing. Annealing promotes epitaxial nanocrystal formation[113]. The sizes of Au NCs ranged from 5nm to 12nm in width depending upon the annealing conditions. More details of sample preparation are given in Chapter 2.

4.3 Epitaxy and Equilibrium Nanocrystal Shapes

Figure 4.3 shows images of epitaxial Au NCs supported on a thin slab of TiO_2 crystal. The TiO_2 crystal in Figure 4.3 (a) recorded by HAADF-STEM has two side surfaces, both belong to (110); one is relatively flat and the other has a large miscut with many surface steps.

The density of the NCs is higher on stepped surfaces, where the surface steps provide preferential nucleation sites. The facets of larger NCs are also visible. The two TEM images in Figure 4.3 (b),(c) represent two different epitaxies of Au NCs observed on TiO_2 (110). The Au NC in Figure 4.3 (b) with a hemispherical shape is oriented along the Au [112] zone axis. In this orientation, the Au atoms are arranged in a rectangular lattice defined by the basis lattice vectors of $Au[11\bar{1}]$ and $Au[1\bar{1}0]$. The epitaxy in Figure 4.3 (b) can be described as $Au(11\bar{1}) \| TiO_2(110)$ and $Au[1\bar{1}0] \| TiO_2[001]$. This was the most common type of epitaxy that we observed and will be henceforth referred as $Au_{[112]}$. This epitaxy has also been reported earlier by vacuum deposition and annealing[102] as well by precipitation and calcination[69]. The Au NC in Figure 4.3 (c) with a large dewetting is oriented along the Au [110] zone axis. The epitaxy in Figure 4.3 (c) can be described as $Au(001) \| TiO_2(110)$ and $Au[1\bar{1}0] \| TiO_2[001]$, which will be referred as $Au_{[110]}$. This epitaxy was much less frequently observed than $Au_{[112]}$.

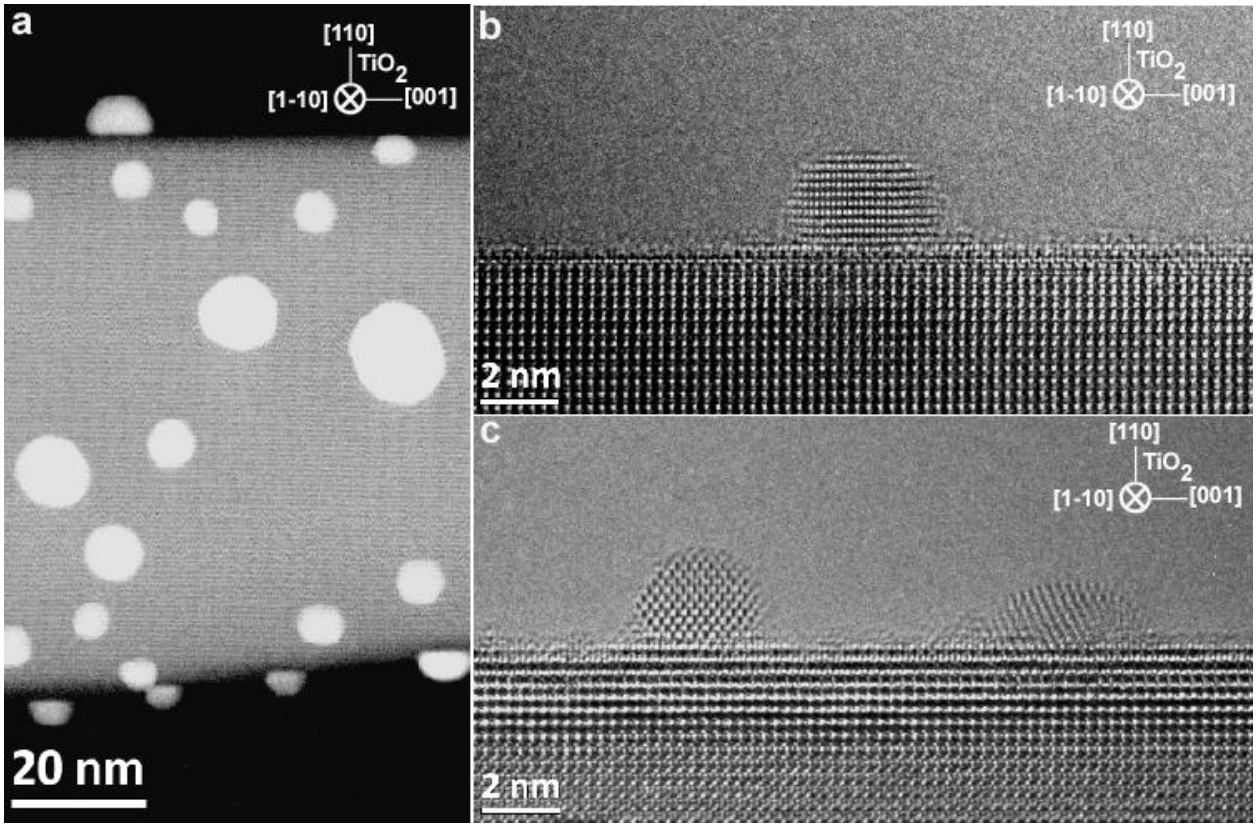

Figure 4.3: (a) Low-magnification STEM image of Au NCs supported on TiO_2(110). The NCs on the edge were used in this study. High resolution TEM images of two types epitaxial Au nanocrystals: (b) $Au_{[112]}$ and (c) $Au_{[110]}$ NC.

In order to determine the shape of the NCs, we examined the atomic resolution contrast of the two types of epitaxial NCs recorded by HAADF-STEM (Figure 4.5). The nanocrystals were imaged along the TiO_2 $[1\,\bar{1}\,0]$ direction. The atomic columns of Au are clearly resolved in both cases. The Au atomic columns appear bright and the Ti atomic columns appear much duller due to the Z-contrast. Superimposed on the experimental images are estimated equilibrium (Wulff) shapes of supported NCs. The parameters used for modeling are the ratio of distances to the {100} and {111} facets, corresponding to the ratio of the surface energies of {100} and {111}, or $\gamma_{100}/\gamma_{111}$. The NC facets are obvious for the $Au_{[110]}$ NC as seen in Figure 4.4 (a). The fit for the NC shape gave $\gamma_{100}/\gamma_{111}$=1.14. The nanocrystal was viewed along the [110]

orientation of Au. For the $Au_{[112]}$ NC shown in Figure 4.5 (b), the fit was obtained with $\gamma_{100} / \gamma_{111}$ = 1.06. There is noticeable edge roughness at the top and side surfaces in this case. Because of this, the nanocrystal facets are not obvious in this image. Thus, we performed modeling and simulations of image contrast to establish the NC shape of $Au_{[112]}$ NCs.

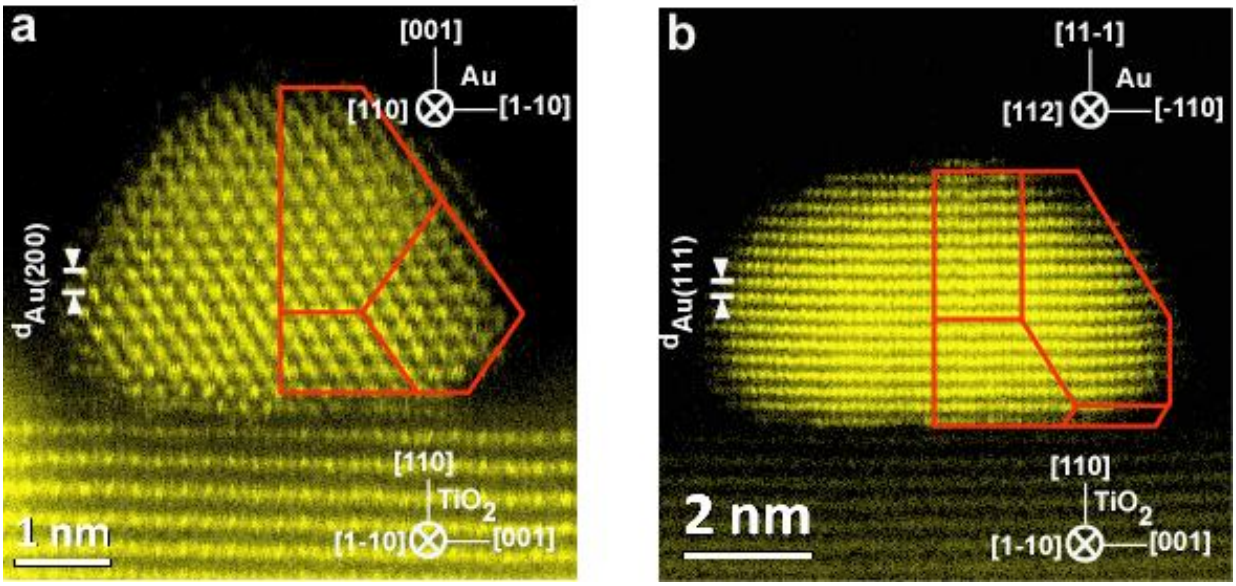

Figure 4.4: (a) and (b) Atomic resolution HAADF-STEM images of two Au NCs of different epitaxy. A model of the Au shape is overlaid on half of the NC in each case.

Figure 4.5 (b) shows a line profile along the width direction of a smaller (dia = 4.3nm) $Au_{[112]}$ NC Figure 4.5 (a). Figure 4.5 (c) shows a line profile along the height direction of the smaller $Au_{[112]}$ NC in Figure 4.5 (a). The change in the slope of the experimental intensity profile is reproduced by the simulation (the discrepancy between the experiment and simulation in Figure 4.5 (c) at the interface is a key point and will be discussed later). Based on these evidences, we concluded that both $Au_{[110]}$ and $Au_{[112]}$ NCs are faceted, with additional corner and edge roughness, as expected from the contribution of entropy to the free energy[135]. As a side

note, we observed in both cases that the models give surface energy ratios less than the theoretical value of $\gamma_{100}/\gamma_{111}$=1.268 [66].

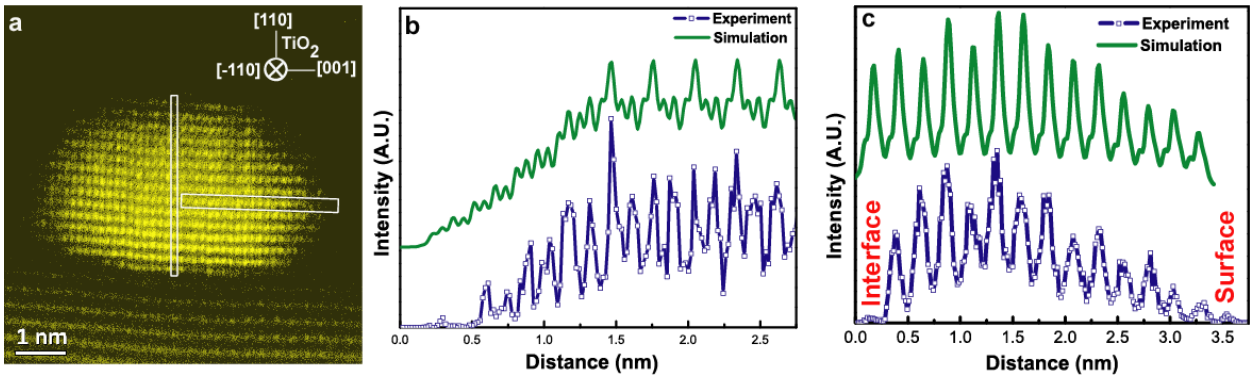

Figure 4.5: (a) Atomic resolution HAADF-STEM image of smaller $Au_{[112]}$. Experimental and simulated (blue) (b) horizontal and (c) vertical line profiles from the $Au_{[112]}$ NC in (a). The simulation used the crystal shape model and multiple scattering as implemented by the multislice method.

4.4 Interfacial Atomic Structure

The combination of Z-contrast and atomic resolution as evidenced above allows a direct examination of the interface atomic structure between the Au NC and TiO_2. Figure 4.6 (a) shows a magnified image of the $Au_{[112]}$ interface imaged by HAADF-STEM. The (111) Au close packed planes ($d_{Au(111)}$ = 2.35 Å) are parallel to the interface and the (220) Au atomic columns perpendicular to the interface ($d_{Au(220)}$ = 1.44 Å) are clearly resolved. The TiO_2 substrate is imaged along its $[1\,\bar{1}\,0]$ zone axis; two types of atomic columns are seen – 'Ti-only' columns and 'Ti-O' columns, which have the same number of Ti atoms as the Ti-only columns and two extra oxygen atoms for every Ti atom. Ti-O columns have a stronger HAADF signal than Ti only columns[101] as supported by simulation.

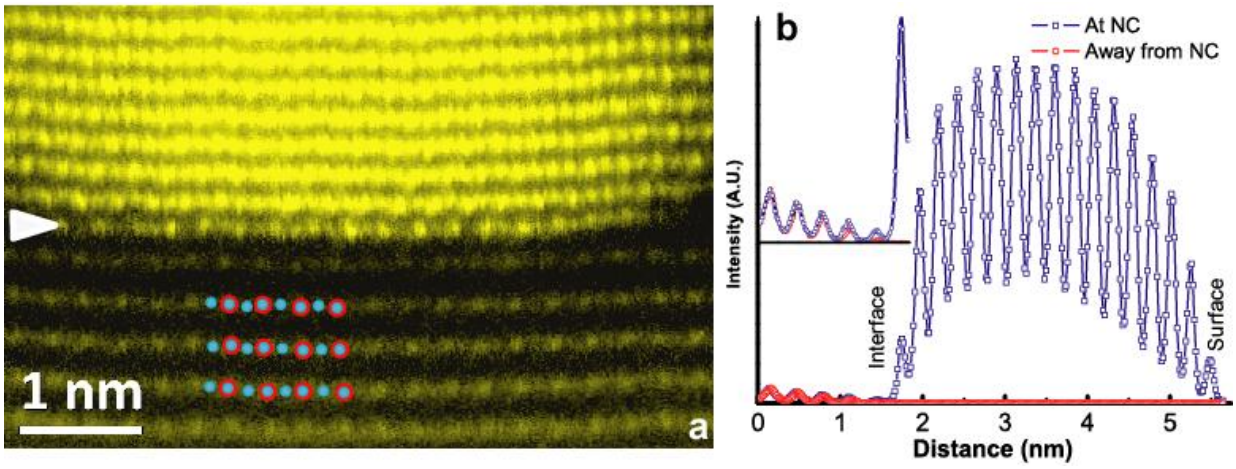

Figure 4.6: (a) Magnified HAADF-STEM image of the $Au_{[112]}$ NC interface. The Ti-O columns (red and blue dots) and Ti-only columns (blue dots) are indicated. The arrow points to the interface with alternating dark and bright atomic columns. (b) Line profiles (averaged over ~2.5 nm) at (blue) and away from (red) the Au NC in (a). The inset shows a magnified view of the profile below the interface.

The intensity line profile (averaged over ~2.5nm) across the interface has been plotted in Figure 4.6 (b). The red and the blue curves are line profiles taken from regions inside and away from the NC respectively. The position of the interfacial layer is indicated by the first peak where difference between the red and blue curves is significant (inset in Figure 4.6 (b)). This peak has been labeled as the interface in Figure 4.6 (b).

The blue intensity curve gradually decreases towards the surface of the NC (right side of the plot) because the equilibrium shape of a Au NC tapers towards the surface resulting in lesser number of Au atoms per column (along the viewing direction) at the surface compared to the center of the NC. It is well known that as the number of atoms per column decreases, ADF intensity in STEM becomes weaker. At the interface however, something unexpected happens. The intensity of the interfacial Au atomic layer is abruptly lesser than its neighboring Au layer. The abrupt decrease in interfacial intensity is unlike the gradual change in intensity observed

between successive Au(111) planes away from the interface. Additional NCs with similar interfacial contrast are presented in Figure 4.7, Figure 4.8 and Figure 4.9.

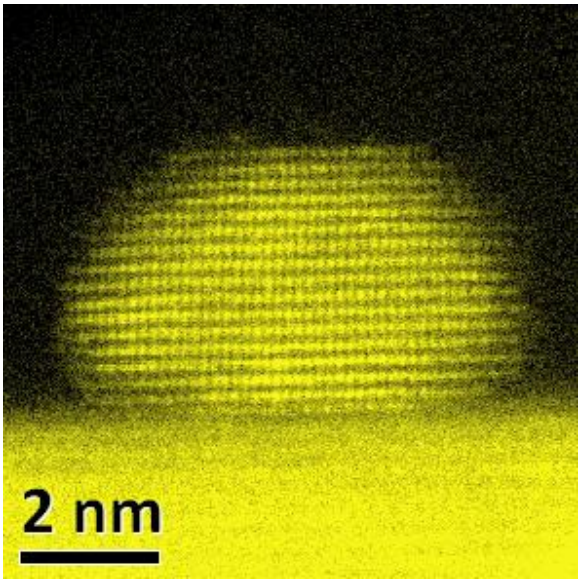

Figure 4.7: An $Au_{[112]}$ NC of 6.7nm in width

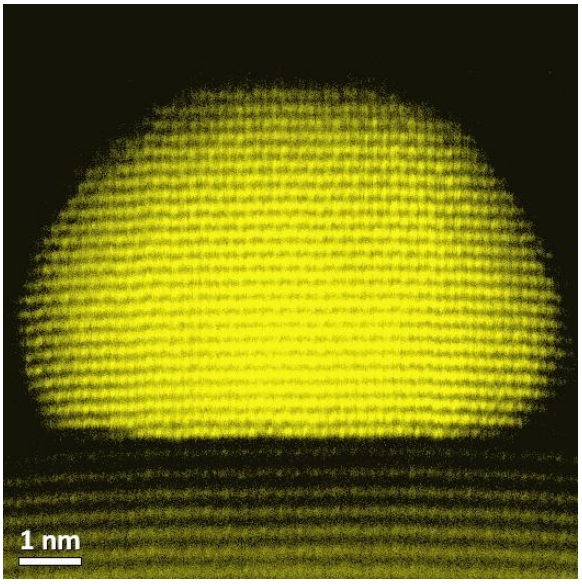

Figure 4.8: An $Au_{[112]}$ NC of 8.5 nm in width

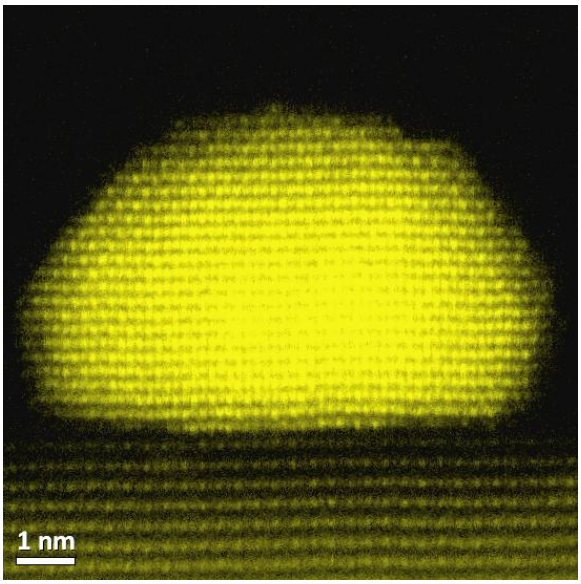

Figure 4.9: An $Au_{[112]}$ NC of 9.0 nm in width

In Figure 4.10, we have plotted the integrated intensity scan taken perpendicular to the interface (similar to Figure 4.6 (b)) from $Au_{[112]}$ NCs shown in Figure 4.5 (b), Figure 4.6 (a), Figure 4.7, Figure 4.8 and Figure 4.9. It is seen that all the $Au_{[112]}$ NCs show a abrupt drop in intensity at the interface and a more gradual drop in intensity between successive Au layers away from the interface. The much smaller STEM intensity at the interface implies that the number of Au atoms in the interfacial layer (along the viewing direction) is much smaller than what is theoretically expected of a FCC close packed Au (111) plane. In order to verify this hypothesis quantitatively, we simulated the STEM line profile from a model $Au_{[112]}$ NC with a Wulff shape and compared it to the experimental line profile of $Au_{[112]}$ NCs (Figure 4.5 (c)). It was seen that the simulated STEM intensity (green curve) of the interfacial layer from the model $Au_{[112]}$ NC was orders of magnitude larger than the observed STEM intensity (blue curve). This proves that the interfacial layer in our experimental images is not a close packed Au(111) layer, but has a different atomic configuration with much lesser Au atoms along the viewing direction than a close packed Au(111) layer.

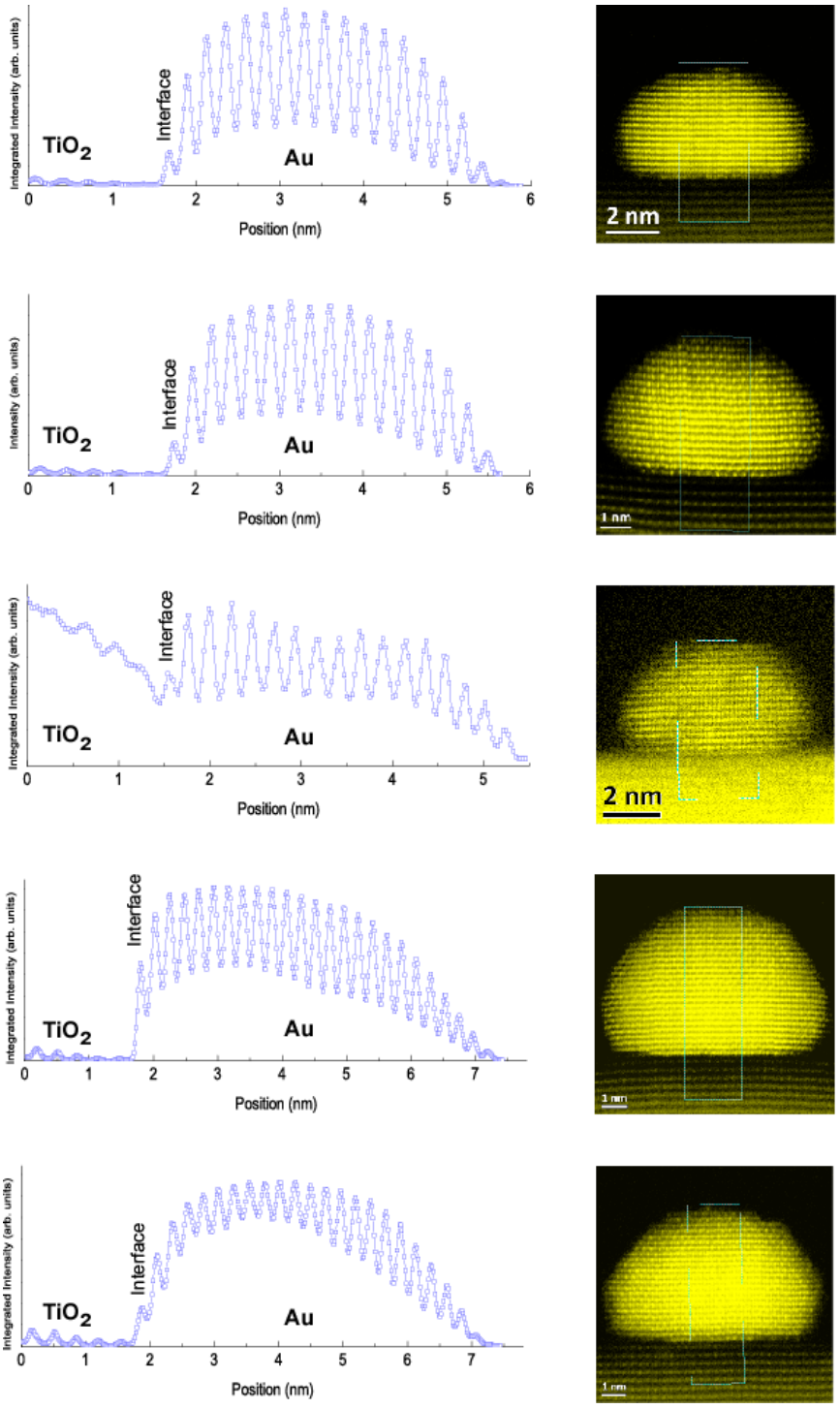

Figure 4.10: Integrated intensity plots from five Au[112] NCs demonstrating the abrupt drop in intensity at the interface.

In order to understand the atomic structure and composition of the interface we took a closer look at the interface. We found periodically altering bright and dark Au columns in the interfacial layer (indicated by arrow in Figure 4.6 (a)). The bright columns appeared on top of dark Ti-only columns of the substrate. Since it is hard to visually recognize the periodically appearing intensity in the figures, we have plotted the intensity (Figure 4.11) of the interfacial row parallel to the interface (squares, red line) for Figure 4.6 (a), Figure 4.7 and Figure 4.9 and compared it to the intensity line scan away from the interface (triangles, green line). All the images were processed by smoothing in order to get rid of scan noise in the line scans. Away from the interface (green curves), we see that there is a small modulation in STEM intensity between atomic columns that arises due to different number of Au atoms per column along the viewing direction in a typical Au NC. The modulation in the contrast away from the interface (green curve) has been reproduced in our simulated horizontal line scan in Figure 4.5 (b). The spacing between strong peaks in the curve was 1.44Å which is consistent with the d-spacing between Au(220) lattice planes. At the interface, however there is a much stronger drop in intensity (pointed out with arrows) with a periodicity of 2.89Å. Because of the periodic drop in the intensity, the spacing between the strong peaks at the interface is seen to be 2.89Å at the interface.

The periodic intensity cannot be seen throughout the interface in Figure 4.6 (a), Figure 4.7, Figure 4.8 and Figure 4.9. This happens for two reasons. Firstly, the interface of Au and TiO_2 in our specimens is not perfect. We believe that Au nucleates in between reconstructed TiO_2 (discussed in more detail later). This reconstruction does not fully cover the surface of TiO2 (110). As a result the interface is not perfect throughout the entire length of the interface. However, such an interface still provides a strong nucleation for equilibrium shaped Au NCs

above itself. Secondly, the presence of surface steps on TiO_2 along the viewing direction can alter the Z-contrast signal from the interfacial layer, particularly away from the center of the interface where only few Au atoms are available to contribute to STEM intensity along the viewing direction. Surface steps along the viewing direction is the norm and one does not expect to normally observe the interfacial layer without any interference from the surface steps during cross-sectional STEM imaging of supported NCs.

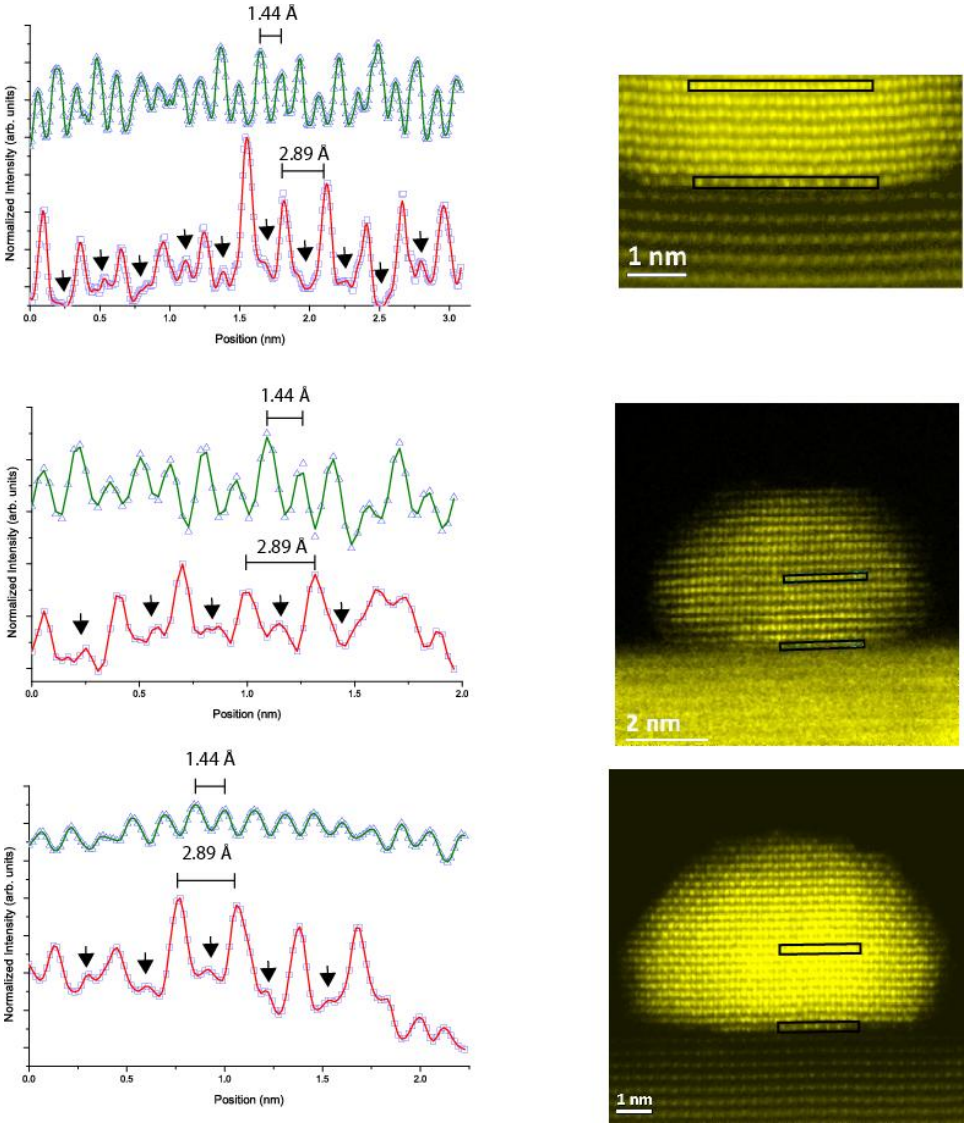

Figure 4.11: Intensity line scans at interface (squares, red line) and away from interface (triangles, green line) from four $Au_{[112]}$ NCs. The arrows point to the reduced intensity in the interfacial line scan appearing with a periodicity of ~ 2.89Å. The peak to peak separation of strong peaks is 2.89Å at the interface in contrast to 1.44Å away from the interface.

In comparison to the $Au_{[112]}$ interface discussed above, the $Au_{[110]}$ NC shown in Figure 4.4 (a) or other $Au_{[110]}$ NCs we observed, bright atomic columns were also seen at the interfacial layer, but they were not periodic as in Figure 4.6 (a). Since there is a defined periodic array of alternating bright and dark spots at the interface of $Au_{[112]}$ NCs that cannot be explained by close packed FCC Au(111) atomic arrangement and because the interface of $Au_{[112]}$ NCs has lesser

number of Au atoms than a close packed FCC Au(111) arrangement, we propose that a special reconstructed interface exists for $Au_{[112]}$ NCs. In the following, we will describe in detail the atomic structure of this reconstructed interface by combining our experimental observations and prior investigations of the TiO_2(110) surface.

Firstly, we found that the spacing between the interfacial layer and its neighboring TiO_2 layer was 3.2±0.4Å, which is close to the bulk TiO_2 (110) spacing. Secondly, the atomic arrangement of the interface atoms along TiO_2 [001] direction has the same periodicity as bulk TiO_2 itself along the same direction. Because the interfacial layer maintains the same lattice structure of bulk TiO_2 and has Au atoms in it (judging from STEM-contrast) we propose that Au atoms are located in between reconstructed Ti and O atoms on a reconstructed TiO_2 (110) surface wherein missing atoms in the surface reconstruction provide nucleation sites for Au atoms. Since we observed that all atomic columns at the interface follow the lattice of bulk TiO_2, we infer that the TiO_2 (110) surface reconstruction has to be such that when viewed from TiO_2 [001] direction, the atomic positions of the surface reconstruction are same as bulk TiO_2. Among the many stable reconstructions of TiO_2 reported [49, 54, 56], the only one we found that fit the above requirement was the (1x2) TiO_2 (110) reconstruction proposed by Pang et. al.[54] In this reconstruction, the TiO_2 (110) surface is reduced (has no bridging oxygen atoms) and every second row of 4-c Ti and O below the 4-c Ti are missing when observed along TiO_2 [001] (Figure 4.12) .[49, 54]

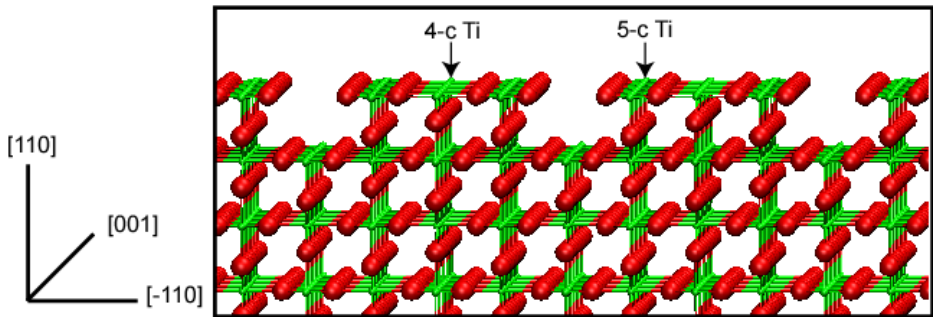

Figure 4.12: (1x2) reconstruction of TiO_2 (110) proposed by Pang *et. al.*

The interfacial reconstruction we propose has Au atomic columns occupying the missing Ti-columns with a periodicity of 16.96 Å ($4xd_{TiO2(-110)}$) when viewed along TiO_2 [001] (Figure 4.13 (a)). To determine the position of the Au atoms along TiO_2 $[1\bar{1}0]$ we go back to our experimental images (which were always taken close to TiO_2 $[1\bar{1}0]$ zone axis) and see that the brighter interfacial atomic columns always appear above the duller (Ti-only) columns of TiO_2 substrate. Thus Au atoms occupy Ti-only columns at the interface when viewed along TiO_2 $[1\bar{1}0]$. This is shown schematically in Figure 4.13 (b). When viewed normal to the interface (along TiO_2 [110] - Figure 4.13(c)) the proposed interfacial reconstruction has Au atoms occupying the interstice between four coplanar- oxygen atoms neighboring the missing Ti row. The presence of the four co-planar oxygen atoms allows only 2.14 Å for Au atoms to be accommodated in the interstice, while the diameter of a metallic Au atom is ~3.2Å. Hence, we suspect that some or all of these nearest neighbor oxygen atoms might be missing in the reconstruction. In order to show that the oxygen sites next to Au could be vacant, we have shaded co-planar oxygen atoms neighboring Au (marked by arrows in Figure 4.13(c)). Since STEM imaging is not sensitive to scattering from oxygen atoms, the above hypothesis needs to be verified by theory.

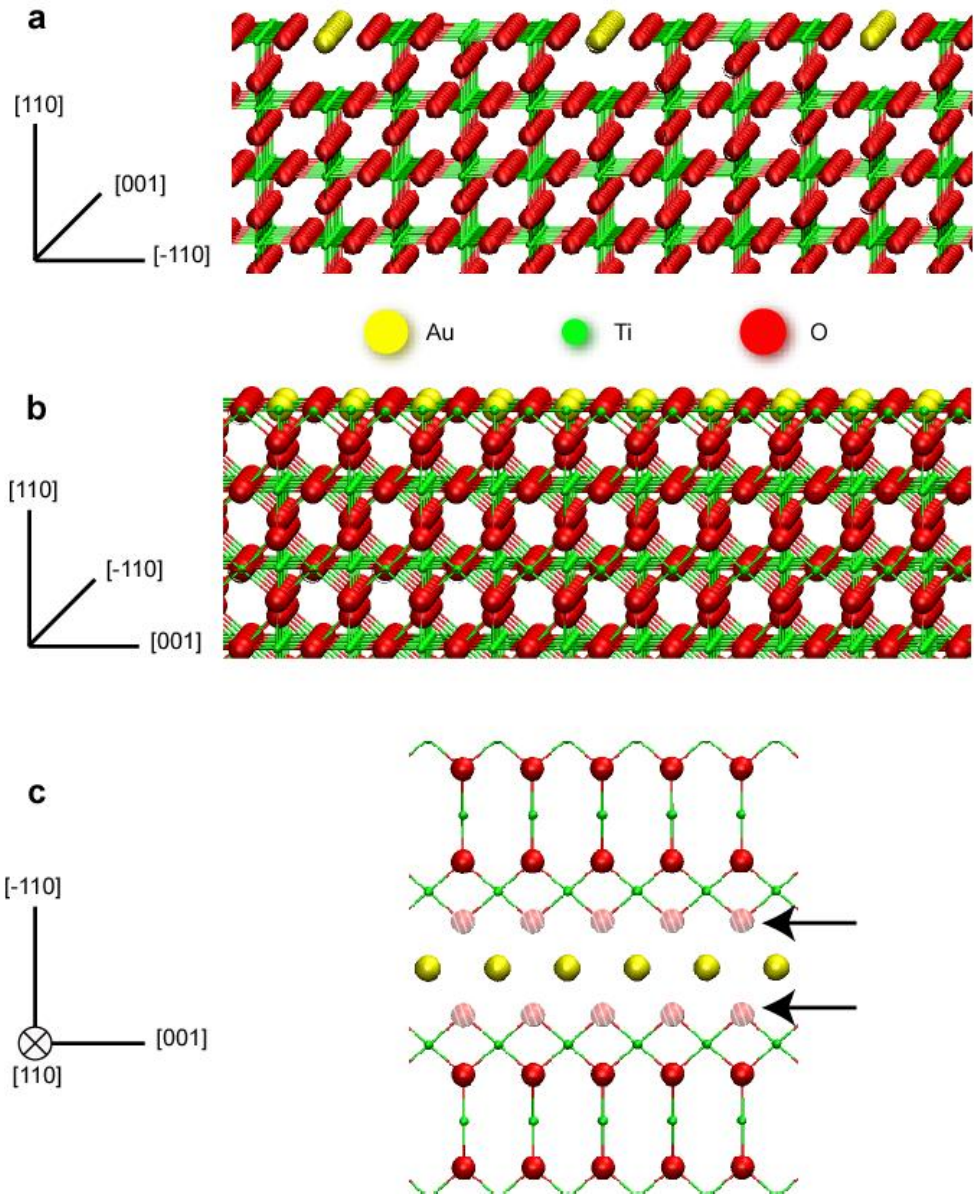

Figure 4.13: Schematic of reconstructed interface of Au[112] and TiO_2 (110) (1x2) viewed along a) TiO_2 [001] b) TiO_2 $[\bar{1}10]$ and c) TiO_2 [110] directions. Au sits in Ti-only columns when observed along TiO_2 $[\bar{1}10]$ direction. The oxygen atoms neighboring Au have been shaded to indicate that they may not be present in the reconstruction.

To verify if our proposed interfacial reconstruction is correct, we created a $Au_{[112]}$ model with the interfacial reconstruction and simulated the projected HAADF scattering potential of our model. Figure 4.14 shows the projected HAADF scattering potential[155] of our proposed

interfacial structure model along the TiO_2 $[1\bar{1}0]$ direction. The potential was convoluted with the simulated electron probe to mimic the Z-contrast of the HAADF-STEM image. The projected potential map does not bring out the strong contrast between the dull Ti-only and bright Ti-O columns since it is not a full STEM image simulation. The strong contrast between the Ti-O and Ti-only columns can come out only in a full STEM simulation. We refer to the results of a full STEM simulation for TiO_2 in the [110] zone axis from other groups which show this effect more clearly.[101] The reference shows that the Ti-only columns are duller than the Ti-O columns, in agreement with our experimental images. We did not do a full STEM simulation for our images since it takes unreasonably long computational times to simulate full multi-slice STEM images for a large non-periodic object like the ones presented in our work. Nevertheless, a full STEM simulation is not needed to pick up the contrast between Au and Ti-O because of the large difference in Z between the elements. Hence the projected potential map is sufficient for our purposes of demonstrating the emergence of periodic bright-dark contrast at the interface and the reduced STEM signal from the interface based on our interface reconstruction model.

The result of the simulation (Figure 4.14) clearly reproduces the alternate bright and dark contrast at the interface similar to the experimental image in Figure 4.6 (a). Further, when we plot the line profile across the simulated image in Figure 4.15, we are also able to reproduce the abrupt drop in STEM intensity at the interface seen in experimental images (Figure 4.10). Since we are able to reproduce all the major features of the interfacial STEM intensity from our model, we believe that the proposed interfacial reconstruction is correct.

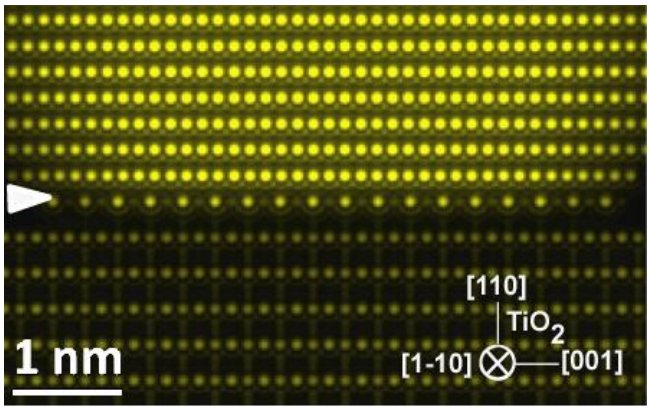

Figure 4.14: Simulated STEM image from a model $Au_{[112]}$ NC with interfacial reconstruction. The arrow points to the interface, showing the same alternating atomic columns as Figure 4.6 (a).

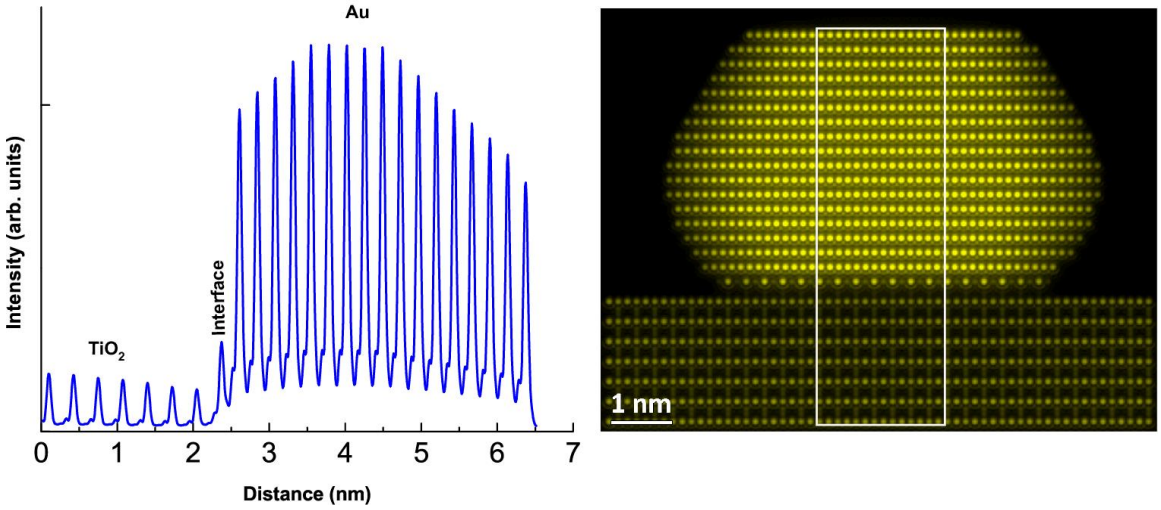

Figure 4.15: Integrated intensity of projected potential across a model $Au_{[112]}$ NC whose interface is reconstructed with Au atoms sitting in the missing Ti rows of a TiO_2 (1x2) reconstruction.

Another important issue is whether the interfacial Au atoms are cationic. To explore this, we performed EELS to characterize the interfacial chemistry. Figure 4.16 (a)-(c) show the integrated Ti $L_{2,3}$ and O K edge intensity together with the electron scattering signal simultaneously recorded by the ADF detector. The ADF signal was used to determine the interface position as indicated by the line in Figure 4.16 (a)-(c). Both Ti $L_{2,3}$ edge (Figure 4.16

(b)) and O K edge (Figure 4.16 (c)) have a strong signal at the interface. However there is also some signal inside the NC. This comes from EELS delocalization. EELS delocalization refers to the presence of EELS signal at a given location from neighboring atomic columns due to electrons scattering to neighboring columns and causing inelastic scattering events in neighboring columns. We anticipate that EELS delocalization is present in our specimen since the specimen thickness is between 30 and 40 nm. We have measured the EELS delocalization for Ti L Edge on our instrument at 200kV to be ~4 Å [156] which is far worse than the imaging resolution of ~ 1 Å achievable in our microscope. Such reduced microanalysis resolution when compared to microscopy resolution is common to STEM-EELS [157]. The presence of Ti and O peaks inside the Au does not imply there is Ti and O inside the Au NC but instead shows that the delocalized EELS signal inside of the Au NC had to come from the interfacial Ti atoms rather than the bulk of TiO_2 since the bulk of TiO_2 is more than 4 Å away from the regions where we see a reasonable Ti signal inside the Au NC.

The EELS fine structure of Ti and O in the interfacial layer is presented in Figure 4.16 4(d) and (e), which compares the fine structure of Ti $L_{2,3}$-Edge and O K-Edge acquired from the interface (red) and from the substrate TiO_2 (blue). The interfacial Ti $L_{2,3}$ edge is consistent with an ionization state between Ti^{3+} and Ti^{4+}, [146] which is a further evidence of neighboring oxygen atoms in our proposed structural model. The four-fold coordination of Au with oxygen in our model is also consistent with the bonding motif of the known Au_2O_3 structure[158].

For the four-fold oxygen coordination in our proposed interfacial reconstruction the dimensions of the unit cell composed of one Au surrounded by four O is 3.97Åx2.95Å. Two O atoms and one Au atom are close packed along the diagonal of this rectangular cell. Since radius of O^{2-} ~ 1.4Å, this gives radius of Au ~1.07 Å, which is much lesser than the metallic radius of

Au(r_{Au0} ~ 1.6Å). For a Au atom to fit in a lattice where the available space is less than its metallic radius, the atom has to either strain the lattice or become smaller by losing some valence electrons. We have experimental evidence from electron micrographs that the interface has the same inter-atomic spacing as the bulk TiO_2. Hence there is no significant strain in the lattice due to Au atoms sitting in the interface. This means that the space constraint had to be accommodated by losing some electrons i.e. by the Au becoming cationic. Based on the space constraints, we estimated above that the radius of a Au atom at the interface to be 1.07Å. Since we know that the radius of Au when it adopts a 3+ state is ~0.85, the Au atoms at the interface must have a larger radius than Au^{3+} but smaller radius than Au^0. Therefore we conclude that the Au atoms have to be cationic with an oxidation state less than three in order to fit into our proposed interfacial reconstruction.

To examine the charge states of Au atoms more quantitatively, we carried out a first-principles calculation (The first principle DFT calculations were done by Min Yu and Dr. Dallas Trinkle in the Materials Science Department at University of Illinois). A plane wave density-functional theory[159-162] calculation of an 8-layer periodic slab of TiO_2 with the (1x2) reconstruction with an added row of 4-fold coordinated Au atoms allows computation of the electronic charge density at the surface, as well as a comparison of the projected electronic density-of-states (DOS) at the surface. The integrated projected DOS for the Au shows a loss of about 1.5e compared to the atomic valence (Figure 4.16 (h)). Moreover, there is a shift in the lowest-lying unoccupied states around the Ti and O ions (Figure 4.16 (f), (g)) at the surface compared with the interior that is consistent with the EELS measurements. Both the bond length consideration and calculations suggest that the four-fold coordinated Au site at the interface between Au and TiO_2 is cationic..

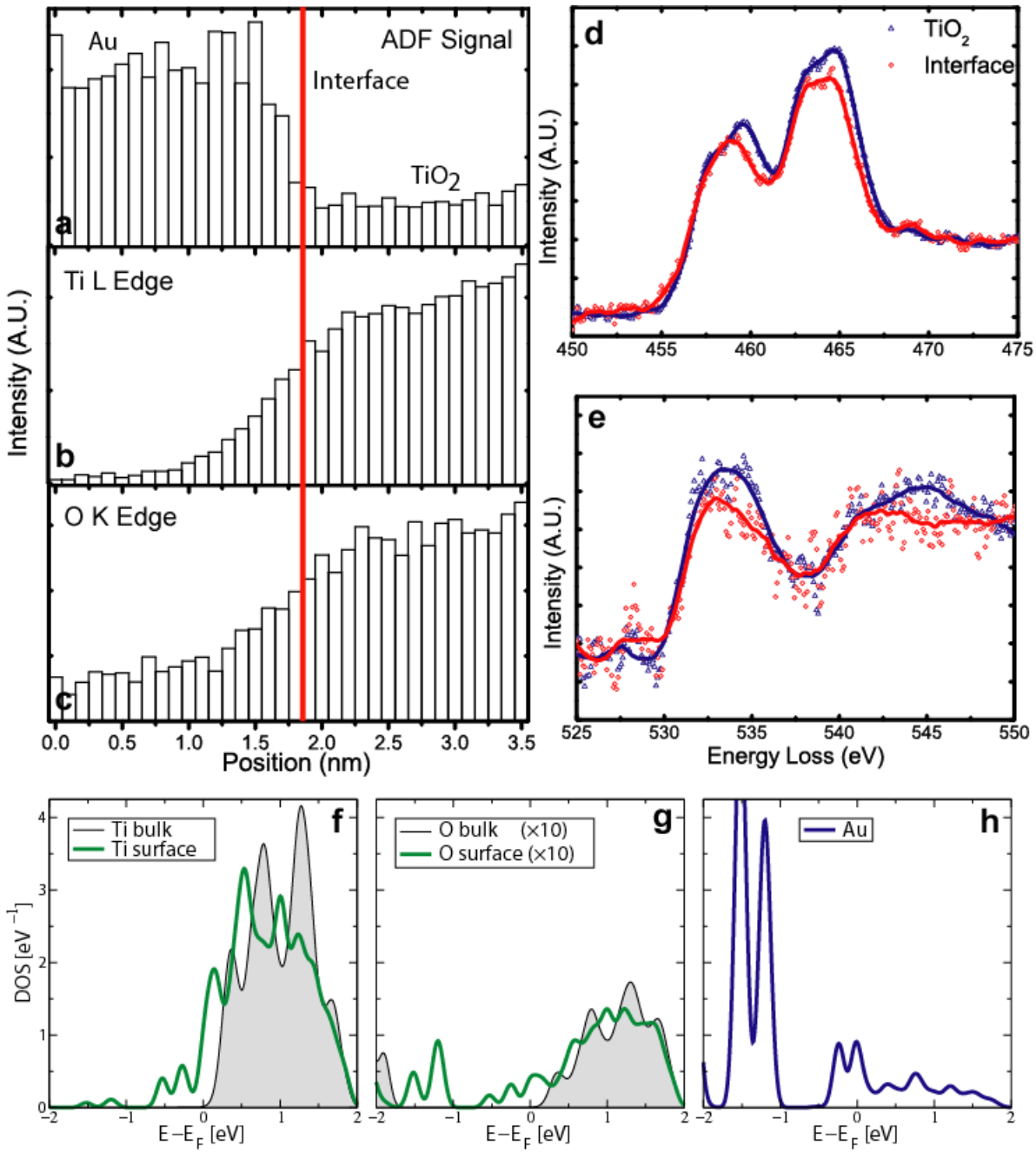

Figure 4.16: (a) Simultaneously acquired (a) ADF intensity, (b) integrated Ti-L Edge intensity and (c) integrated O-K Edge intensity from a line scan across the $Au_{[112]}$ interface. The red line points to the reconstructed interfacial layer with Au, Ti and O atoms. (d) Ti $L_{2,3}$ edge and (e) O K edge obtained from the interface (red) and far away from the interface (blue). The EELS profiles from points between 1.5 – 1.9 nm and 2.2 – 2.4 nm were averaged to obtain the interface and TiO_2 EEL spectra respectively. Projected density of states from (f) Ti, (g) O and (h) Au at the surface of a reconstructed TiO_2(110) (1x2) surface with Au atoms inserted along missing Ti rows. DFT calculations were done by Min Yu and Dr. Dallas Trinkle in the Materials Science department at University of Illinois.

4.5 Interfacial Energy

To see whether the interfacial reconstruction affects NC adhesion, we measured the interfacial energy for $Au_{[112]}$ and $Au_{[110]}$ interfaces by analyzing the equilibrium shape of the NCs. The equilibrium shape of a supported NC is determined by the same principle of minimum free energy as for a free crystal as described in section 4.1, which gives[163] –

$$\frac{\Delta h - h}{h} = \frac{\gamma_{TiO_2} - \gamma_{Int}}{\gamma_{Au}} \tag{4.1}$$

where h is the distance from the center to the top facet, Δh (undercut) is the reduced distance from the center to the bottom facet because of the support, and γ with its subscript refers to the surface and interface energies. The interfacial energy can be determined by examining Δh if the surface energies are known. The dimensions that can be measured directly from experimental images of $Au_{[112]}$ NCs are the total height (2h-Δh) and the width (w). It can be shown that for $Au_{[112]}$ NCs with the equilibrium shape $h = w/\sqrt{6}$.

It is seen from Figure 4.17 that

$$h_{111} = \left(\frac{w}{2}\right)\cos(\alpha) \tag{4.2}$$

where,

$$\cos(\alpha) = \frac{[1\,\bar{1}\,\bar{1}]\bullet[1\,\bar{1}\,0]}{\left|1\,\bar{1}\,\bar{1}\right|\left|1\,\bar{1}\,0\right|} = \frac{\sqrt{2}}{\sqrt{3}} \tag{4.3}$$

Hence,

$$h_{111} = \left(\frac{w}{2}\right) * \frac{\sqrt{2}}{\sqrt{3}} = \frac{w}{\sqrt{6}} \tag{4.4}$$

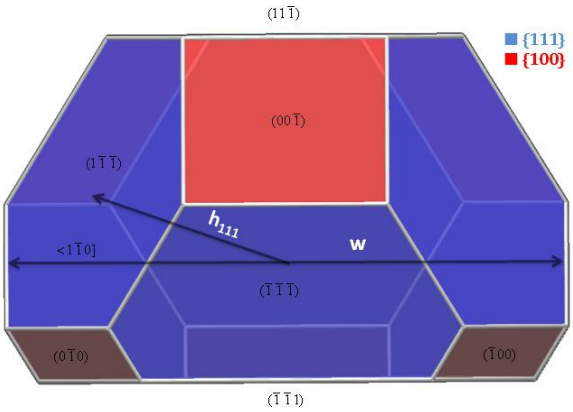

Figure 4.17: Schematic of the ES of a supported $Au_{[112]}$ NC viewed from the [112] zone axis. The blue facets are {111} and the red facets are {100}. w is the width of the NC and h_{111} is the distance from the center of the unsupported NC to the center of any 111 facet.

For $Au_{[110]}$ NCs, center to top distance (h), total height (2h-Δh) and width (w) were obtained directly from the image. For measuring NC dimensions we calibrated the images using FFT spots of Au $(11\ \bar{1})$ or TiO_2(110). The error in measuring the peak to peak separation of FFT spots was taken to be 2 pixels. The total height (2h-Δh) was measured from line profiles averaged over the width of the NC. The error in measuring the peak to peak separation of Au (111) rows was 2 pixels. Experimentally, we observed that beam induced roughness can lead to additional incomplete Au layers appearing at top surface, which was taken into account in our measurement. The width was measured from line profiles averaged over the widest Au (111) planes. The error in measuring the peak to peak separation of Au (111) rows was taken to be $2*d_{Au(220)}$ based on the roughness of side edges.

The interfacial energy was calculated by using $\gamma_{Au(111)}$ = 1.283 J/m^2 following Vitos et al[66] and $\gamma_{TiO2(110)}$ = 0.33 J/m^2 following Cosandey et al[63]. The average interfacial energy of Au[112] NCs was measured to be 0.67±0.1 J/m^2 from 23 $Au_{[112]}$ NCs. Similarly, we measured the interfacial energy of $Au_{[110]}$ NCs to be 1.12±0.17 J/m^2 using γAu(100) = 1.627 J/m^2 [66] from 3 Au[110] NCs that we observed.

There is a difference of 0.45 J/m^2 in interfacial energy between $Au_{[112]}$ and $Au_{[110]}$ NCs. The interfacial energy difference somewhat depends on the surface energies of Au that we used. Even in the case, when the ratio of $\gamma_{Au(100)}/\gamma_{Au(111)}$ is reduced to 1.05, $\gamma_{Au(100)/TiO2(110)}$ drops only to 0.99 ± 0.14 J/m^2. The $\gamma_{Au(100)/TiO2(110)}$ is still higher than $\gamma_{Au(111)/TiO2(110)}$ by ~0.3 J/m^2. Thus, the interfacial reconstruction in $Au_{[112]}$ NCs leads to a significantly reduced interfacial energy of $Au_{[112]}$ NCs. Indeed, the reduced interfacial energy of the $Au_{[112]}$ NCs is reflected by their abundance among observed nanocrystals after extended annealing (>2 hours).

CHAPTER 5

MEASUREMENT OF LINE TENSION OF EPITAXIAL GOLD NANOCRYSTALS SUPPORTED ON TITANIUM DIOXIDE (110)

Atoms at the intersection of three phases have an additional free energy compared to interfacial atoms between two phases. This energy normalized by length is referred to as a line tension (LT) at the three phase boundary. The LT competes with surface/interface energies and ultimately determines the morphology of interfaces. For examples, LT of lipid membrane stabilizes a range of membrane structures and their associated mechanic properties [164-166] and in vapor-solid-liquid catalytic growth of nanowires LT determines the preferred growth diameter.[167] For solids, where the surface energy is typically two orders of magnitude larger than liquids, LT becomes important only when the interfacial dimension reaches the scale of several nanometers (nm). Experimental measurements of LT in solids are therefore extremely difficult. Consequently, LT has been mostly ignored in the study of solid-solid interfaces. This approximation leaves large gaps in thermodynamic predictions of nanocrystal properties precisely where they matter most, for example, in the early stage of nanocrystal formation and in supported catalyst particles of a few nanometers in size. Here we report the first experimental measurements of interfacial LT of supported nanocrystals by investigating epitaxial Au nanocrystals supported on rutile (TiO_2). Studying nanocrystals of the same epitaxy allows us to separate interfacial energy from interfacial LT. The study was enabled by aberration corrected electron microscopy; the significantly improved image resolution allows us to determine the shape of NCs in the cross-sectional geometry with accuracy of a single atomic layer. By examining Au nanocrystals less than 12nm in size, we measured the interfacial LT to be

0.85±0.24 eV/Å (1.36±0.38 x 10^{-9} N) and interfacial energy to be 0.61±0.06 J/m^2 (assuming $\gamma_{TiO2(110)}$ = 0.33 J/m^2 and $\gamma_{Au(111)}$ = 1.283 J/m^2) for NCs with the epitaxial relationship $Au(111)_{[-110]} \parallel TiO_2(110)_{[001]}$. The effects of surface energy and strain relaxation on NC shape are discussed.

5.1 Introduction

Line tension (LT) is defined as the free energy required to increase the interfacial circumference by a unit length. LT arises since atoms at a three phase line have a different energy than atoms at a two phase interface. Line tension (LT) was first conceptually described by Gibbs. Later, Boruvka and Neumann[168] generalized the Young's equation for the contact angle of a liquid droplet on a solid surface by incorporating LT as –

$$\cos(\theta) = \frac{\gamma_{SV} - \gamma_{SL}}{\gamma_{LV}} - \frac{\tau}{\gamma_{LV} r} \tag{5.1}$$

where, θ is the contact angle of the droplet, γ_{SV}, γ_{LV} are surface energies of solid substrate and liquid droplet, γ_{SL} is interfacial energy, r is radius of the droplet and τ is interfacial line tension. In liquid droplets, LT becomes important in determining the wetting angle (θ) when the LT term in equation (5.1) becomes significant, i.e. as r reduces to the order of the characteristic length = τ/γ. From equation (5.1), it is clear that LT (τ) can be extracted from plots of cos(θ) versus 1/r if all the other thermodynamic parameters are constant. Using this approach, LT has been measured in several liquids[169-171]. Theoretical estimates of LTs of liquid droplets is on the order 10^{-10} N while experimental values range from 10^{-6} to 10^{-9} N.[171] For non-metallic liquids with typical values of γ_{LV} = 10^{-2} J/m^2 and LT = 10^{-9} N, the effect of LT on droplet shape can be seen below 100nm. In comparison to liquids, the surface energies of metallic solids are about

two orders of magnitude larger. Thus for similar values of LT, the characteristic length of metallic solids is two orders of magnitude smaller, thus making it more difficult to experimentally observe the effect of LT on the shape of supported metallic nanocrystals (NCs). Measurements of LT in supported metallic NCs are also complicated by the fact that the NC shape and interfacial energy change with the NC orientation. Measurements of LT are meaningful only for NCs having the same orientation relationship with the support. Further, one has to be careful to avoid the effect of surface inhomogeneties that create a 'pseudo-line tension' effect.[172, 173] To the best of our knowledge interfacial line tension has not been reported before for supported metallic NCs.

The prime issue with measuring the shapes of small (<10nm) metallic NCs is the experimental difficulty in imaging the interface, facets and ES to high accuracy. Measurements of ES of NCs have been previously reported using multiple experimental techniques including Transmission Electron Microscopy (TEM),[63, 133] Scanning Electron Microscopy (SEM), [133, 134] Scanning Probe Microscopy (SPM),[135-138] Grazing Incidence Small Angle X-Ray Scattering[174] etc. Among these techniques, TEM and SPM are capable of measuring individual shapes of sub-10nm NCs. Cross sectional TEM is potentially useful for smaller NCs (<10nm), but conventional cross sectional sample preparation methods leads to modifications of the surface atomic structure of smaller NCs. SPM has been successful in determining the shapes of small 2-D metal islands [136-138] but generally has difficulties with shape measurements of 3-D metallic NCs that are less than 10nm.[97, 105, 140-144] Therefore, a more direct method is sought to address the issue of measuring ES of small 3-D metallic NCs.

In this study, we have analyzed the equilibrium shape (ES) of epitaxial Au NCs supported on TiO_2 (110) in an aberration corrected Scanning Transmission Electron Microscope

(ac-STEM). The NCs are prepared after the oxide support has been thinned to electron transparency to avoid damaging the NCs during sample preparation. The NC images were formed in the so-called Z-contrast mode by collecting high angle scattered electrons using a High-Angular Annular Dark Field (HAADF) detector; the Z-contrast in HAADF-STEM resulted in straightforward image interpretation and shape measurement (in contrast to complicated phase contrast in TEM images). The ~1Å resolution of our ac-STEM[175] allowed us to measure the shapes of NCs to a single atomic layer accuracy. All the Au NCs used in this work had the same epitaxial arrangement ($Au(111)_{[-110]} \parallel TiO_2(110)_{[001]}$) which has been reported before.[69, 70]

Using shape measurements from ac-STEM images of epitaxial Au NCs in the size range 4 to 11 nm, we show that smaller Au NCs are more dewet from the support than larger NCs. We attribute the dewetting to the enhanced effect of LT at smaller NC sizes. In order to measure LT from ES of NCs, we have modified the Wulff-Kaishew equation.[127, 131] By fitting the experimentally observed shapes from ac-STEM images to the modified Wulff-Kaishew equation, we were able to measure the interfacial LT of epitaxial Au NCs.

5.2 Results

5.2.1 Nanocrystal Epitaxy and Equilibrium Shape

The STEM image in Figure 5.1 represents a typical epitaxial Au NCs observed on TiO_2 (110). The Au NC in Figure 5.1 with a hemispherical shape is oriented along the Au [112] zone axis. In this orientation, the Au atoms are arranged in a rectangular lattice defined by the basis lattice vectors of $Au[11\bar{1}]$ and $Au[1\bar{1}0]$. The epitaxy in Figure 5.1 can be described as $Au(111)_{[-110]} \parallel TiO_2(110)_{[001]}$. This was the most common type of epitaxy that we observed. This

epitaxy has also been reported earlier by vacuum deposition and annealing[102] as well by precipitation and calcination[69].

In order to determine the shape of the NCs, we examined atomic resolution contrast of the epitaxial NCs recorded by HAADF-STEM. The nanocrystals were imaged along the TiO_2 $[\bar{1}10]$ direction. The atomic columns of Au are clearly resolved in Figure 5.1. The Au atomic columns appear bright and the Ti atomic columns appear much duller due to the Z-contrast. Superimposed on the experimental image in Figure 5.1 is the estimated equilibrium (Wulff) shape. The parameters used for modeling are the ratio of distances to the {100} and {111} facets, corresponding to the ratio of the surface energies of {100} and {111}, or $\gamma_{100}/\gamma_{111}$. For the Au NC shown in Figure 5.1, the fit was obtained with $\gamma_{100}/\gamma_{111} = 1.06$. There is noticeable edge roughness at the top and side surfaces in this case. The edge roughness is expected from surface step fluctuations at finite temperatures.[135] Because of this, the nanocrystal facets are not obvious in the HAADF-STEM image. Thus, we performed modeling and simulations of image contrast to establish the faceting of Au NCs.

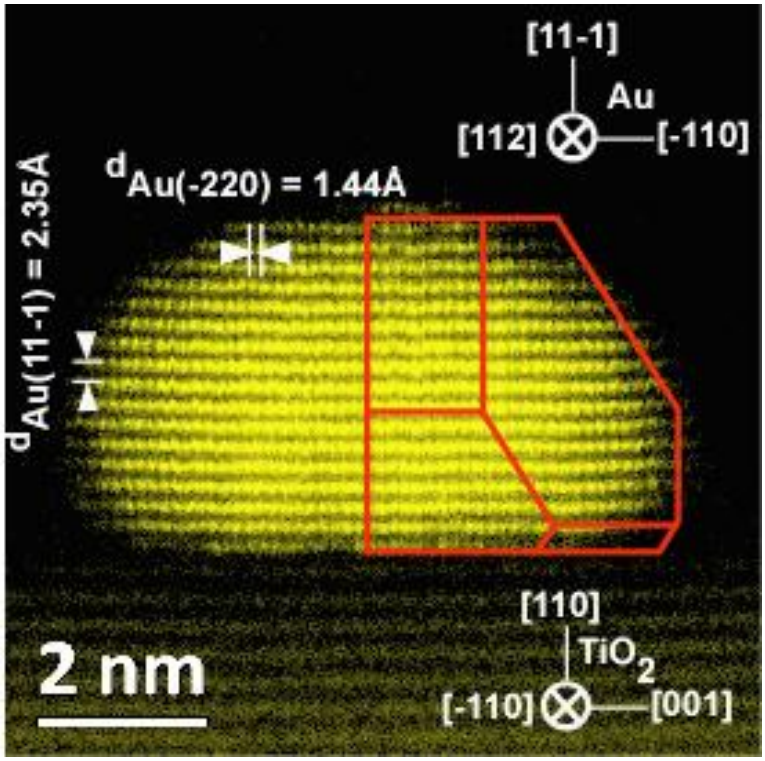

Figure 5.1: High resolution STEM image of epitaxial Au NC with the epitaxial relationship $Au(111)_{[-110]} \parallel TiO_2(110)_{[001]}$. The best fit Wulff shape has been overlaid on one half of the NC.

Figure 5.2(b) shows a line profile along the width direction of a (dia = 4.3nm) Au NC shown in Figure 5.2(a). The solid blue curve shows the experimental line profile from the region marked by the box in Figure 5.2(a). The dashed green curve shows the simulated STEM line profile from a similar region in a model NC, whose dimensions were identical to the NC in Figure 5.2(a). It can be seen from Figure 5.2(b) that the change in the slope of the experimental line profile is well reproduced by the simulated line profile. Thus we concluded that Au NCs are faceted and close to the ES, with additional corner and edge roughness, as expected from the contribution of entropy to the free energy.[135] As a side note, we observed that the Wulff shape fit for NC shape always gave surface energy ratios less than the theoretical value of $\gamma_{100} / \gamma_{111}$ =1.268 .[66]

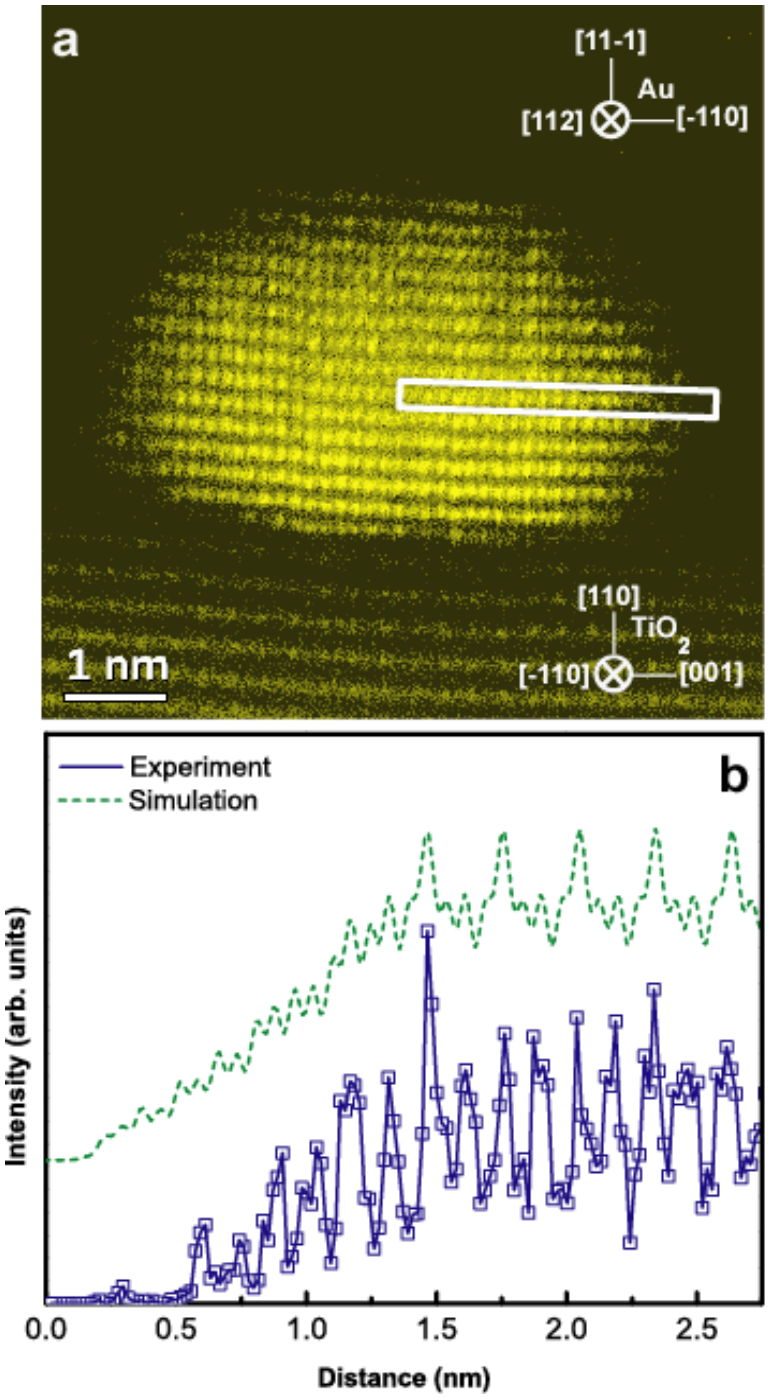

Figure 5.2: (a) Atomic resolution HAADF-STEM image of smaller Au NC. (b) Experimental (solid, blue) and simulated (dashed, green) horizontal line profiles from the Au NC in (a). The simulation used a crystal shape model with the same size as the NC in (a) and multiple scattering as implemented by the multislice method.

The Au NCs were faceted at all sizes (Figure 5.3(a) and (b)) which is consistent with earlier reports that larger Au NCs are dewet and faceted at equilibrium[63, 154] but inconsistent with reports that equilibrium shapes of smaller Au NCs is spherical.[63, 102] We suspect that edges of smaller NCs became rounded during cross sectional TEM sample preparation in prior work[63].

5.2.2 Size Dependence of NC Shapes

Figure 5.3(c) is a 3D model of a typical Au NC. The well-defined NC shapes allow us to extract NC dimensions from experimental images as shown in Figure 5.3(d), which is a schematic illustration of measurements from a typical Au NC. The dimensions that can be extracted with confidence are the total height (2h-Δh) and the width (w). These dimensions have been identified in Figure 5.3(d). It can be shown (Appendix B) that for Au NCs, the center to top surface distance (h) = w/√6. The undercut for Au NCs then can be measured using Δh = 2*(w/√6) – (2h- Δh).

Using the shape information in STEM images of Au NCs, we measured Δh/h for a number of NCs. Figure 5.4(a) plots Δh/h versus NC width from 42 Au NCs. Since the data has outliers, we performed leave-one-out cross validation to see if the data was better fit by a linear curve or a horizontal line. The cross validation score (CVS) was computed for each case as –

$$CVS = \frac{\sum_{j=1}^{42} \left(\frac{f(x_j, \theta) - y_j}{y_{error}} \right)^2}{42}$$

where $f(x_j,\theta)$ is computed by fitting all the data points except (x_j,yj) to the curve of choice. Using leave-one-out cross validation, we got a CVS of 2.976 for a linear fit and a CVS of

3.813 for a horizontal line fit, which shows that the data is better predicted by a linear curve. Thus we used a direct-weighted linear fit for the data which is shown by the dashed red line in Figure 5.4(a). The weighted linear fit to the data (dashed red line) shows Δh/h by drops by ~0.14 over 7nm. In other words, smaller epitaxial Au NCs are more dewet than larger epitaxial Au NCs. Indeed, the dewetting of smaller Au NCs is also obvious upon comparing Figure 5.3(a) and (b). The error bars in Figure 5.4(a) are conservative estimates based on the largest possible measurement error as explained in detail below.

a) Error in calibration: Distances in images were calibrated using FFT spots of Au($11\bar{1}$) or TiO_2($\bar{1}10$). The error in measuring the distance between Au($11\bar{1}$) and Au($\bar{1}\bar{1}1$) spots was taken to be 2 pixels. In real space units this corresponds to a half error up to 0.1 nm depending upon image magnification and NC size.

b) Error in measuring total height (H = 2h - Δh): We noticed that the electron beam induced roughening could result in partially formed, additional, Au layers at the top surface. For some Au NCs, the beam-induced layer was easily discernable where the layer was only half, or less, formed or was much duller in contrast than the Au layer immediately below. In such cases, we did not include the beam induced layer while measuring the total height.

   But for other cases, where the top layer was more than half formed, but much duller in contrast than the layer adjacent to it, it was difficult to decide whether the top layer was beam induced. For such NCs, we assumed that the top layer was beam induced but to account for the uncertainty, an extra layer being present in the NC is included in the error bar.

   Additionally, the error in measuring the peak to peak separation of Au ($11\bar{1}$) rows was taken to be 2 pixels (corresponding to a half error of 0.02 – 0.05 nm depending upon image magnification and NC size).

c) Error in measuring width (W): The error in measuring width was taken to be $2d_{Au(220)}$ because of the roughness of the side edges. The error in measuring the peak to peak separation of Au ($2\bar{2}0$) rows was taken to be 2 pixels (corresponding to a half error of 0.03 – 0.1 nm depending upon image magnification and NC size).

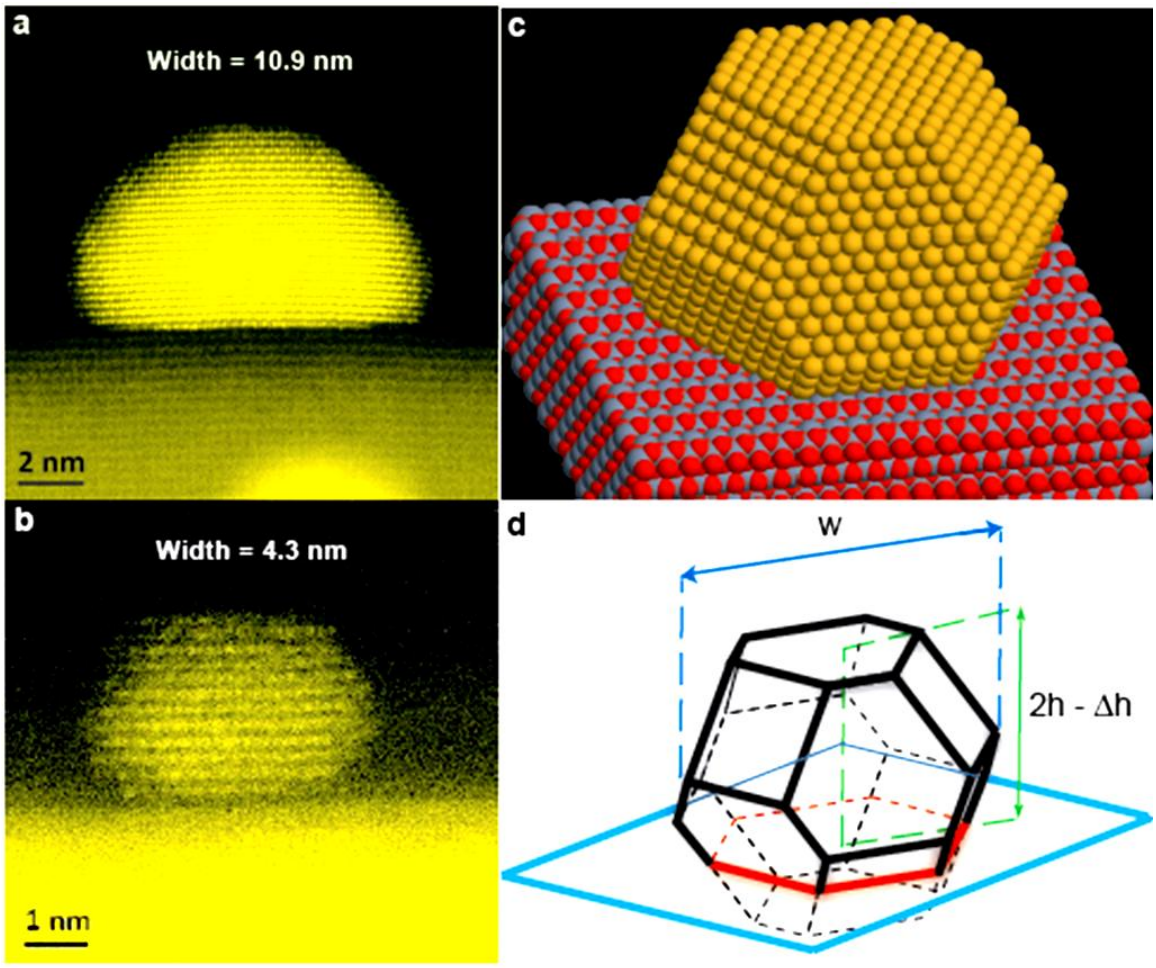

Figure 5.3: (a) 10.9 nm Au NC, (b) 4.3 nm Au NC, (c) Model of Au NC and (d) Schematic of Au NC shape showing measurements of NC dimesions.

5.2.3 Measurement of Line Tension of Epitaxial Au NCs

The ES of a supported NC is related to the surface and interfacial energies by the Wulff-Kaishew[127, 131] principle which gives –

$$\frac{\Delta h - h}{h} = \frac{\gamma_{TiO_2} - \gamma_{Int}}{\gamma_{Au}} \tag{5.2}$$

where γ with its subscript refers to the surface and interface energies. By taking into account the interfacial line tension (τ_{Int}) for supported NCs, the Wulff-Kaishew principle can be modified as –

$$\frac{\Delta h - h}{h} = \frac{\gamma_{TiO_2} - \gamma_{Int}}{\gamma_{Au}} - \frac{\tau_{Int}}{\gamma_{Au}} \frac{dl_{Int}}{dA_{Int}} \tag{5.3}$$

where A_{Int} and l_{Int} are the interfacial area and interfacial perimeter respectively (derived in next section). This expression for ES of solid NCs with LT is fundamentally similar to the effect of LT on liquid droplets[168] except for the 'geometric factor' of dl_{Int}/dA_{Int} , which depends on the shape of the interface. The geometric factor in (5.3) can be rewritten in terms of measurable quantities as (derived in next section) –

$$\left(\frac{dl_{Int}}{dA_{Int}} \right)_{112} = \frac{2}{\sqrt{3} a_{Int}} = \frac{2}{\sqrt{3}(w + \frac{2\Delta h}{\tan\theta})} \tag{5.4}$$

where tan(θ)=1.633.

By measuring NC dimensions as well as expressing the geometric factor in terms of measurable NC dimensions, all terms except LT are known in equation(5.3). Therefore by plotting appropriately we can extract LT. Figure 4(b) shows a plot of "(Δh-h)/h" versus "$1/a_{Int}$" for Au , where a_{Int} is defined in equation (5.31). Since the data has outliers, we performed leave-one-out cross validation to see if the data was better fit by a linear curve or a horizontal line. We obtained a CVS of 2.764 for a linear fit and a CVS of 3.813 for a horizontal line fit, which shows

that the data is better predicted by a linear curve. From the slope of a direct-weighted linear fit to Figure 5.4(b), LT was measured to be 0.85±0.24 eV/Å (1.36±0.38 x 10^{-9} N). The value of LT depends on the value of γ_{Au}. We used $\gamma_{Au(111)}$ = 1.283 J/m^2 following Vitos et al[66]. The error bar in our measurements is about 24 percent which is higher than LT measurements of liquid droplets. The reason for this larger error stems from the fact that LT in different Au NCs is equal only to an approximation since the details of atomic bonding at the boundary of interfaces cannot be universally self similar among NCs of various sizes. Further, incomplete equilibrium shape formation as well as beam induced shape change in some NC could contribute to some error.

We were also able to measure interfacial energy from intercept of the plot in Figure 5.4(b) as $\gamma_{Au(111)/TiO2(110)}$ = 0.61±0.06 J/m^2. The value of interfacial energy depends on the values of γ_{Au} and $\gamma_{TiO2(110)}$. We used $\gamma_{Au(111)}$ = 1.283 J/m^2 as mentioned above and $\gamma_{TiO2(110)}$ = 0.33 J/m^2 following Cosandey et al[63]. We compared our measurements to prior work using the same $\gamma_{Au(111)}$, $\gamma_{TiO2(110)}$ and found that the reported value of $\gamma_{Au(111)/TiO2(110)}$ from a 200nm Au NC prepared on TiO_2 (110) in vacuum[63] was larger by ~0.52 J/m^2. Other reports of interfacial energies of Au NCs on TiO_2 (110) do not consider equilibrium shaped NCs[95, 102] and therefore not suitable for comparison.

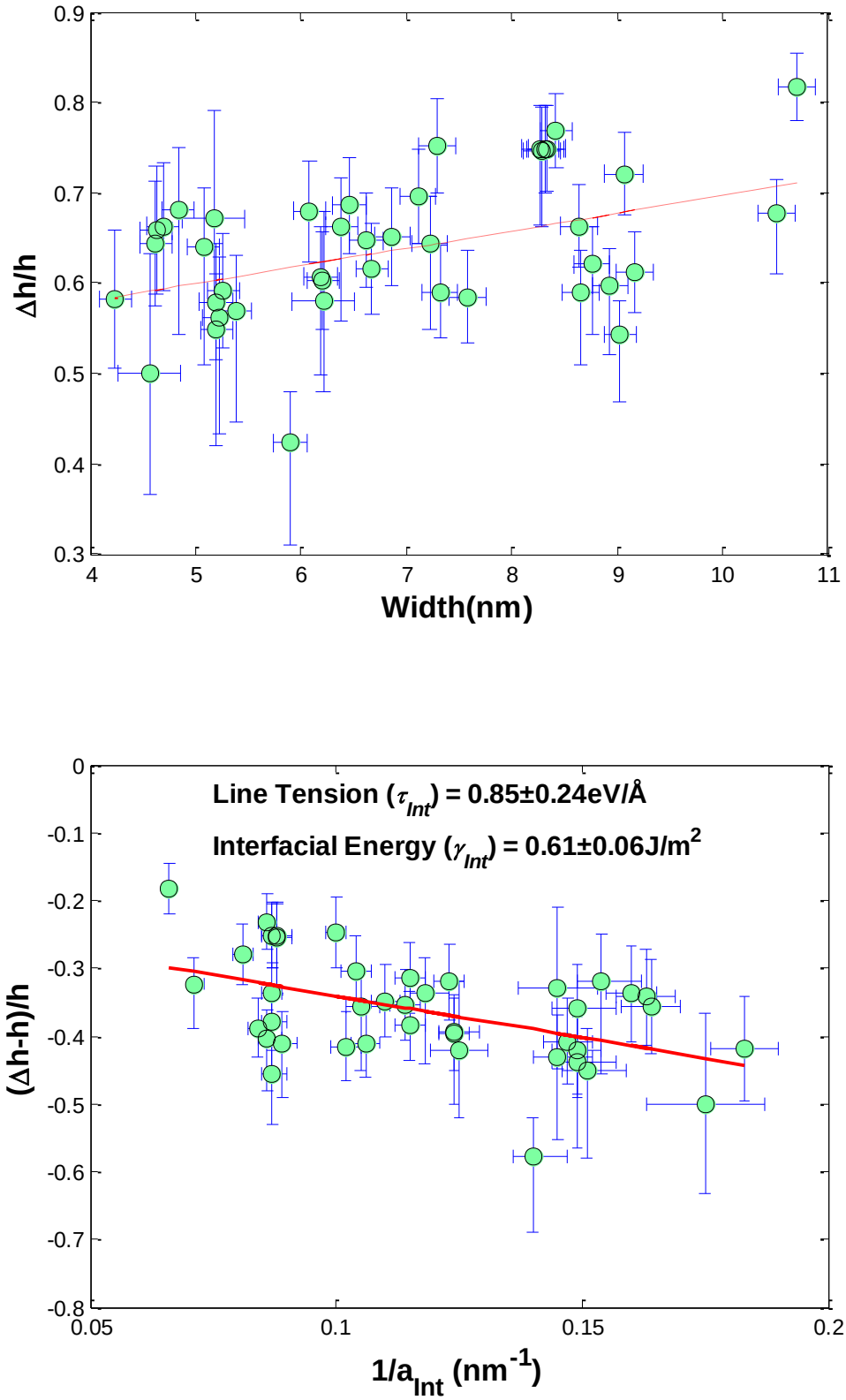

Figure 5.4: (a) Plot of Δh/h versus NC width for Au NCs in the size range of 4 – 11 nm, (b) Plot of (dh-h)/h versus $1/a_{Int}$ where a_{Int} has been defined in equation (5.31). LT and interfacial energy have ben measured from the slope and intercept respectively.

5.2.4 Modified Wulff-Kaishew Theorem

Following Kern et al.,[132] interfacial LT can be incorporated into the expression for excess free energy of assembling a supported and unstrained NC from n atoms as –

$$\Delta G(n) = -n\Delta\mu + \sum_{j \neq Int} \gamma_j A_j + (\gamma_{Int} - \gamma_{TiO_2}) A_{Int} + \tau_{Int} l_{Int} \tag{5.5}$$

where ΔG and $\Delta\mu$ are the excess free energy and chemical potential difference between a Au atom in the gas phase and a Au atom in the NC respectively, n is the number of atoms in the NC, γ_j is the surface energy of free Au NC surfaces, γ_{Int} is the interfacial energy and τ_{Int} is the interfacial LT. Equation (5.5) ignores the effect of misfit strain in assembling the NC on a support. It has been suggested that the contribution to the free energy of the NC from misfit strain can be modeled as a fraction of the uniform strain energy ($\lambda E \varepsilon^2 V$),[176] where E is a combination of the elastic coefficients of the NC and the support, ε is the strain close to the interface from lattice misfit and V is the volume of the NC and λ is a parameter that accounts for strain relaxation. The linearity of H vs W (Figure 5.5) suggests that the strain relaxation is self-similar for all the Au NCs we have observed. Hence, we approximate λ to be a constant for the NCs we studied. Now, the total excess free energy of a Au NC can be rewritten by including the strain energy as –

$$\Delta G(n) = -n\Delta\mu + \sum_{j \neq Int} \gamma_j A_j + (\gamma_{Int} - \gamma_{TiO_2}) A_{Int} + \tau_{Int} l_{Int} + \lambda E \varepsilon^2 V \tag{5.6}$$

where λ is a parameter that comes from strain relaxation and is approximated to not change with NC size. Noting that,

$$V = n\nu \tag{5.7}$$

where V is the volume of the NC and ν is the atomic volume, and

$$V = \frac{1}{2}\left(\sum_{j \neq Int} h_j A_j + (h - \Delta h) A_{Int} \right) \tag{5.8}$$

where h is the distance from the center to the top facet, Δh (undercut) is the difference in the distance between the center to the bottom facet of an unsupported cluster and the center to bottom facet of the supported cluster, the derivative of ΔG can be written as –

$$d\Delta G(n) = \frac{\left(\lambda E \varepsilon^2 - \Delta\mu\right)}{2\nu}\left(\sum_{j \neq Int} h_j A_j + (h - \Delta h) A_{Int} \right) + \sum_{j \neq Int} \gamma_j dA_j + (\gamma_{Int} - \gamma_{TiO_2}) dA_{Int} + \tau_{Int} dl_{Int} \tag{5.9}$$

Using the partial equilibria conditions,

$$\left(\frac{\partial \Delta G}{\partial A_{Int}} \right)_{A_j,\ldots,T,\Delta\mu} = 0 \tag{5.10}$$

$$\left(\frac{\partial \Delta G}{\partial A_j} \right)_{A_i,\ldots,A_{Int},T,\Delta\mu} = 0 \tag{5.11}$$

we get,

$$\frac{\gamma_{Int} - \gamma_{TiO_2} + \tau_{Int} \dfrac{dl_{Int}}{dA_{Int}}}{h - \Delta h} = \frac{\Delta\mu - \lambda E \varepsilon^2}{2\nu} \tag{5.12}$$

$$\frac{\gamma_{Au}}{h} = \frac{\Delta\mu - \lambda E \varepsilon^2}{2\nu} \tag{5.13}$$

where γ_{Au} is the surface energy of the Au NC facet parallel to the interface. Combining equations (5.12) and (5.13) we get,

$$\frac{\Delta h - h}{h} = \frac{\gamma_{TiO_2} - \gamma_{Int}}{\gamma_{Au}} - \frac{\tau_{Int}}{\gamma_{Au}} \frac{dl_{Int}}{dA_{Int}} \tag{5.14}$$

In order to express the geometric factor in terms of measurable dimensions we first examine the shape of a Au (111) facet as shown in Figure 5.6 (a). The blue regions are {111} type facets and the red regions are {100} type facets. This color scheme will be followed throughout.

As long as the reentrant {100} facets exist at the interface (which is the case in all the NCs that we analyzed), the shape of the interface will be similar to the (111) surface facets. The dimensions a,x,w_{top} of the surface facets will be referred as a_{int}, x_{int} and w_{int} respectively for the interfacial (111) facet. The circumference and the area of the interface will then be given by:

$$l_{Int} = 3(a_{Int} - x_{Int}) \tag{5.15}$$

$$A_{Int} = \sqrt{\frac{3}{4}}(a_{Int}^2 - x_{Int}^2) \tag{5.16}$$

x_{int} does not change with a marginal increase in the interfacial area (corresponding to an increasing undercut). Thus,

$$dl_{Int} = 3(da_{Int}) \tag{5.17}$$

$$dA_{Int} = \sqrt{\frac{3}{2}}a(da_{Int}) \tag{5.18}$$

Therefore the geometric factor can be expressed as –

$$\frac{dl_{Int}}{dA_{Int}} = \frac{2}{\sqrt{3}a_{Int}} \tag{5.19}$$

Since a_{int} is not experimentally measurable, we wish to express a_{int} in terms of experimentally measurable quantities. By considering the Au NC in the [112] zone axis we can see that (Figure 5.6 (b))

$$\frac{a - 2x}{a_{Int} - 2x_{Int}} = \frac{z}{z + \Delta h} \tag{5.20}$$

$$z = \frac{a - 2x}{2} \tan\theta \tag{5.21}$$

Substituting for z in equation (5.20) and simplifying we get,

$$a_{Int} - 2x_{Int} = a - 2x + \frac{2\Delta h}{\tan\theta} \tag{5.22}$$

Since $x = x_{Int}$, equation (5.22) simplifies to

$$a_{Int} = a + \frac{2\Delta h}{\tan\theta} \tag{5.23}$$

where $\tan(\theta) = 1.633$ (from geometrical considerations).

In the above expression (5.23) for a_{Int}, 'a' is not a measurable quantity. Hence, in order to express 'a' in terms of measurable quantities, we consider the Au NC in the [110] zone axis (Figure 5.6 (c)).

From Figure 5.6 (c), we see that

$$\frac{AO}{h_{111}} = \tan\phi \tag{5.24}$$

where $\tan(\varphi)=\sqrt{2}$.

Since,

$$AO = \frac{2}{3}\left(\frac{\sqrt{3}}{2}a\right) = \frac{a}{\sqrt{3}} \tag{5.25}$$

We get,

$$a = \sqrt{6}h_{111} \tag{5.26}$$

It is seen from Figure 5.6 (d) that –

$$h_{111} = \left(\frac{w}{2}\right)\cos(\alpha) \tag{5.27}$$

where,

$$\cos(\alpha) = \frac{[1\,\bar{1}\,\bar{1}]\bullet[1\,\bar{1}\,0]}{\left|1\,\bar{1}\,\bar{1}\right|\left|1\,\bar{1}\,0\right|} = \frac{\sqrt{2}}{\sqrt{3}} \tag{5.28}$$

Hence,

$$h_{111} = \left(\frac{w}{2}\right) * \frac{\sqrt{2}}{\sqrt{3}} = \frac{w}{\sqrt{6}} \tag{5.29}$$

Thus –

$$w = \sqrt{6}h_{111} \tag{5.30}$$

where ‘w’ is the width of NC as seen in the [112] zone axis.

Hence equation (5.23) simplifies to

$$a_{Int} = w + \frac{2\Delta h}{\tan\theta} \tag{5.31}$$

Thus,

$$\left(\frac{dl_{Int}}{dA_{Int}}\right)_{112} = \frac{2}{\sqrt{3}a_{Int}} = \frac{2}{\sqrt{3}(w + \frac{2\Delta h}{\tan\theta})} \tag{5.32}$$

In the above analysis, all Au NCs are assumed to be dewet from the TiO_2 substrate which is consistent with our experimental observations. We note that for even larger Au NCs, where the reentrant facets might disappear at the interface, the above analysis has to be modified.

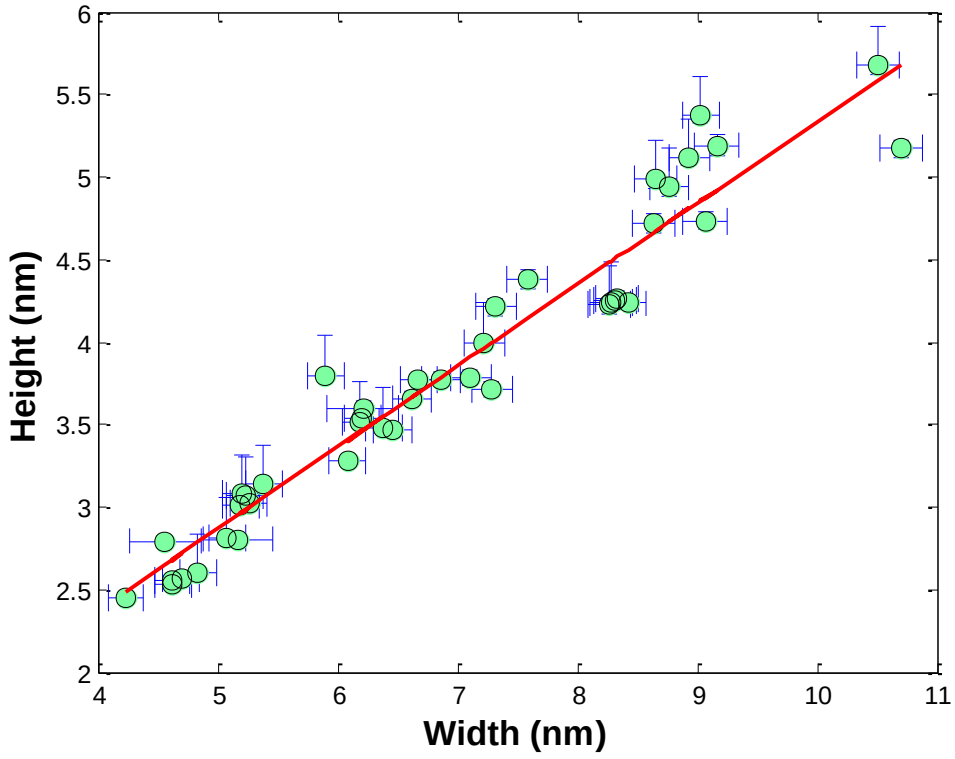

Figure 5.5: Plot of NC height vs NC width for Au NCs.

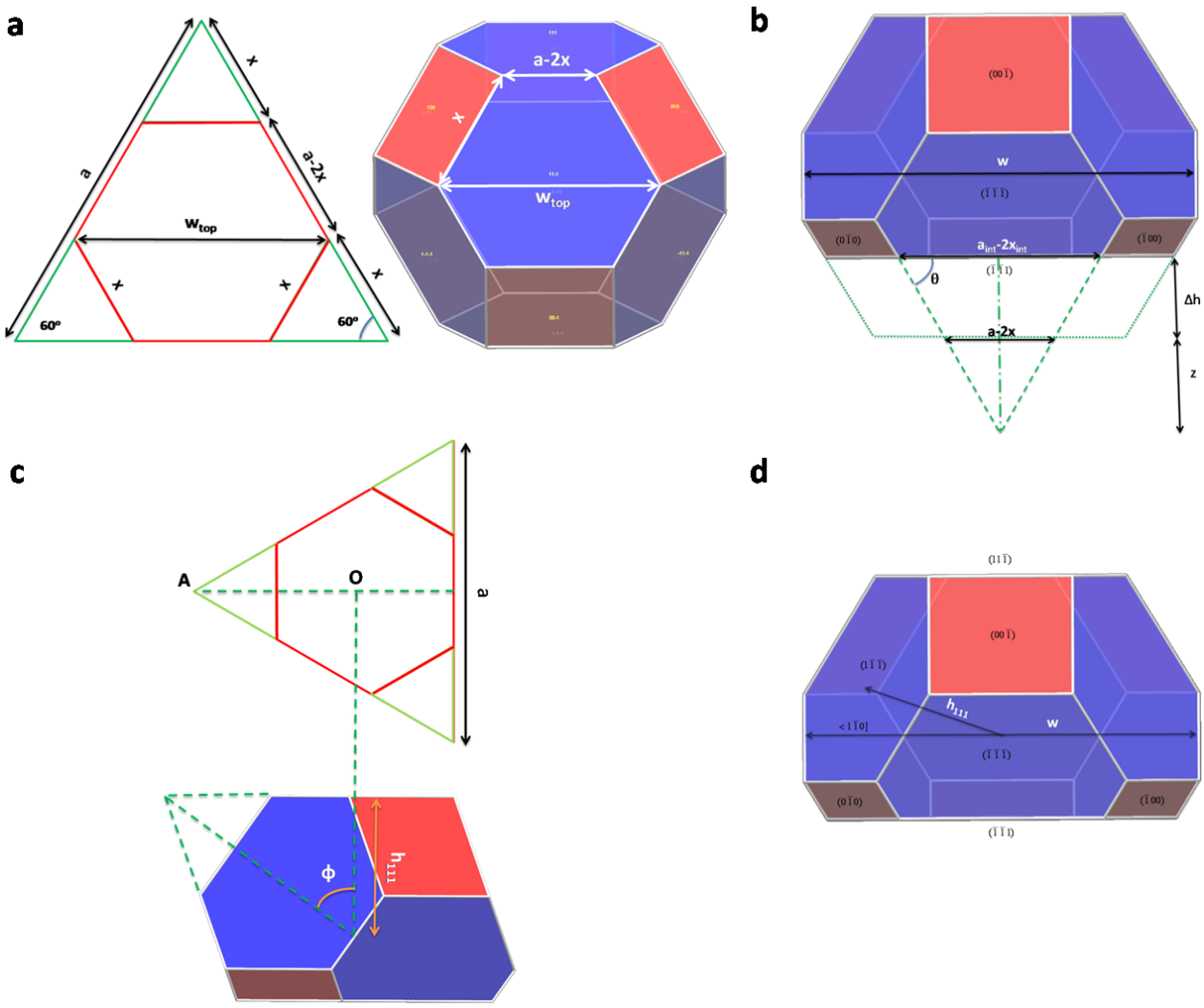

Figure 5.6: The ligher (blue) facets are {111} and darker (red) facets are {100}. (a) Plan view ES of a Au(111) facet. The green lines are not present in the real Au NC shown on the right. The edge with length 'x' is formed at the intersection of (111) facet with {100} facets. (b) Schematic of the ES of a supported Au NC viewed from the [112] zone axis. Δh is the undercut due to the formation of an interface. The dashed lines are a guide to the eye. (c) Schematic of the ES of a supported Au NC viewed from the [110] zone axis. The top figure shows a plan view of the (111) facet at the top of the Au NC. 'O' is the centroid of the top (111) facet. (d) Schematic of the ES of a supported Au NC viewed from the [112] zone axis. w is the width of the NC and h_{111} is the distance from the center of the unsupported NC to the center of any 111 facet.

5.2.5 Measuring the Ratio of γ_{100} and γ_{111} Surface Energies

Cross-sectional STEM images of $Au_{[112]}$ NCs also enabled us to estimate the surface energy ratios of Au(100) and Au(111) by looking for the best fit to the NC shape. For fitting NC shapes, we optimized our imaging conditions to obtain images without roughening the NC surface. We found that it was not possible to exactly fit the NC shape by using conventional Wulff construction wheret all NCs facets of the same family have identical surface energies. This is shown in Figure 5.7 where we obtained the best fit Wulff shape by assuming the ratio of $\gamma_{100}/\gamma_{111}$ to be 1.15 for all (100) facets. (The surface roughness in this image is seen to be much lesser than previously presented images since it was acquired using a fast scanning conditions that prevented beam damage of the NC. However, the resolution of this image is consequently poorer. This tradeoff is inevitable while obtaining images of NCs at room temperature.) It is seen in Figure 5.7 that the edge near the interface (indicated by arrow) does not fit well with the Wulff shape. This feature was typical of most $Au_{[112]}$ NCs, i.e. the undercutting resulting from Au{100} facets at the interface could not be satisfactorily fitted by a regular Wulff construction.

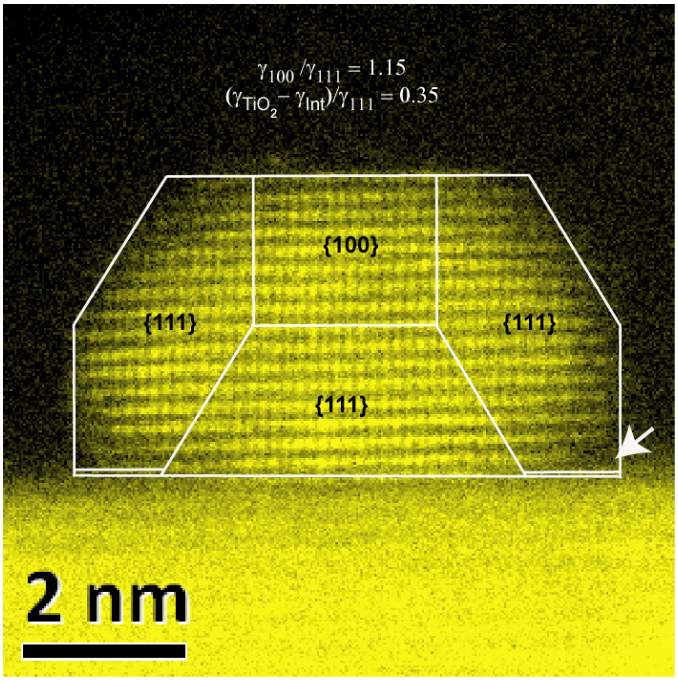

Figure 5.7: Fitting a Wulff shape to a $Au_{[112]}$ NC by using smaller surface energy values for Au{100} facets terminating at the interface.

Since we observed larger undercutting of Au {100} facets at the interface this implied a smaller surface energy for Au {100} facets at the interface. We found that by setting $\gamma_{100}/\gamma_{111}$ = 0.9 for Au {100} facets terminating at the interface, we were able to obtain a good fit for the NC shown in Figure 5.7. The new fit is shown in Figure 5.8, where $\gamma_{100}/\gamma_{111}$ = 1.15 for Au {100} facets near the top of the NC and $\gamma_{100}/\gamma_{111}$ = 0.9 for Au {100} facets near the interface.

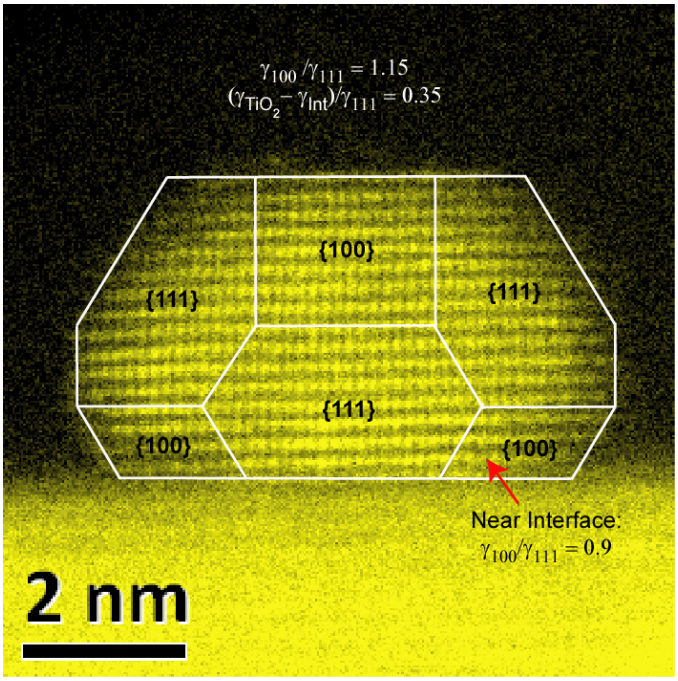

Figure 5.8: Fitting a Wulff shape to a $Au_{[112]}$ NC by using smaller surface energy values for Au{100} facets terminating at the interface.

It can be shown that $h_{100} = \sqrt{2}(r_{Int} - \Delta h/\tan\theta)$ for Au {100} facets terminating at the interface, where r_{Int} is half the width of the interface in the viewing direction and $\tan\theta = 1.633$. Since r_{Int} and Δh are directly measurable quantities, h100 at interface is also measurable. Also, since Au (111) is parallel to the interface, $h_{111} = h = w/\sqrt{6}$. Hence, it is possible to measure the ratio of $\gamma_{100}/\gamma_{111}$ (= h_{100}/h_{111}) for Au {100} facets terminating at the interface from measurable parameters in the images. Figure 5.9 shows a plot of $\gamma_{100}/\gamma_{111}$ versus NC width. It is seen from Figure 5.9 that the ratio of $\gamma_{100}/\gamma_{111}$ at the interface is mostly less than one with mean $\gamma_{100}/\gamma_{111}$ = 0.93.

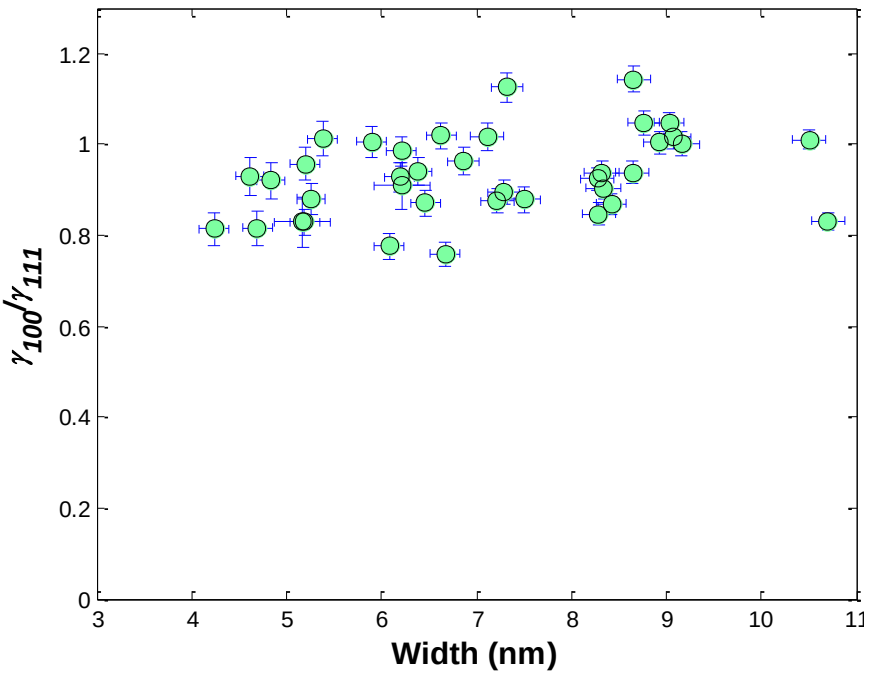

Figure 5.9: Plot of of $\gamma_{100}/\gamma_{111}$ versus NC width

5.3 Discussion

5.3.1 Line Tension

The value of line tension in our study of Au NCs on TiO_2 (110) is of the same order of magnitude of line tension measured recently at a grain boundary triple junction of copper ($6.0 \pm 3.0 \times 10^{-9}$ N).[177] However, the analysis so far has assumed that size dependence of NC shape is solely due to line tension. Other factors that could potentially affect the analysis and induce size dependent changes in ES of NCs include followings:–

a) *Size dependent interfacial energy* : A change in interfacial energy is expected when the interfacial atomic structure changes with size. This could happen for example by nucleation of dislocations at larger NC sizes (for example, Pd NCs on MgO).[178] By imaging the interfacial atomic structure with atomic resolution Scanning Transmission

Electron Microscopy (STEM), we found that atomic structure of interfaces were similar for all NC sizes and we did not observe misfit dislocations at the interface. In absence of obvious structural difference, we assume that the interfacial energy is nearly constant in all NCs we have investigated and does not contribute to the drop in Δh/h for smaller NCs in Figure 5.4(a).

b) *Size dependent surface energy*: Since $\Delta h/h = 1+ (\gamma_{TiO2} - \gamma_{Int})/\gamma_{Au}$ and $(\gamma_{TiO2} - \gamma_{Int} < 0)$, γ_{Au} should 'decrease' for smaller NCs in order to explain the trend in Figure 5.4(a). However, it is well known that surface energy increases for smaller NCs where the proportion of atoms at the edge sites of a surface increases. [99, 179]

c) *Size dependent interfacial strain relaxation*: Misfit strain arises due to the lattice mismatch of the NC and its support when the NC lattice is coherent or semi-coherent with the support's lattice. For Au NCs on TiO_2 (110), we observed full coherency at the interface with Au ($2\bar{2}0$) lattice planes aligning with TiO_2 (002) throughout the length of the interface. The misfit strain at this interface is ~2.3% ($d_{Au(110)}$ = 2.885Å, $d_{TiO2(001)}$ = 2.954Å). We observed that the strain relaxes as we move away from the interface and the Au (220) spacing away from the interface is close to the bulk Au (220) spacing. Misfit strain can have a significant impact on NC shape and can be quite complicated to model particularly when the strain relaxes away from the interface. The effect of interfacial misfit strain on the shape of NCs is profound in many supported NCs and has been extensively studied.[176, 180-184] When strain relaxation varies as a function of NC size, the self-similarity of supported NC shape will be lost. The loss of self similarity is expected to manifest as a non-linearity in a plot of nanocrystal (NC) height (H) versus NC width (w).[176, 185] In order to verify the effect of interfacial misfit strain relaxation

on the shape of Au NCs, we plotted the NC height (H) versus the NC width (w) (Figure 5.5). In Figure 5.5 we see that a plot of H versus w is linear with a R^2 value of 0.93. The linearity of H versus W suggests that the contribution to shape from strain relaxation can be approximated to be size-independent for the sizes of NCs in our experiments. Accurate measurement of strain and strain relaxation is not possible in our STEM images, however, because of STEM scan distortions, which is on the same order or larger than the strain.

By neglecting the size dependent effects of surface energy and strain relaxation, the measured value of LT represents a lower limit for the actual value of LT. To see this, we express Δh/h as a function of the ratio of NC height (H) and NC width (w):

$$\frac{\Delta h}{h} = \frac{2h - H}{h} = 2 - \frac{\sqrt{6}H}{w} \tag{5.33}$$

Muller and Kern have concluded analytically for a 2D rectangular crystal that misfit strain relaxation results in an increase of H/w with increasing NC size based on comparison with several experimental data.[176] According to equation (5.33), an increase in H/w corresponds to a decrease in Δh/h. Thus misfit strain relaxation is expected to result in a 'decrease' in Δh/h with increasing NC size. However our experimental measurements show that Δh/h increases for larger NCs (Figure 5.4(a)). Therefore if strain induced change in H/w contributed significantly to shape change, then the actual value of LT must be larger than what we have measured in order to overcompensate for the hypothetical strain induced decrease in Δh/h for larger NCs. Similar to the effect of strain, an increase in surface energy for smaller NCs should also result in an increase in Δh/h for smaller NCs as explained earlier. Because we have neglected the change in surface energy as well, the actual value of LT will have to also overcompensate for the effect of

surface energy on size in order to explain the observed decrease in Δh/h for smaller NCs. Thus by neglecting contributions of strain and surface energy, we are measuring a lower limit for LT.

5.3.2 Ratio of γ_{100} and γ_{111} near NC and Substrate Interface

The decrease in $\gamma_{100}/\gamma_{111}$ for Au {100} surfaces near the interface probably is the effect of interfacial misfit strain on surface stress and surface energy. The relation between surface stress and surface energy is given by the Shuttleworth-Herring equation[186] –

$$g_{ij} = \gamma\delta_{ij} + \frac{d\gamma}{d\varepsilon_{ij}} \tag{5.34}$$

where g_{ij} and ε_{ij} are components of the surface stress and strain tensors respectively and δ_{ij} is the Kronecker delta function. At the interface of the $Au_{[112]}$ NCs we know that there exists ~2.3% tensile strain from interfacial misfit. Interfacial misfit strain can alter the surface stress and surface energy of the Au facets terminating at the interface, thereby resulting in lower values for $\gamma_{100}/\gamma_{111}$ at the interface compared to $\gamma_{100}/\gamma_{111}$ expected for a free NC.

It is difficult to analytically model the change in surface stress and surface energy at the interface since surface stress (and consequently surface energy) is also affected by adsorbates.[187] The values for Au surface energies used in this work were obtained from earlier DFT calculations for metal surfaces in vacuum. Such calculations for the surface energies[66] and surface stresses[188] do not account for changes due to adsorbates such as gas atoms in ambient atmosphere. The adsorption of gases to the Au surfaces can result in complicated interactions that would require first principle calculations to accurately predict the change in surface stress and surface energy for Au facets near the interface.

5.4 Conclusion

In conclusion, we examined the ES of epitaxial Au NCs with the epitaxial relationship – $Au(111)_{[-110]} \parallel TiO_2(110)_{[001]}$ and found that shapes of epitaxial Au NCs were not self similar between the largest and smallest sizes analyzed in this work. The smaller NCs were more dewet than the larger NCs. We attributed the increased dewetting for smaller NCs to the increased effect of interfacial LT for smaller NCs. In order to measure LT, we incorporated the line tension into Wulff-Kaishew theorem and fitted a value of LT to the observed experimental NC shapes. By doing so, we measured the lower limit of LT for Au NCs supported on TiO_2 (110) to be 0.85±0.24 eV/Å (1.36±0.38 x 10^{-9} N) by using $\gamma_{Au(111)}$ = 1.283 J/m^2 and $\gamma_{TiO2(110)}$ = 0.33 J/m^2. In this measurement, we neglected the effects of change in strain relaxation and surface energy with NC size.

Further, we also found that the ratio $\gamma_{100}/\gamma_{111}$ is ~0.93 for Au {100} facets near the interface. We attribute this reduced value of $\gamma_{100}/\gamma_{111}$ to the effect of interfacial misfit strain on the surface stress and surface energy of Au facets at the interface.

CHAPTER 6

SUMMARY AND CONCLUSIONS

6.1 RHEED Studies of Au and Ag NCs on TiO_2 (110)

The epitaxial formation of Au and Ag NCs on different surfaces of TiO_2 (110) with varied stoichiometry was investigated. For Au NCs, the following critical observations were made –

a) Irrespective of whether the starting stoichiometry of TiO_2 (110) was oxygen-rich or oxygen-deficient and irrespective of whether the annealing was carried out in vacuum or air, the Au NCs always evolved to the same epitaxial arrangement. This ubiquitous epitaxy was found to be – Au $(111)_{[-110]} \parallel TiO_2\,(110)_{[001]}$.
b) After the formation of epitaxial Au NCs, a (1x2) TiO_2 (110) reconstruction was seen in the RHEED patterns in all the above cases.
c) The onset of epitaxial rearrangement of Au NCs on oxygen-deficient and (1x2) reconstructed TiO_2 happens at ~600^{o}C on reduced TiO_2 (110) surfaces while the onset of epitaxial rearrangement of Au NCs on oxygen-rich happens at ~750^{o}C.

These observations led to the conclusion that epitaxial rearrangement of Au NCs on TiO_2 (110) proceeds by the nucleation of Au over (1x2) TiO_2 (110) reconstructions. The lattice match of Au and TiO_2 along Au [-110] and TiO_2 [001] drives the formation of the first few atomic layers which serve as nuclei for further growth of Au NCs. TiO_2 (110) surfaces that have large number of (1x2) areas are able to nucleate epitaxial Au NCs more readily than TiO_2 (110) surfaces which have little (1x2) reconstruction areas. The proposed interface of Au (111) and

(1x2) reconstructed TiO_2 also explains the stability of Au(111)/TiO_2(110) interfaces which have reported many times before despite theoretical calculations that the interface has a negligible work of adhesion on oxidized TiO_2 (110).

Epitaxial rearrangement of Ag NCs on TiO_2 (110) responds differently to the stoichiometry of the TiO_2 support. While a similar epitaxy (Ag $(111)_{[-110]} \parallel TiO_2\ (110)_{[001]}$) was observed for Ag NCs supported on oxygen-rich or oxygen-deficient supports, some of the Ag NCs supported on oxygen-rich TiO_2 (110) also evolved into another favorable epitaxial configuration (Ag $(112)_{[-110]} \parallel TiO_2\ (110)_{[001]}$). For Ag NCs also, the onset of epitaxial rearrangement happened at lower temperatures on a reduced TiO_2 (110) support. Further, the sublimation of Ag NCs as a function of the support stoichiometry was also investigated. It was found that Ag NCs supported on oxygen-rich TiO_2 (110) sublimed at higher temperatures than Ag NCs supported on reduced TiO_2 (110). While it is well known that the sublimation temperature of unsupported or weakly supported NCs are determined by NC size,[189] our studies on the effect of TiO_2 (110) stoichiometry on Ag NC sublimation highlight the need for considering the effect of interfacial adhesion of NCs when determining the sublimation temperature of supported NCs.

6.2 Enhanced Adhesion of $Au_{[112]}$ NCs on TiO_2 (110) from Interfacial Reconstruction

The interface of $Au_{[112]}$ NCs on TiO_2 (110) was investigated using aberration corrected Scanning Transmission Electron Microscopy (STEM) in order to understand the enhanced interfacial adhesion of this interface as compared to other interfaces observed in Au/TiO_2(110). Consistent with the conclusions from RHEED, it was found that the interface of $Au_{[112]}$ NCs was formed by Au atoms sitting along a missing Ti row of a (1x2) reconstruction proposed by Pang

et al.[54] By sitting periodically in the missing Ti row, the interface of $Au_{[112]}$ NCs becomes an ordered mix of Au, Ti and O – termed as an interfacial reconstruction.

Conventionally, the chemical interactions between metal NCs and oxides are classified into redox reaction, alloy formation, encapsulation, interdiffusion and no interaction.[57, 190] From thermodynamic free energy of heats of reactions and surface energy considerations, Au is not expected to have no chemical interactions on TiO_2 (110).[49] In our work, we have observed a novel interaction between Au and TiO_2 where Au atoms, driven by lattice match constraints, nucleate along the missing Ti row of the (1x2) TiO_2 reconstruction – resulting in an interfacial reconstruction of Au, Ti and O atoms. This novel interfacial arrangement of atoms leads to an enhanced interfacial adhesion for Au NCs on TiO_2 (110). The enhanced adhesion of metal-oxide interfaces from interfacial reconstruction reveals another pathway for creating stable metal-oxide interfaces for commercially relevant systems such as catalysts, thermal barrier coatings, erosion and corrosion resistant coatings, wear resistant coatings etc.

6.3 Measurement of Interfacial Line Tension in $Au_{[112]}$ NCs Supported on TiO_2 (110)

This work concerns the first experimental measurements of interfacial line tension (LT) of supported NCs and the demonstration of its importance in determining equilibrium shape (ES) of NCs. By studying epitaxial gold NCs supported on titanium dioxide using aberration corrected electron microscopy, we found that shapes of gold NCs were not self-similar below 10nm. We have explained this unexpected observation by accounting for interfacial line tension that was measured to be 1.03±0.24 eV/Å (1.65±0.40 x 10^{-9} N) for $Au(111)_{[-110]}||TiO_2(110)_{[001]}$.

More than hundred years ago Gibbs had predicted line tension to be a fundamental physical property of an interface. However there have been no measurements of line tension of

3D supported NCs till date. Our breakthrough in measuring this fundamental interfacial property not only provides an estimate for line tensions of supported NCs but also demonstrates an experimental technique that can spur advancements in accurately predicting nucleation, growth and ES of NCs. Our technique is particularly appealing for material systems that require processing in ambient.

Further, we also found that the ratio $\gamma_{100}/\gamma_{111}$ for Au {100} facets near the interface was 0.93, which was unexpected since experimental measurements[134] of and theoretical estimates[66] of $\gamma_{100}/\gamma_{111}$ are always greater than one, i.e. the {100} facets are less stable than {111} facets. We attributed this reduced value of $\gamma_{100}/\gamma_{111}$ to the effect of interfacial misfit strain on the surface stress and surface energy of Au facets at the interface.

6.4 Outlook

Nanocrystal interfaces, like nanocrystal surfaces, are an important issue in nanomaterials research. Most nanocrystals used in applications are supported; the interface can have a large effect on nanocrystal properties. Interfacial phenomena at the nanoscale can often lead to surprising and distinctive functionality.[191, 192] Electron microscopy is one of best tools for studying interfaces. Recent developments in aberration corrected electron microscopy has brought significantly new insights to oxide interfaces,[152] grain boundaries. [151] The work presented in this thesis is the first elucidation of atomistic structure at a very important nanocrystal interface by aberration corrected electron microscopy. Furthermore, we demonstrate that unambiguous nanocrystal shape information can be obtained from the electron images. The unambiguous shape information helped us to measure the line tension for Au NCs supported on

TiO_2, a thermodynamic parameter that could prove useful in understanding nucleation and growth of NCs better.

We selected the Au/TiO_2 interface for study because of the tremendous interest in this system due to the unusual catalytic activity of Au nanoparticles. Interfacial Au cations has been suggested as responsible for Au/TiO_2's catalytic activity.[46] However, there has been no conclusive evidence for the existence of interfacial Au atoms of different chemical nature. The study presented here also shows for the first time that the interfacial reconstruction of Au, Ti and O atoms possibly results in cationic Au species at the interface.

Despite much progress, many questions remain – both for Au/TiO_2 specifically and for NC interfaces in general. Future work should help sort out some of the big questions raised by this study. In this regard, some of the following outlined experiments will be useful –

(i) Quantitative 2D atomic resolution chemical characterization of NC interfaces – The ideal characterization of any interface would involve understanding the atomic structure and its electronic (chemical) structure. The characterization of a NC interface's atomic structure is easier than the characterization of its electronic structure. EELS offers the best local probing technique to study the electronic structure of interfaces. However, as explained in chapter 4, atomic resolution EELS is difficult since EELS delocalization is not only a function of probe size but also atomic scattering to neighboring columns. EELS delocalization can be minimized by using thinner specimens and higher energy electrons. However, both are not trivial issues since thinner specimens are more difficult to synthesize and higher energy electron can cause more beam damage to the specimen.

Further, quantitative EELS interpretation requires the use of multislice and DFT simulations for determining delocalization and electronic structure. Nevertheless, quantitative understanding of EEL spectra combined with atomic resolution analysis will pave way for a better understanding of interfaces. Also, while all EEL spectra shown in this work are line scans, 2D EELS, which has been demonstrated by many groups will be ideal for the characterization of NC interfaces where the edge atoms of the interface have different electronic structures than atoms in the interior of the interface. 2D EELS has not yet been reported for NC interfaces since the beam damage during 2D EELS is large. However, with the advent of faster EELS acquisition systems and better energy filters which reject little signal, 2D EELS of NC interfaces are a realistic possibility.

(ii) Line tension of NCs – Line tension is a thermodynamic parameter that has been sparsely measured for supported NCs despite its significance in nucleation and growth of NCs, nanowires, stability of quantum dots etc. The experimental difficulty in measuring line tension is because it is manifest only at smaller NC sizes whereas shape measurement of smaller NCs is not straightforward even with aberration corrected microscopes. An alternative is to use scanning probe microscopes (SPMs). SPMs are useful for measuring shapes of 2D NCs, but do not in general give atomic resolution for 3D metallic NCs. For using aberration corrected microscopes for shape measurement of small NCs, care must be taken to ensure that the NC shape is not altered by beam damage. Better electron detectors can greatly increase the efficiency of signal collection and reduce the time spent on collecting images of NCs. In our experience, STEM is better than TEM when studying NC shapes, since beam damage is lesser in STEM. However, the scan distortion in STEM images still has room for improvement in order to get strain information simultaneously

with shape information. Obtaining strain information is very critical to measuring line tension with confidence since size dependent strain in NCs can also affect the shape of NCs and lead to erroneous measurement of line tension.

REFERENCES

1. van Santen, R.A., et al., *CATALYSIS: AN INTEGRATED APPROACH*. 1999, Amsterdam: Elsevier. 574.

2. Anderson, J.A. and M.F. Garcia, *Supported Metals in Catalysis*. Catalytic Science Series, ed. G.J. Hutchings. Vol. 5. 2005, London: Imperial College Press. 368.

3. Astruc, D., *Organometallic Chemistry and Catalysis*. 2007, New York: Springer Berlin Heidelberg. 611.

4. Pattrick, G., et al., *The potential for use of gold in automotive pollution control technologies: a short review.* Topics in Catalysis, 2004. 30-1(1-4): p. 273-279.

5. Hayashi, T., K. Tanaka, and M. Haruta, *Selective vapor-phase epoxidation of propylene over Au/TiO2 catalysts in the presence of oxygen and hydrogen.* Journal of Catalysis, 1998. 178(2): p. 566-575.

6. Hutchings, G.J., *Catalysis by gold.* Catalysis Today, 2005. 100(1-2): p. 55-61.

7. Haruta, M., et al., *Novel Gold Catalysts for the Oxidation of Carbon-Monoxide at a Temperature Far Below 0-Degrees-C.* Chemistry Letters, 1987(2): p. 405-408.

8. Yin, Y. and A.P. Alivisatos, *Colloidal nanocrystal synthesis and the organic-inorganic interface.* Nature, 2005. 437(7059): p. 664-670.

9. Billinge, S.J.L. and I. Levin, *The problem with determining atomic structure at the nanoscale.* Science, 2007. 316(5824): p. 561-565.

10. Williams, D.B. and B.C. Carter, *Transmission Electron Microscopy: Basics*. 1996, New York: Springer Science+Business Media Inc.

11. Scherzer, O., *The theoretical resolution limit of the electron microscope.* J. Appl. Phys., 1949. 20: p. 20-28.

12. Beck, V.D., *Hexapole Spherical-Aberration Corrector.* Optik, 1979. 53(4): p. 241-255.

13. Rose, H., *Outline of a Spherically Corrected Semiaplanatic Medium-Voltage Transmission Electron Microscope.* Optik, 1990. 85(1): p. 19-24.

14. Zach, J.C. and M. Haider, *Aberration Correction in a Low-Voltage Sem by a Multipole Corrector.* Nucl. Instrum. Methods Phys. Res., Sect. A, 1995. 363(1-2): p. 316-325.

15. Haider, M., et al., *Electron microscopy image enhanced.* Nature, 1998. 392(6678): p. 768-769.

16. Krivanek, O.L., et al., *Towards Sub-0.5 Angstrom Electron Beams.* Ultramicroscopy, 2003. 96(3-4): p. 229-237.

17. Batson, P.E., N. Dellby, and O.L. Krivanek, *Sub-angstrom Resolution Using Aberration Corrected Electron Optics.* Nature, 2002. 418: p. 617-620.

18. Spence, J.C.H., *High-Resolution Electron Microscopy* 3rd ed. 2003, Oxford, UK: Oxford University Press. 424.

19. Crewe, A.V. and J. Wall, *A Scanning Microscope with 5 Å Resolution.* J. Mol. Biol., 1970. 48(3): p. 375-393.

20. Howie, A., *Image-Contrast and Localized Signal Selection Techniques.* J. Microsc. (Oxf), 1979. 117: p. 11-23.

21. Egerton, R.F., *Electron Energy-loss Spectroscopy in the Electron Microscope*. 2nd ed. 1996, New York: Plenum. 500.

22. Ahn, C.C., M.M. Disko, and B. Fultz, *Transmission Electron Energy Loss Spectrometry in Materials Science and EELS Atlas*. 2nd ed, ed. C.C. Ahn. 2004, Weinheim: Wiley-VCH. 400.

23. Browning, N.D., M.F. Chisholm, and S.J. Pennycook, *Atomic-Resolution Chemical-Analysis Using a Scanning-Transmission Electron-Microscope.* Nature, 1993. 366(6451): p. 143-146.

24. Kimoto, K., et al., *Element-selective Imaging of Atomic Columns in a Crystal Using STEM and EELS.* Nature, 2007. 450: p. 702-704.

25. Muller, D.A., et al., *Atomic-Scale Chemical Imaging of Composition and Bonding by Aberration-Corrected Microscopy.* Science, 2008. 319: p. 1073-1076.

26. Muller, D.A., *Structure and bonding at the atomic scale by scanning transmission electron microscopy.* Nature Mater., 2009. 8(4): p. 263-270.

27. Shibata, N., et al., *Atomic-scale imaging of individual dopant atoms in a buried interface.* Nature Materials, 2009. 8(8): p. 654-658.

28. Klie, R.F., et al., *Enhanced current transport at grain boundaries in high-Tc superconductors.* Nature, 2005. 435(7041): p. 475-478.

29. Bond, G.C. and D.T. Thompson, *Catalysis by Gold.* Catalysis Reviews, 1999. 41(3): p. 319 - 388.

30. Haruta, M., *Size- and support-dependency in the catalysis of gold.* Catalysis Today, 1997. 36(1): p. 153-166.

31. Haruta, M., *Catalysis of Gold Nanoparticles Deposited on Metal Oxides.* CATTECH, 2002. 6(3): p. 102-115.

32. Meyer, R., et al., *Surface chemistry of catalysis by gold.* Gold Bulletin, 2004. 37(1-2): p. 72-+.

33. Min, B.K. and C.M. Friend, *Heterogeneous gold-based catalysis for green chemistry: Low-temperature CO oxidation and propene oxidation.* Chemical Reviews, 2007. 107(6): p. 2709-2724.

34. Chen, M.S. and D.W. Goodman, *Structure-activity relationships in supported Au catalysts.* Catalysis Today, 2006. 111(1-2): p. 22-33.

35. Haruta, M., et al., *Low-Temperature Oxidation of CO over Gold Supported on TiO2, [alpha]-Fe2O3, and Co3O4.* Journal of Catalysis, 1993. 144(1): p. 175-192.

36. Chretien, S., S.K. Buratto, and H. Metiu, *Catalysis by very small Au clusters.* Current Opinion in Solid State & Materials Science, 2007. 11(5-6): p. 62-75.

37. Bond, G.C. and D.T. Thompson, *Gold-catalysed oxidation of carbon monoxide.* Gold Bulletin, 2000. 33(2): p. 41-51.

38. Lemire, C., et al., *CO adsorption on oxide supported gold: from small clusters to monolayer islands and three-dimensional nanoparticles.* Surface Science, 2004. 552(1-3): p. 27-34.

39. Janssens, T.V.W., et al., *Relation between nanoscale Au particle structure and activity for CO oxidation on supported gold catalysts.* Journal of Catalysis, 2006. 240(2): p. 108-113.

40. Lopez, N., et al., *On the origin of the catalytic activity of gold nanoparticles for low-temperature CO oxidation.* Journal of Catalysis, 2004. 223(1): p. 232-235.

41. Valden, M., X. Lai, and D.W. Goodman, *Onset of catalytic activity of gold clusters on titania with the appearance of nonmetallic properties.* Science, 1998. 281(5383): p. 1647-1650.

42. Vijay, A., G. Mills, and H. Metiu, *Adsorption of gold on stoichiometric and reduced rutile TiO2 (110) surfaces.* Journal of Chemical Physics, 2003. 118(14): p. 6536-6551.

43. Yoon, B., et al., *Charging effects on bonding and catalyzed oxidation of CO on Au-8 clusters on MgO.* Science, 2005. 307(5708): p. 403-407.

44. Sanchez, A., et al., *When gold is not noble: Nanoscale gold catalysts.* Journal of Physical Chemistry A, 1999. 103(48): p. 9573-9578.

45. Grunwaldt, J.D. and A. Baiker, *Gold/titania interfaces and their role in carbon monoxide oxidation.* Journal of Physical Chemistry B, 1999. 103(6): p. 1002-1012.

46. Bond, G.C., C. Louis, and D.T. Thompson, *Catalysis by Gold*. Catalytic Science Series, ed. G.J. Hutchings. Vol. 6. 2006, London: Imperial College Press. 366.

47. Hodge, N.A., et al., *Microstructural comparison of calcined and uncalcined gold/iron-oxide catalysts for low-temperature CO oxidation.* Catalysis Today, 2002. 72(1-2): p. 133-144.

48. Henry, C.R., *Surface studies of supported model catalysts.* Surface Science Reports, 1998. 31(7-8): p. 235-325.

49. Diebold, U., *The surface science of titanium dioxide.* Surface Science Reports, 2003. 48(5-8): p. 53-229.

50. Grant, F.A., *Properties of Rutile (Titanium Dioxide).* Reviews of Modern Physics, 1959. 31(3): p. 646-674.

51. Brittain, H.G., *The Oxide Handbook, 2nd Edition - Samsonov,Gv.* Journal of the American Chemical Society, 1983. 105(8): p. 2514-2514.

52. Duke, C.B., *Surface-Structures of Tetrahedrally Coordinated Semiconductors - Principles, Practice, and Universality.* Applied Surface Science, 1993. 65-6: p. 543-552.

53. Ramamoorthy, M., D. Vanderbilt, and R.D. Kingsmith, *1st-Principles Calculations of the Energetics of Stoichiometric Tio2 Surfaces.* Physical Review B, 1994. 49(23): p. 16721-16727.

54. Pang, C.L., et al., *Added row model of TiO2(110)1x2.* Physical Review B, 1998. 58(3): p. 1586-1589.

55. Onishi, H., K. Fukui, and Y. Iwasawa, *Atomic-Scale Surface-Structures of Tio2 (110) Determined by Scanning-Tunneling-Microscopy - a New Surface-Limited Phase of Titanium-Oxide.* Bulletin of the Chemical Society of Japan, 1995. 68(9): p. 2447-2458.

56. Park, K., et al., *Surface reconstructions of TiO2(110) driven by suboxides.* Physical Review Letters, 2006. 96(22).

57. Campbell, C.T., *Ultrathin metal films and particles on oxide surfaces: structural, electronic and chemisorptive properties.* Surface Science Reports, 1997. 27(1-3): p. 1-111.

58. Tauster, S.J., *Strong Metal-Support Interactions.* Accounts of Chemical Research, 1987. 20(11): p. 389-394.

59. Pillay, D., Y. Wang, and G.S. Hwang, *Nucleation and growth of 1B metal clusters on rutile TiO2(110): Atomic level understanding from first principles studies.* Catalysis Today, 2005. 105(1): p. 78-84.

60. Giordano, L., et al., *Cu, Ag, and Au atoms adsorbed on TiO2(110): cluster and periodic calculations.* Surface Science, 2001. 471(1-3): p. 21-31.

61. Lopez, N., et al., *The adhesion and shape of nanosized Au particles in a Au/TiO2 catalyst.* Journal of Catalysis, 2004. 225(1): p. 86-94.

62. Wahlstrom, E., et al., *Bonding of gold nanoclusters to oxygen vacancies on rutile TiO2(110).* Physical Review Letters, 2003. 90(2).

63. Cosandey, F. and T.E. Madey, *Growth, morphology, interfacial effects and catalytic properties of Au on TiO2.* Surface Review and Letters, 2001. 8(1-2): p. 73-93.

64. Zhang, L., R. Persaud, and T.E. Madey, *Ultrathin metal films on a metal oxide surface: Growth of Au on TiO2 (110).* Physical Review B, 1997. 56(16): p. 10549.

65. Lai, X., et al., *Scanning tunneling microscopy studies of metal clusters supported on TiO2 (110): Morphology and electronic structure.* Progress in Surface Science, 1998. 59(1-4): p. 25-52.

66. Vitos, L., et al., *The surface energy of metals.* Surface Science, 1998. 411(1-2): p. 186-202.

67. Overbury, S.H., P.A. Bertrand, and G.A. Somorjai, *Surface composition of binary systems. Prediction of surface phase diagrams of solid solutions.* Chem. Rev., 1975. 75(5): p. 547-560.

68. Lopez, N. and J.K. Norskov, *Theoretical study of the Au/TiO2(1 1 0) interface.* Surface Science, 2002. 515(1): p. 175-186.

69. Akita, T., et al., *SEM and RHEED-REM study of au particles deposited on rutile TiO2 (110) by deposition precipitation and gas-phase grafting methods.* Journal of Catalysis, 2002. 212(1): p. 119-123.

70. Cosandey, F., L. Zhang, and T.E. Madey, *Effect of substrate temperature on the epitaxial growth of Au on TiO2(110).* Surface Science, 2001. 474(1-3): p. 1-13.

71. Crewe, A.V. and J. Wall, *Contrast in a High Resolution Scanning Transmission Electron Microscope.* Optik, 1970. 30(5): p. 461-474.

72. Wall, J., et al., *Scanning-Transmission Electron-Microscopy at High-Resolution.* Proceedings of the National Academy of Sciences of the United States of America, 1974. 71(1): p. 1-5.

73. Reimer, L., *Transmission Electron Microscopy: Physics of Image Formation and Microanalysis*. 4th ed. 1995, New York: Springer.

74. Engel, A., J.W. Wiggins, and D.C. Woodruff, *Comparison of Calculated Images Generated by 6 Modes of Transmission Electron-Microscopy.* Journal of Applied Physics, 1974. 45(6): p. 2739-2747.

75. Wang, Z.L. and J.M. Cowley, *Simulating High-Angle Annular Dark-Field Stem Images Including Inelastic Thermal Diffuse-Scattering.* Ultramicroscopy, 1989. 31(4): p. 437-454.

76. Hall, C.R. and P.B. Hirsch, *Effect of thermal diffuse scattering on propagation of high energy electrons through crystals.* Proceedings of the Royal Society of London, Series A (Mathematical and Physical Sciences), 1965. 286(1405): p. 158-177.

77. Pennycook, S.J., *Z-Contrast Stem for Materials Science.* Ultramicroscopy, 1989. 30(1-2): p. 58-69.

78. Haider, M., S. Uhlemann, and J. Zach, *Upper limits for the residual aberrations of a high-resolution aberration-corrected STEM.* Ultramicroscopy, 2000. 81(3-4): p. 163-175.

79. Wen, J.G., et al., *The Formation and Performance of Sub-Angstrom to Nanometer-Sized Electron Probes Using the Aberration Corrected JEOL 2200FS Transmission Electron Microscope at the University of Illinois.* Microscopy and Microanalysis, 2010.

80. Pennycook, S.J. and D.E. Jesson, *High-Resolution Z-Contrast Imaging of Crystals.* Ultramicroscopy, 1991. 37(1-4): p. 14-38.

81. Spence, J.C.H. and P.W. Hawkes, *Science of Microscopy*. 2006: Springer. 696.

82. Mitterbauer, C., et al., *Electron energy-loss near-edge structures of 3d transition metal oxides recorded at high-energy resolution.* Ultramicroscopy, 2003. 96(3-4): p. 469-480.

83. Egerton, R.F., *New techniques in electron energy-loss spectroscopy and energy-filtered imaging.* Micron, 2003. 34(3-5): p. 127-139.

84. Morin, R. and H.W. Fink, *Highly Monochromatic Electron Point-Source Beams.* Applied Physics Letters, 1994. 65(18): p. 2362-2364.

85. Graef, M.D., *Introduction to Conventional Transmission Electron Microscopy*. 2003: Cambridge. 718.

86. Cowley, J.M., *Diffraction Physics*. 3rd ed. 1995: Elsevier Science. 481.

87. Iizuka, Y., et al., *Adsorption of CO on gold supported on TiO₂*. Catalysis Today, 1997. 36(1): p. 115-123.

88. Akita, T., et al., *HAADF-STEM observation of Au nanoparticles on TiO2.* Surface and Interface Analysis, 2008. 40(13): p. 1760-1763.

89. Akita, T., et al., *Analytical high-resolution TEM study of supported gold catalysts: orientation relationship between Au particles and TiO2 supports.* Journal of Electron Microscopy, 2000. 49(5): p. 657-662.

90. Chen, M.S. and D.W. Goodman, *The structure of catalytically active gold on titania.* Science, 2004. 306(5694): p. 252-255.

91. Chusuei, C.C., et al., *Modeling heterogeneous catalysts: metal clusters on planar oxide supports.* Topics in Catalysis, 2000. 14(1): p. 71-83.

92. Giorgio, S., M. Cabie, and C.R. Henry, *Dynamic observations of Au catalysts by environmental electron microscopy.* Gold Bulletin, 2008. 41(2): p. 167-173.

93. Jiang, Z.Q., et al., *Direct XPS evidence for charge transfer from a reduced rutile TiO2(110) surface to Au clusters.* Journal of Physical Chemistry C, 2007. 111(33): p. 12434-12439.

94. Lai, X. and D.W. Goodman, *Structure-reactivity correlations for oxide-supported metal catalysts: new perspectives from STM.* Journal of Molecular Catalysis A: Chemical, 2000. 162(1-2): p. 33-50.

95. Lazzari, R., et al., *Self-similarity during growth of the Au/TiO2(110) model catalyst as seen by the scattering of x-rays at grazing-angle incidence.* Physical Review B, 2007. 76(12).

96. Matthey, D., et al., *Enhanced Bonding of Gold Nanoparticles on Oxidized TiO2(110).* Science, 2007. 315(5819): p. 1692-1696.

97. Mitchell, C.E.J., et al., *Direct observation of behaviour of Au nanoclusters on TiO2(1 1 0) at elevated temperatures.* Surface Science, 2001. 490(1-2): p. 196-210.

98. Okazawa, T., M. Kohyama, and Y. Kido, *Electronic properties of Au nano-particles supported on stoichiometric and reduced TiO2(1 1 0) substrates.* Surface Science, 2006. 600(19): p. 4430-4437.

99. Parker, S.C. and C.T. Campbell, *Kinetic model for sintering of supported metal particles with improved size-dependent energetics and applications to Au on TiO2(110).* Physical Review B, 2007. 75(3).

100. Shibata, N., et al., *Direct imaging of reconstructed atoms on TiO2 (110) surfaces.* Science, 2008. 322(5901): p. 570-573.

101. Shibata, N., et al., *Interface Structures of Gold Nanoparticles on TiO2 (110).* Physical Review Letters, 2009. 102(13).

102. Zhang, L., et al., *Initial growth and morphology of thin Au films on TiO2(110).* Surface Science, 1999. 439(1-3): p. 73-85.

103. Ioannides, T. and X.E. Verykios, *Charge transfer in metal catalysts supported on doped TiO2: A theoretical approach based on metal-semiconductor contact theory.* Journal of Catalysis, 1996. 161(2): p. 560-569.

104. Wang, Y. and G.S. Hwang, *Adsorption of Au atoms on stoichiometric and reduced TiO2(110) rutile surfaces: a first principles study.* Surface Science, 2003. 542(1-2): p. 72-80.

105. Luo, K., et al., *Silver growth on TiO2(110)(1x1) and (1x2).* Journal of Physical Chemistry B, 2000. 104(14): p. 3050-3057.

106. Chen, D.A., et al., *Small, uniform, and thermally stable silver particles on TiO2(110)-(1x1).* Surface Science, 2000. 464(1): p. L708-L714.

107. Baletto, F. and R. Ferrando, *Structural properties of nanoclusters: Energetic, thermodynamic, and kinetic effects.* Reviews of Modern Physics, 2005. 77(1): p. 371-423.

108. Bording, J.K., et al., *Size- and shape-dependent energetics of nanocrystal interfaces: Experiment and simulation.* Physical Review Letters, 2003. 90(22).

109. Li, B.Q. and J.M. Zuo, *Structure and shape transformation from multiply twinned particles to epitaxial nanocrystals: Importance of interface on the structure of Ag nanoparticles.* Physical Review B, 2005. 72(8).

110. Canario, A.R., et al., *Growth of Ag nanostructures on TiO2(1 1 0).* Surface Science, 2003. 547(3): p. L887-L894.

111. Burda, C., et al., *Chemistry and properties of nanocrystals of different shapes.* Chemical Reviews, 2005. 105(4): p. 1025-1102.

112. Zayed, M.K. and H.E. Elsayed-Ali, *Melting and solidification study of as-deposited and recrystallized bi thin films.* Journal of Applied Physics, 2006. 99(12): p. 123516-1.

113. Sato, K., et al., *Size-dependent structural transition from multiple-twinned particles to epitaxial fcc nanocrystals and nanocrystal decay.* Physical Review B (Condensed Matter and Materials Physics), 2007. 76(14): p. 144113-8.

114. Claus, P. and H. Hofmeister, *Electron microscopy and catalytic study of silver catalysts: Structure sensitivity of the hydrogenation of crotonaldehyde.* Journal of Physical Chemistry B, 1999. 103(14): p. 2766-2775.

115. Grunert, W., et al., *Structural properties of Ag/TiO2 catalysts for acrolein hydrogenation.* Journal of Physical Chemistry B, 2004. 108(18): p. 5709-5717.

116. Su, C.C., et al., *The adsorption and reactions of methyl iodide on powdered Ag/TiO2.* Catalysis Today, 2004. 97(1): p. 71-79.

117. Min, L., et al., *Oxygen-induced restructuring of the TiO₂(110) surface: a comprehensive study.* Surface Science, 1999. 437(1-2): p. 173-90.

118. Diebold, U., et al. *The relationship between bulk and surface properties of rutile TiO₂(110).* 2000. Park City, UT, USA: World Scientific.

119. Li, M., W. Hebenstreit, and U. Diebold, *Morphology change of oxygen-restructured TiO₂(110) surfaces by UHV annealing: Formation of a low-temperature (1×2) structure.* Physical Review B (Condensed Matter), 2000. 61(7): p. 4926-33.

120. Murray, P.W., N.G. Condon, and G. Thornton, *Effect of Stoichiometry on the Structure of Tio2(110).* Physical Review B, 1995. 51(16): p. 10989-10997.

121. Castro, T., et al., *Size-Dependent Melting Temperature of Individual Nanometer-Sized Metallic Clusters.* Physical Review B, 1990. 42(13): p. 8548-8556.

122. Shyjumon, I., et al., *Structural deformation, melting point and lattice parameter studies of size selected silver clusters.* European Physical Journal D, 2006. 37(3): p. 409-415.

123. Mezey, L.Z. and J. Giber, *The Surface Free-Energies of Solid Chemical-Elements - Calculation from Internal Free Enthalpies of Atomization.* Japanese Journal of Applied Physics Part 1-Regular Papers Short Notes & Review Papers, 1982. 21(11): p. 1569-1571.

124. Pabisiak, T. and A. Kiejna, *First-principles study of Au nanostructures on rutile TiO2(110).* Physical Review B, 2009. 79(8).

125. Locatelli, A., et al., *One-dimensional Au on TiO2.* Journal of Physics-Condensed Matter, 2007. 19(8).

126. MenteÅŸ, T.O., et al., *Surface modification of oxides by electron-stimulated desorption for growth-mode control of metal films: Experiment and density-functional calculations.* Physical Review B, 2007. 76(15): p. 155413.

127. Wulff, G., Zeitschrift für Kristallographie, 1901. 34.

128. Benson, G.C. and D. Patterson, *Note on an Analytical Proof of Wulff's Theorem in Three Dimensions.* The Journal of Chemical Physics, 1955. 23(4): p. 670-672.

129. Herring, C., *Structure and Properties of Solid Surfaces*, Chicago: University of Chicago Press.

130. von Laue, M., Zeitschrift fur Kristallographie, 1943. 105: p. 124.

131. Kaishew, R., in *Arbeitstagung Festköper Physik* 1952, Dresden.

132. R. Kern, G.L.L., J.J. Metois, *Basic Mechanisms in the Early Stage of Epitaxy.* Current Topics in Materials Science, 1979. 3: p. 135-419.

133. Sadan, H. and W.D. Kaplan, *Auâ€“Sapphire (0001) solidâ€“solid interfacial energy.* Journal of Materials Science, 2006. 41(16): p. 5099-5107.

134. Heyraud, J.C. and J.J. Metois, *Equilibrium shape of gold crystallites on a graphite cleavage surface: Surface energies and interfacial energy.* Acta Metallurgica, 1980. 28(12): p. 1789-1797.

135. Bonzel, H.P., *3D equilibrium crystal shapes in the new light of STM and AFM.* Physics Reports-Review Section of Physics Letters, 2003. 385(1-2): p. 1-67.

136. Worren, T., et al., *Copper clusters on Al2O3/NiAl(1 1 0) studied with STM.* Surface Science, 2001. 477(1): p. 8-16.

137. Hansen, K.H., et al., *Palladium Nanocrystals on Al_{2}O_{3}: Structure and Adhesion Energy.* Physical Review Letters, 1999. 83(20): p. 4120.

138. Koplitz, L.V., O. Dulub, and U. Diebold, *STM study of copper growth on ZnO(0001)-Zn and ZnO(0001)-O surfaces.* Journal of Physical Chemistry B, 2003. 107(38): p. 10583-10590.

139. Wuttig, M. and X. Liu, *Growth of Ultrathin Metal Films*, in *Ultrathin Metal Films*. 2004. p. 5-44.

140. Silly, F. and M.R. Castell, *Bimodal growth of Au on SrTiO3(001).* Physical Review Letters, 2006. 96(8).

141. Nilius, N., et al., *Quantization of electronic states in individual oxide-supported silver particles.* Surface Science, 2004. 572(2-3): p. 347-354.

142. Pakarinen, O.H., et al., *High-resolution scanning force microscopy of gold nanoclusters on the KBr (001) surface.* Physical Review B, 2006. 73(23).

143. Tanner, R.E., et al., *The evolution of Ni nanoislands on the rutile TiO2(110) surface with coverage, heating and oxygen treatment.* Surface Science, 2001. 486(3): p. 167-184.

144. Silly, F. and M.R. Castell, *Growth of Ag icosahedral nanocrystals on a SrTiO3(001) support.* Applied Physics Letters, 2005. 87(21).

145. Wolf, D. and S. Yip, eds. *Materials Interfaces: Atomic-level Structure and Properties*. 1992, Springer.

146. Ohtomo, A., et al., *Artificial charge-modulation in atomic-scale perovskite titanate superlattices.* Nature, 2002. 419(6905): p. 378-380.

147. Shaikhutdinov, S.K., et al., *Determination of atomic structure of the metal-oxide interface: Pd nanodeposits on an FeO(111) film.* Physical Review Letters, 2003. 91(7).

148. Herzing, A.A., et al., *Identification of active gold nanoclusters on iron oxide supports for CO oxidation.* Science, 2008. 321(5894): p. 1331-1335.

149. Zhang, Z.L., et al., *Direct atom-resolved imaging of oxides and their grain boundaries.* Science, 2003. 302(5646): p. 846-849.

150. Shibata, N., et al., *Observation of rare-earth segregation in silicon nitride ceramics at subnanometre dimensions.* Nature, 2004. 428(6984): p. 730-733.

151. Jia, C.L. and K. Urban, *Atomic-resolution measurement of oxygen concentration in oxide materials.* Science, 2004. 303(5666): p. 2001-2004.

152. Muller, D.A., et al., *Atomic-scale chemical imaging of composition and bonding by aberration-corrected microscopy.* Science, 2008. 319(5866): p. 1073-1076.

153. LeBeau, J.M., et al., *Quantitative atomic resolution scanning transmission electron microscopy.* Physical Review Letters, 2008. 100(20).

154. Lai, X., et al., *Scanning tunneling microscopy studies of metal clusters supported on TiO2 (110): Morphology and electronic structure.* Progress in Surface Science, 1998. 59(1-4): p. 25-52.

155. Ishizuka, K., *A practical approach for STEM image simulation based on the FFT multislice method.* Ultramicroscopy, 2002. 90(2-3): p. 71-83.

156. Shah, A.B., et al., *The Atomic and Electronic Structure of an Asymmetric LaMnO3-SrMnO3 Superlattice.* Advanced Materials, 2009. 21.

157. Muller, D.A. and J. Silcox, *Delocalization in inelastic scattering.* Ultramicroscopy, 1995. 59(1-4): p. 195-213.

158. Jones, P.G., et al., *Gold(Iii) Oxide.* Acta Crystallographica Section B-Structural Science, 1979. 35(JUN): p. 1435-1437.

159. Kresse, G. and J. Furthmuller, *Efficient iterative schemes for ab initio total-energy calculations using a plane-wave basis set.* Physical Review B, 1996. 54(16): p. 11169-11186.

160. Kresse, G. and J. Hafner, *Ab initio molecular dynamics for liquid metals.* Physical Review B, 1993. 47(1): p. 558.

161. Kresse, G. and D. Joubert, *From ultrasoft pseudopotentials to the projector augmented-wave method.* Physical Review B, 1999. 59(3): p. 1758-1775.

162. Perdew, J.P. and Y. Wang, *Accurate and Simple Analytic Representation of the Electron-Gas Correlation-Energy.* Physical Review B, 1992. 45(23): p. 13244-13249.

163. Winterbottom, W.L., *Equilibrium shape of a small particle in contact with a foreign substrate.* Acta Metallurgica, 1967. 15(2): p. 303-310.

164. Baumgart, T., S.T. Hess, and W.W. Webb, *Imaging coexisting fluid domains in biomembrane models coupling curvature and line tension.* Nature, 2003. 425(6960): p. 821-824.

165. Lipp, M.M., et al., *Phase and morphology changes in lipid monolayers induced by SP-B protein and its amino-terminal peptide.* Science, 1996. 273(5279): p. 1196-1199.

166. Baoukina, S., et al., *The molecular mechanism of lipid monolayer collapse.* Proceedings of the National Academy of Sciences of the United States of America, 2008. 105(31): p. 10803-10808.

167. Schmidt, V., S. Senz, and U. Gosele, *Diameter-dependent growth direction of epitaxial silicon nanowires.* Nano Letters, 2005. 5(5): p. 931-935.

168. Boruvka, L. and A.W. Neumann, *Generalization of Classical-Theory of Capillarity.* Journal of Chemical Physics, 1977. 66(12): p. 5464-5476.

169. Pompe, T. and S. Herminghaus, *Three-phase contact line energetics from nanoscale liquid surface topographies.* Physical Review Letters, 2000. 85(9): p. 1930-1933.

170. Amirfazli, A., et al., *Line Tension Measurements through Drop Size Dependence of Contact Angle.* Journal of Colloid and Interface Science, 1998. 205(1): p. 1-11.

171. Amirfazli, A. and A.W. Neumann, *Status of the three-phase line tension.* Advances in Colloid and Interface Science, 2004. 110(3): p. 121-141.

172. Quere, D., *Surface wetting - Model droplets.* Nature Materials, 2004. 3(2): p. 79-80.

173. Checco, A., P. Guenoun, and J. Daillant, *Nonlinear dependence of the contact angle of nanodroplets on contact line curvature.* Physical Review Letters, 2003. 91(18).

174. Renaud, G., et al., *Real-time monitoring of growing nanoparticles.* Science, 2003. 300(5624): p. 1416-1419.

175. Wen, J.G., et al., *The Formation and Utility of Sub-Angstrom to Nanometer-Sized Electron Probes in the Aberration-Corrected Transmission Electron Microscope at the University of Illinois.* Microscopy and Microanalysis, 2010. 16(2): p. 183-193.

176. Muller, P. and R. Kern, *Equilibrium nano-shape changes induced by epitaxial stress (generalised Wulf-Kaishew theorem).* Surface Science, 2000. 457(1-2): p. 229-253.

177. Gottstein, G., L.S. Shvindlerman, and B. Zhao, *Thermodynamics and kinetics of grain boundary triple junctions in metals: Recent developments.* Scripta Materialia, 2010. 62(12): p. 914-917.

178. Graoui, H., S. Giorgio, and C.R. Henry, *Effect of the interface structure on the high-temperature morphology of supported metal clusters.* Philosophical Magazine B-Physics of Condensed Matter Statistical Mechanics Electronic Optical and Magnetic Properties, 2001. 81(11): p. 1649-1658.

179. Campbell, C.T., S.C. Parker, and D.E. Starr, *The effect of size-dependent nanoparticle energetics on catalyst sintering.* Science, 2002. 298(5594): p. 811-814.

180. Shchukin, V.A. and D. Bimberg, *Spontaneous ordering of nanostructures on crystal surfaces.* Reviews of Modern Physics, 1999. 71(4): p. 1125-1171.

181. Tersoff, J. and F.K. Legoues, *Competing Relaxation Mechanisms in Strained Layers.* Physical Review Letters, 1994. 72(22): p. 3570-3573.

182. Chen, Y. and J. Washburn, *Structural transition in large-lattice-mismatch heteroepitaxy.* Physical Review Letters, 1996. 77(19): p. 4046-4049.

183. Medeiros-Ribeiro, G., et al., *Shape transition of germanium nanocrystals on a silicon (001) surface from pyramids to domes.* Science, 1998. 279(5349): p. 353-355.

184. Dahmen, U., et al., *Magic-size equilibrium shapes of nanoscale Pb inclusions in Al.* Physical Review Letters, 1997. 78(3): p. 471-474.

185. Muller, P. and R. Kern, *Equilibrium shape of epitaxially strained crystals (Volmer-Weber case).* Journal of Crystal Growth, 1998. 193(1-2): p. 257-270.

186. Shuttleworth, R., *The surface tension of solids.* Proceedings of the Physical Society. Section A, 1950. 63: p. 444-457.

187. Ibach, H., *The role of surface stress in reconstruction, epitaxial growth and stabilization of mesoscopic structures (vol 29, pg 193, 1997).* Surface Science Reports, 1999. 35(1-2): p. 71-73.

188. Kollar, J., et al., *Calculation of surface stress for fcc transition metals.* Physical Review B, 2003. 68(24).

189. Koga, K., T. Ikeshoji, and K. Sugawara, *Size- and temperature-dependent structural transitions in gold nanoparticles.* Physical Review Letters, 2004. 92(11).

190. Fu, Q. and T. Wagner, *Interaction of nanostructured metal overlayers with oxide surfaces.* Surface Science Reports, 2007. 62(11): p. 431-498.

191. Stengel, M. and N.A. Spaldin, *Origin of the dielectric dead layer in nanoscale capacitors.* Nature, 2006. 443(7112): p. 679-682.

192. Zhang, P.P., et al., *Electronic transport in nanometre-scale silicon-on-insulator membranes.* Nature, 2006. 439(7077): p. 703-706.

APPENDIX A: IMAGE SIMULATIONS

Image simulations are an integral part of electron microscopy. Particularly, quantitative image contrast interpretation requires the use of image simulations. We have used multislice simulations as implemented in the "ZMULT" program (http://cbed.mse.uiuc.edu) for simulating HRTEM and HRSTEM images. A typical input file (".ms" file) for STEM simulation using "ZMULT" is shown below –

 # enter title and control flags
AU/TiO2 Nanoparticle Simulation File: _sf _auto _xyz _file _cor _new

 # atomic coordinate file
au_tio2.dat

 # HV tiltx tilty
200 0.0 0.0

 # meshx meshy
1024 1024

 # number of slices
40

 # extinction rule 1 1 default
1 1

 # 1 to calculate potential in real space
1

 # Specify the atom and the Debye-Waller factor
3
Ti
0.5
O
0.5
Au
0.574

 # Objective aperture
7.0

 # Output
40 -1

 # pendulusung output
au.pl
1 0 0

 # STEM control
STEM-ADF

 # Probe parameters
df_nm -1.582
c3_mm 0.5658E-02
c5_mm -0.8450
kmax 0.89715
a1_nm 1.34 5.44
a2_nm 22.96 2.31
a3_um 2.76 -16.70
a4_um 3.65 -84.00
a5_mm 2.02 -12.70
b2_nm 15.90 60.42
b4_um 48.84 -35.00
d4_um 19.88 82.20
s3_um 1.19 150.90
fhi 90

#starting probe position
probe 0.5137 0.3105

#end of probe parameter input
end

#scan area (in units of image size, i.e. 1 pixel ≡ 1/1024 = 0.0098) followed by
 # number of sampling points in x and y directions (in units of pixels)
0.00098 0.5664 1 290

#inner and outer detector radius in sin(theta)/lamda and maximum atomic radius in Angstrom
1 2 10

The atomic coordinates of the specimen were provided in the form of a ".dat" file as the input for the above program. The ".dat" file is generated using the "MXTAL" program (http://cbed.mse.uiuc.edu). The commands used to generate a typical Au-TiO_2 ".dat" file in "MXTAL" are given below –

mxtal> load tio2rutile.dat

mxtal> transform 0 0 1 1 -1 0 1 1 0 0 0 0

mxtal> box -13 -6 -7 13 0 7

mxtal> place 1 0 0 0 0 1 0 0 0

At this stage, the output should appear as shown below (Figure A1) where the TiO_2 model is being viewed along [-110] direction. Blue atoms represent oxygen and pink atoms represent titanium.

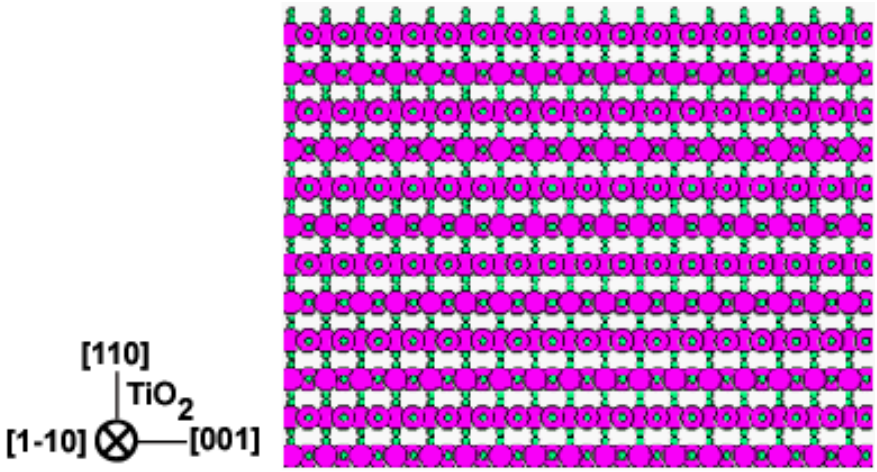

Figure A1: Model of TiO_2 slab generated using MXTAL

The oxygen atoms at the surface can be modified/removed using the select command in "MXTAL". The Au nanocrystal is added to the model using the following commands in "MXTAL".

mxtal> load au.xtl

mxtal> sphere 35 -1

mxtal> hcut 1 1 1 22.0

mxtal> hcut 1 0 0 23

mxtal> acut -1 -1 -1 9.75

mxtal> place -1 1 0 1 1 -2 0 0 0

mxtal> shift 2 0 11 0

mxtal> view 3 110 0.8

At this stage the output should appear as shown below (Figure A2) where the interfacial distance between Au and TiO_2 has been fixed arbitrarily by the "shift" command. Blue atoms represent oxygen, pink atoms represent titanium and green atoms represent gold.

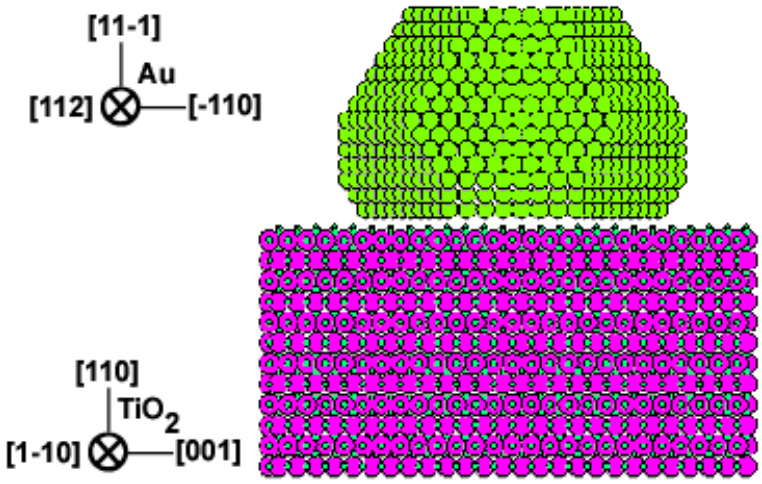

Figure A2: Model of Au nanocrystal supported on TiO_2 (110) generated using MXTAL

In order to output the atomic coordinates to a ".dat" file that is recognized by "ZMULT" the following commands are used

mxtal> open au_tio2.dat

mxtal> print_a 4

Often times, it is necessary to alter the original atomic coordinates created in "MXTAL" – for example to create a wedge shaped specimen, surface reconstructions etc. This was achieved by altering the coordinate file (".xyz") produced by "MXTAL" in the Accelrys Discovery Studio program.

APPENDIX B: E-BEAM EVAPORATION PROCEDURES

Prior to using the e-beam evaporator, the material of choice has to be loaded in the e-beam evaporator by venting the chamber. The choice of crucible liners is vital for each material. An extensive list of crucible liners is available at "http://www.plasmaterials.com/ThinFilmEvapMatSrcRef.pdf". The crucibles can be replaced quickly through the glass-viewport flange located on the filament-side of the evaporator using type-7 tweezers. There is no need to remove the entire e-beam evaporator for crucible replacement. Once the required materials have been loaded into the e-beam evaporator, the chamber has to be pumped down and baked to less than 100^{o}C for 24 hours. Since the e-beam evaporator has O-ring seals for isolating the flowing water from the vacuum, baking to greater than 120^{o}C will result in the fracture of O-rings and leak of water into the vacuum chamber. After the bake, the chamber base pressure should be below $2x10^{-8}$ torr. Upon obtaining this pressure, the e-beam evaporator can be degassed and kept ready for later operation (degassing instructions below). The following instructions are for routine e-beam evaporation of materials.

1. Rotate the crucibles and bring the required target into position.

    a. Always perform only anticlockwise motion of the rotary handle. This increases the life of the O-Rings.

    b. Always go slow when doing the rotation. Fast rotation can damage the O-Rings.

2. Check if HV supply is connected to the copper leads.

3. Turn on water. Wait for at least 15 minutes before starting the e-beam evaporator.

Water Supply Instructions:

a. Open the red valve, so that water can flow through the e-beam evaporator and the thickness monitor

b. The water pressure is sufficient only if the bubbles are pushed out through the outlet pipe. If the bubbles are stuck in the pipes, increase the water pressure slowly till they are pushed out and water flows freely.

4. Switch on the MAIN toggle switch. (Black color toggle switch at Right bottom corner). Wait till the High voltage and current reading stabilize to a value around zero. The "OFF/RESET" button will automatically come on.
5. Press the "HIGH VOLTAGE ON" (white) button. It should light up. Wait for the high voltage reading to reach 5.5 kV.
6. Press the "FIL ON/OFF" (white) button. It should light up.
7. *Deposition instructions (only if the e-beam has been degassed already):*
    a. Make sure that the shutter is closed. Very slowly (at the rate of <1 milliampere per minute) turn up the "EMISSION CURRENT ADJUST" rotary knob while watching the pressure. The pressure should not rise above $5x10^{-7}$ torr at any point of time.
    b. Set up the thickness monitor in the meantime.
    c. Upon reaching desired value of emission current, open the physical shutter and the thickness monitor's shutter at the same time.
    d. After depositing the required amount of material, close the physical shutter.
    e. Slowly turn down the "EMISSION CURRENT ADJUST" to zero.
    f. Switch off the "FIL ON/OFF". The light should go off.

g. Press “OFF/RESET”. The “HIGH VOLTAGE ON” (white) button light should go off. Wait for the high voltage reading to reach 0 kiloVolts. The “OFF/RESET” light will continue to be on. This is normal.

Degassing Instructions (to be followed if e-beam is being operated for the first time after venting the chamber) :

a. Make sure that the e-beam shutter is open.
b. Go up to 1 milliAmpere. The pressure will jump to ~4 x 10^{-7} torr. Wait till the pressure comes down to ~ 2 x 10^{-7} torr.
c. Now slowly increase the emission current by 1 milliampere. The pressure will jump each time. Wait for the pressure to drop to ~2x10^{-7} before increasing the emission current again.
d. Keep increasing the emission current slowly until the thickness monitor records around 5 A of deposited material. The e-beam source is then sufficiently.
e. Now Slowly turn down the “EMISSION CURRENT ADJUST” to zero.
f. Switch off the “FIL ON/OFF”. The light should go off.
g. Press “OFF/RESET”. The “HIGH VOLTAGE ON” (white) button light should go off. Wait for the high voltage reading to reach 0 kiloVolts. The “OFF/RESET” light will continue to be on. This is normal.
h. Rotate the crucibles and go to the next source.

    a. Always perform only anticlockwise motion of the rotary handle. This increases the life of the O-Rings.

    b. Always go slow when doing the rotation. Fast rotation can damage the O-Rings.

i. Repeat the degassing procedure for the next crucible and thus successively degas all four sources.

8. SHUTDOWN Instructions:

    a. Switch off the MAIN toggle switch.

    b. Close the physical shutter.

    c. Swithch off the thickenss monitor.

    d. Let the water run for 30 minutes after turning off the e-beam evaporator

    e. Close the red valve, so that water does not flow through the ebeam evaporator and the thickness monitor any more.

    f. Reduce the water flow rate (green knob) so that it is enough for the Turbo pump.

APPENDIX C: RHEED DATA ANALYSIS

The evolution of epitaxy with temperature can be tracked by tracking the intensity of individual spots in the RHEED patterns. In our system, we used the following procedure to track individual RHEED spots.

1. Filename of images were designated to be the μV reading of thermocouple, i.e. a reading of 0.811mV on the voltmeter would translate to a filename "0811.tif".
2. Background images were acquired every 1000 μV by blanking the beam.
3. The images were processed using "Gatan Digital Micrograph" using the following script which computes the integrated intensity of a chosen spot on the topmost image by compensating for spot motion from electric field of the heater. The script calculates temperature by a 10^{th} order polynomial fit to the thermocouple reading versus temperature curve. Care must be exercised in choosing a spot that is not close to any damaged pixels (damaged pixels refer to various spots on the RHEED screen that light up upon heating beyond 500^{o}C). Once a spot is identified, the following input parameters in should be entered in the script before running the script to process all the images. The inputs to the script are described below –
    i. Input 1: x and y coordinates of the maximum intensity in the spot from RHEED patterns taken after the heater is turned off and the sample has cooled down and the difference in the x and y positions of the spot's maximum between the highest temperature RHEED pattern and the RHEED pattern obtained after sample has cooled down.

ii. Input 2: Width and height (in pixels) of box to be used for obtaining integrated intensity. Typical values for the width and height of box used for integrated intensity are 20 pixels each.

iii. Input 3: The lowest and highest temperatures measured in the experiment. The temperature should be obtained by the same 10^{th} order polynomial fit used in the script.

iv. Input 4: The x, y coordinates of the top left corner and width and height of box used for obtaining background. The background must be obtained close to the spot for accurate background subtraction. Also, the background should have any damaged pixels. Typical values for the background height and width are 36 pixels each.

The script is given in full below.

```
image front := findfrontimage()

////////////////////////////////// INPUTS Section ////////////////////////////////////////

// INPUT 1: max_X, max_y, x_drift, y_drift

        number max_x = 192;  number max_y = 153; // To be obtained from last cooling down image

        number x_drift = 5; number y_drift = 6;

         // Difference in positions of maxima ( Maximum_x_Highest_Temp - Maximum_x_Cooling_Down)

// INPUT 2: width_spot, height_spot

        number width_spot = 20;   number height_spot = 20;
```

```
// INPUT 3: start_temp, end_temp

        number start_temp = 214.625; // Lowest temperature measured

        number end_temp = 767.087; // Highest temperature measured

// INPUT 4: start_x_bg, start_y_bg, width_bg, height_bg

        number start_x_bg = 278;  number start_y_bg = 344;

        number width_bg = 36; number height_bg = 36;

//////////////////////////// Processing Section ////////////////////////////////////////

number end_x_bg = start_x_bg + width_bg;

number end_y_bg = start_y_bg + height_bg;

number integrated_intensity_bg = sum (front [start_y_bg, start_x_bg, end_y_bg, end_x_bg]);

number integrated_intensity_bg_norm = integrated_intensity_bg*(width_spot*height_spot)/(width_bg*height_bg);

number Tc = val(Getname(front))/1000;

number T = (-0.00000196844*(Tc**10)) + 0.000142706*(Tc**9) - 0.0043851*(Tc**8) + 0.074395*(Tc**7)-
0.76341*(Tc**6) + 4.9277*(Tc**5) - 20.674*(Tc**4) + 60.628*(Tc**3) - 139.42*(Tc**2) + 284.96*Tc + 50.298;

number start_x = max_x - width_spot/2 + ( x_drift * (T - start_temp) / (end_temp - start_temp) );

number start_y = max_y - height_spot/2 + ( y_drift * (T - start_temp) / (end_temp - start_temp) );

number end_x = start_x + width_spot;

number end_y = start_y + height_spot;

number integrated_intensity_spot = sum (front [start_y, start_x, end_y, end_x]);
```

```
number integrated_intensity_spot_bgsub = integrated_intensity_spot - integrated_intensity_bg_norm;

//////////////////////////// Output Section ////////////////////////////////////////////////

result (Getname(front) + " , " + T + " , " + start_x + " , " + start_y + " , " + integrated_intensity_spot_bgsub + " , " +
integrated_intensity_bg_norm + "\n");

 closeimage(front);
```
